Downloaded from orbit.dtu.dk on: Dec 21, 2017

Technical University of Denmark

Optical Processing of High Dimensionality Signals

Da Ros, Francesco; Peucheret, Christophe; Xu, Jing; Galili, Michael

Publication date:
2014

Document Version
Publisher's PDF, also known as Version of record

Link back to DTU Orbit

Citation (APA):
Da Ros, F., Peucheret, C., Xu, J., & Galili, M. (2014). Optical Processing of High Dimensionality Signals. Kgs. Lyngby: Technical University of Denmark (DTU).

DTU Library
Technical Information Center of Denmark

General rights
Copyright and moral rights for the publications made accessible in the public portal are retained by the authors and/or other copyright owners and it is a condition of accessing publications that users recognise and abide by the legal requirements associated with these rights.

- Users may download and print one copy of any publication from the public portal for the purpose of private study or research.
- You may not further distribute the material or use it for any profit-making activity or commercial gain
- You may freely distribute the URL identifying the publication in the public portal

If you believe that this document breaches copyright please contact us providing details, and we will remove access to the work immediately and investigate your claim.

Optical Processing of High Dimensionality Signals

Ph.D. Thesis
Francesco Da Ros

September 14th, 2014

DTU Fotonik
Department of Photonics Engineering

DTU Fotonik
Department of Photonics Engineering
Technical University of Denmark
Ørsteds Plads 343
DK-2800 Kgs. Lyngby
Denmark

Preface

The work presented in this Thesis was carried out as a part of my Ph.D. project in the period September 15th, 2011 to September 14th, 2014. The work took place at DTU Fotonik (Technical University of Denmark, Department of Photonics Engineering) and at the Fraunhofer Institute for Telecommunications, Heinrich Hertz Institute, Berlin, Germany.

The Ph.D. project was financed by the Technical University of Denmark, the Danish Research Council for Technology and Production Sciences and the FTP7 project EURO-FOS and supervised by:

- Christophe Peucheret (main supervisor 11/2011-08/2013, co-supervisor 09/2013-09/2014), Professor, FOTON Laboratory (CNRS UMR 6082) - ENSSAT - University of Rennes 1, Lannion, France
- Jing Xu (co-supervisor 11/2011-09/2014), Associate Professor, School of Optical and Electronic Information, Huazhong University of Science and Technology, Wuhan, China
- Michael Galili (main supervisor 09/2013-09/2014), Associate Professor, DTU Fotonik, Technical University of Denmark, Kgs. Lyngby, Denmark

Abstract

Optical parametric amplifiers (OPAs) combine high-gain broadband amplification at nearly arbitrary wavelengths with the prospect for achieving an ideally 0-dB noise figure when used in phase-sensitive configuration. Furthermore, several recent demonstrations confirm their potential for all-optical signal processing, including wavelength conversion, optical phase conjugation (OPC), and signal regeneration.
This project focuses precisely on the applications of OPAs for all-optical signal processing with a two-fold focus: on the one hand, processing the advanced modulation formats required to increase the capacity of future communication systems; on the other hand, the different nonlinear material suitable for providing parametric amplification. Therefore, three different materials, namely silica highly nonlinear fibers (HNLFs), silicon waveguides, and periodically poled lithium niobate (PPLN) waveguides, are investigated. The limits of parametric amplification for 16-quadrature amplitude modulation (QAM) signals are first characterized. The acquired knowledge is then applied to the design of a black-box OPC-device used to provide Kerr nonlinearity compensation for a 5-channel polarization-division multiplexing (PDM) 16-QAM signal at 1.12 Tbps with significant improvements in received signal quality.
Furthermore, the first demonstration of phase regeneration for binary phase-shift keying (BPSK) signals using the silicon platform is presented. The silicon-based OPA relies on a novel design where a reverse-biased p-i-n junction fabricated along the waveguide allows decreasing the nonlinear absorption, thus achieving phase-sensitive extinction ratios in excess of 20 dB. Finally, a recently proposed quadrature phase-shift keying (QPSK)-to-2×BPSK wavelength and format converter is characterized experimentally by implementing it using fiber-, silicon, and PPLN-based platforms. Similar results have been measured for all three media under continuous-wave operation and for fiber- and PPLN-based implementations under modulated-

signal operations with little penalty introduced by the conversion.
Altogether this work demonstrates the potential of phase-insensitive and phase-sensitive parametric processing applied to high-dimensionality modulation formats.

Resumé

Optisk parametriske forstærkere (OPA) kombinerer høj bredhånds forstærkningsgrad ved reelt vilkårlige bølgelængder med muligheden for at opnå et ideelt 0 dB støjtal når forstærkeren bliver benyttet i en fase følsom konfiguration. Desuden har nylige eksperimenter understøttet forstærkernes potentiale til optisk signal behandling såsom bølgelængde konvertering, optisk fase spejling (OPC) samt regenerering af signaler.

Fokus for dette projekt er netop applikationer af OPA'er til optisk signal behandling og det har to mål. Det ene mål er at signal behandle de avancerede modulationsformater som er nødvendige for at kunne øge kapaciteten i fremtidens kommunikationssystemer. Det andet mål er at undersøge forskellige ikke-lineære materialers brugbarhed som parametriske forstærkere. Derfor er tre forskellige materialer blevet undersøgt - stærkt ikke-lineære silicium baserede fibre (HNLF), silicium bølgeledere samt periodisk inverteret (poled) litium niobate bølgeledere (PPLN). Begrænsningerne af parametriske forstærkere i et 16-kvadratur amplitude moduleret signal (QAM) er først blevet afdækket. Den tilegnede viden er derpå blevet anvendt til at designe en såkaldt sort-boks OPC enhed som ved hjælp af Kerr ikke-lineær kompensation giver betragtelig forbedring af et modtaget 5-kanals polarisations flettet (PDM) 16-QAM 1.12 Tbps signal.

Endvidere er den første demonstration af fase regenerering af et binært fase-skiftet signal (BPSK) i en silicium platform bliver præsenteret. Den silicium-baserede OPA udnytter et nyt design hvor en omvendt bias p-i-n forbindelse som er fabrikeret langs en bølgeleder tillader en reduktion af den ikke-lineære absorption hvorved et fase-følsomt slukningsforhold på mere end 20 dB er opnået. Afslutningsvis, er et nyligt foreslået kvadratur fase-skiftet (QPSK) til 2×BPSK bølgelængde og format konverterings princip blevet karakteriseret i henholdsvis fiber, silicium samt PPLN platforme. Sammenlignelige resultater er blevet målt for alle tre materialer når kontinuert lys er blevet benyttet. Både den fiber samt den PPLN baserede

implementering er desuden blevet karakteriseret med modulerede signaler og kun små forværringer er blevet introduceret ved konverteringen.

Sammenholdes dette arbejde er potentialet for fase-ikke-følsom og fase-følsom parametrisk behandling af mange-dimensionale modulations formater blevet demonstreret.

Acknowledgements

The results presented in this thesis would not have been achieved if not for the direct or indirect contribution of many people to whom I am extremely grateful and I will start by apologizing if I may have forgotten some of you.

First and foremost I would like to thank my supervisors Prof. Christophe Peucheret, Assoc. Prof. Jing Xu and Assoc. Prof. Michael Galili for their invaluable guidance throughout these years. Their constant support and extreme patience as well as friendliness have made this period a pleasant and enjoyable learning opportunity.

In particular, I would like to thank Christophe Peucheret for his brilliant mentoring even before the start of the Ph.D. project and for making the project possible. I will always be grateful for introducing me to experimental work and teaching me the rigorous research approach without which the work presented in this thesis could not have been completed. Jing Xu and Michael Galili are deeply acknowledged for their constructive suggestions and interesting technical discussions.

I am grateful to my examiners Prof. Periklis Petropoulos (Optoelectronics Research Centre, University of Southampton, UK), Prof. Michael Vasilyev (University of Texas at Arlington, USA) and Assoc Prof. Jesper Lægsgaard (DTU Fotonik) for taking the time to read this thesis and for their constructive feedback that definitely helped improving its quality.

I would like to thank all former and present colleagues and friends in the High-Speed Optical Communication Group at DTU Fotonik for the great working environment that made the whole period much more fun. Thank you Dragana, Evarist, Hans Christian, Hao, Ji Hua, Jorge, Lei Lei, Ning, Robert, Yi, Yunhong, Yutaka, and Zohreh for making the long weekends in the lab much more enjoyable. Thank you also to Ashu, Asger,

Deming, Feihong, Rameez, and Valerija for the much needed coffee breaks and for being great office mates. I am grateful to Anders and Leif for the interesting discussion and their moral and technical support. Their help with the practical bureaucratic matters and translations in Danish has also been highly appreciated. Then, a big thank to Kjeld whose skills have made phase-sensitive amplification possible.

I would like to thank the Technical University of Denmark, the Danish Research Council for Technology and Production Sciences and the FTP7 project EURO-FOS for supporting this Ph.D. project. I am grateful to Otto Mønsted, Oticon and Torben og Alice Frimodts foundations for their financial support which allowed me to attend several international conferences as well as my external research stay at the Heinrich-Hertz Institute, Berlin, Germany.

A special thank goes to Colja Schubert for welcoming me at the HHI and for making my seven-month external research stay extremely smooth, interesting and enjoyable. *Vielen Dank* also to all the members of the Submarine and Core System (SCS) and DPS groups at the HHI for accepting me into their group and for never being too busy to provide brilliant suggestions, regardless of their tight schedule. I am really grateful to Isaac, Thomas, Christian, Markus, Robert, Carsten, Lutz, Saleem, Pablo, Felix, and Johannes. Your kindness, enthusiasm and hard-work are inspiring and I will never forget the stimulating discussions in front of the coffee machine and the Friday bars at Zeitlos.

Thanks to Prof. Klaus Petermann at the Technical University of Berlin (TUB) and Lars Zimmermann at IHP for a fruitful and valuable collaboration, and especially to Andrzej and Mahmoud at TUB; it has been a pleasure working with you.

To all my friends in Denmark, Albert, Alessio, Carolina, Giorgos, Ioan, Kamau, Javier, Matias, Matteo, Silvia, Stig, Valentina, thanks for all the time you dragged me out of the lab when I really needed a break.

Last but definitely not least, many thanks to my parents and my sister for their continuous support unaffected by the distance and to Valentina for bearing with me every day with great patience.

Ph.D. Publications

The following publications have resulted from this Ph.D. project.

Articles in international peer-reviewed journals: (11)

J1 D. Vukovic, J. Schröder, **F. Da Ros**, L. Bangyuan Du, C.J. Chae, D-Y Choi, M.D. Pelusi, and C. Peucheret, "Multichannel nonlinear distortion compensation using optical phase conjugation in a silicon nanowire," *Optics Express*, **23**, 3640–3646 (2015).

J2 H.C. Hansen Mulvad, **F. Da Ros**, M. Galili, K. Dalgaard, and L.K. Oxenløwe, "Phase regeneration of a DPSK data signal using a Lithium Niobate phase modulator", *Journal of Lightwave Technology*, **33**, 2189–2198 (2015).

J3 I. Sackey, **F. Da Ros**, J.K. Fischer, T. Richter, M. Jazayerifar, C. Schubert, K. Petermann, and C. Peucheret, "Kerr nonlinearity mitigation: mid-link spectral inversion versus digital backpropagation in 5×28-GBd PDM 16-QAM signal transmission," *Journal of Lightwave Technology*, **33**, 1821–1827 (2015).

J4 I. Sackey, **F. Da Ros**, M. Jazayerifar, T. Richter, C. Meuer, M. Nölle, L. Molle, C. Peucheret, K. Petermann, and C. Schubert, "Kerr nonlinearity mitigation in 5×28-GBd PDM 16-QAM signal transmission over a dispersion-uncompensated link with backward-pumped distributed Raman amplification," *Optics Express*, **22**, 27381–27391 (2014).

J5 **F. Da Ros**, K. Dalgaard, Y. Fukuchi, J. Xu, M. Galili, and C. Peucheret, "Simultaneous QPSK-to-2×BPSK wavelength and modulation format conversion in PPLN," *IEEE Photonics Technology Letters*, **26**, 1207–1210 (2014).

J6 **F. Da Ros**, D. Vukovic, A. Gajda, K. Dalgaard, L. Zimmermann, B. Tillack, M. Galili, K. Petermann, and C. Peucheret, "Phase regeneration of DPSK signals in a silicon waveguide with reverse-biased p-i-n junction," *Optics Express*, **22**, 5029–5036 (2014).

J7 **F. Da Ros**, K. Dalgaard, L. Lei, J. Xu, and C. Peucheret , "QPSK-to-2×BPSK wavelength and modulation format conversion through phase-sensitive four-wave mixing in a highly nonlinear optical fiber," *Optics Express*, **21**, 28743–28750 (2013).

J8 L. Lei, **F. Da Ros**, J. Xu, C. Peucheret, J. Dong, and X. Zhang, "All-optical three-input logic minterms generation using semiconductor optical amplifier-based Sagnac interferometer," *Electronics Letters*, **13**, 1467–1468 (2013).

J9 Y. Ding, J. Xu, **F. Da Ros**, B. Huang, H. Ou, and C. Peucheret, "On-chip two-mode division multiplexing using tapered directional coupler-based mode multiplexer and demultiplexer," *Optics Express*, **21**, 10376–10382 (2013).

J10 Y. Ding, B. Huang, H. Ou, **F. Da Ros**, and C. Peucheret, "Polarization diversity DPSK demodulator on the silicon-on-insulator platform with simple fabrication," *Optics Express*, **21**, 7828–7834, (2013).

Contributions to international peer-reviewed conferences: (22)

C1 K. Petermann, A. Gajda, G. Dziallas, M. Jazayerifar, L. Zimmermann, B. Tillack, **F. Da Ros**, D. Vukovic, K. Dalgaard, M. Galili, and C. Peucheret, "Phase-sensitive gain in silicon waveguides," *Optical Fiber Communication Conference, OFC* (2015), paper Tu2F.4 [invited].

C2 **F. Da Ros**, M. Nölle, C. Meuer, A. Rahim, K. Voigt, A. Abboud, I. Sackey, S. Schwarz, L. Molle, G. Winzer, L. Zimmermann, C.G. Schäffer, J. Bruns, K. Petermann, and C. Schubert, "Experimental demonstration of an OFDM receiver based on a silicon-nanophotonic discrete Fourier transform filter," in *IEEE Photonics Conference, IPC* (2014), paper MG2.5.

C3 I. Sackey, **F. Da Ros**, T. Richter, R. Elschner, M. Jazayerifar, C. Meuer, C. Peucheret, K. Petermann, and C. Schubert, "Design and performance evaluation of an OPC device using a dual-pump

polarization-independent FOPA," in *European Conference on Optical Communication, ECOC* (2014), paper Tu.1.4.4.

C4 **F. Da Ros**, I. Sackey, R. Elschner, T. Richter, C. Meuer, M. Nölle, M. Jazayerifar, K. Petermann, C. Peucheret, and C. Schubert, "Kerr nonlinearity compensation in a 5×28-GBd PDM 16-QAM WDM system using fiber-based optical phase conjugation," in *European Conference on Optical Communication, ECOC* (2014), paper P.5.3.

C5 L.K. Oxenløwe, M. Pu, Y. Ding, H. Hu, **F. Da Ros**, D. Vukovic, A. Sellerup Jensen, H. Ji, M. Galili, C. Peucheret, K. Yvind "All-Optical signal processing using silicon devices," in *European Conference on Optical Communication, ECOC* (2014), paper We.2.5.1 [invited].

C6 C. Peucheret, **F. Da Ros**, D. Vukovic, Y. Ding, K. Dalgaard, M. Galili, A. Gajda, J. Xu, Y. Fukuchi, H. Hu, L. Lei, H. Ou, L. Zimmermann, L.K. Oxenløwe, B. Tillack, and K. Petermann, "Parametric phase-sensitive and phase-insensitive all-optical signal processing on multiple nonlinear platforms," in *Progress In Electromagnetics Research Symposium, PIERS*, 1160 (2014) [invited].

C7 C. Peucheret, **F. Da Ros**, D. Vukovic, K. Dalgaard, M. Galili, A. Gajda, L. Zimmermann, B. Tillack, and K. Petermann, "Parametric optical signal processing in silicon waveguides with reverse-biased p-i-n Junctions," in *IEEE Summer Topical* (2014), paper TuD4.1 [invited].

C8 J. Martìnez Dìaz, J. Bohigas Nadal, D. Vukovic, **F. Da Ros**, E. Palushani, and C. Peucheret, "A comparison of nonlinear media for parametric all-optical signal processing," in *IEEE Photonics Conference, IPC* (2013), paper ThG1.5.

C9 **F. Da Ros**, D. Vukovic, A. Gajda, L. Zimmermann, K. Petermann, and C. Peucheret, "Continuous wave phase-sensitive four-wave mixing in silicon waveguides with reverse-biased p-i-n junctions," in *European Conference on Optical Communication, ECOC* (2013), paper P.2.11.

C10 A. Gajda, **F. Da Ros**, D. Vukovic, L. Zimmermann, C. Peucheret, B. Tillack, and K. Petermann, "High efficiency wavelength conversion of 40 Gbps signals at 1550 nm in SOI nano-rib waveguides using p-i-n diodes," in *IEEE International Conference on Group IV Photonics* (2013), paper FC3.

C11 **F. Da Ros**, J. Xu, L. Lei, and C. Peucheret, "Phase noise tolerant QPSK receiver using phase sensitive wavelength conversion," in *OptoElectronics and Communications Conference/Photonics in Switching, OECC/PS* (2013), paper TuS2-5.

C12 V. Cristofori, Z. Lali-Dastjerdi, **F. Da Ros**, L.S. Rishøj, M. Galili, C. Peucheret, and K. Rottwitt, "Fiber optical parametric chirped pulse amplification of sub-picosecond pulses," in *OptoElectronics and Communications Conference/Photonics in Switching, OECC/PS* (2013), paper TuS2-3.

C13 E. Palushani, H.C. Hansen Mulvad, M. Galili, **F. Da Ros**, H. Hu, P. Jeppesen, and L.K. Oxenløwe, "Spectral Compression of a DWDM grid using optical time-lenses," in *OptoElectronics and Communications Conference/Photonics in Switching, OECC/PS* (2013), paper ThO2-1.

C14 Y. An, M. Müller, J. Estaran, S. Spiga, **F. Da Ros**, C. Peucheret, and M.-C. Amann, "Signal quality enhancement of directly-modulated VCSELs using a micro-ring resonator transfer function," in *OptoElectronics and Communications Conference/Photonics in Switching, OECC/PS* (2013), paper ThK3-3.

C15 **F. Da Ros**, M.P. Calabrese, N. Kang, E. Palushani, and C. Peucheret, "Orthogonal phase quadratures conversion to different wavelengths through phase-sensitive four wave mixing in an Highly Nonlinear Fiber," in *Optical Fiber Communication Conference, OFC* (2013), paper OW4C.

C16 Y. An, **F. Da Ros** and C. Peucheret, "All-optical network coding for DPSK signals," in *Optical Fiber Communication Conference, OFC* (2013), paper JW2A.60.

C17 Y. Ding, B. Huang, H. Ou, **F. Da Ros**, and C. Peucheret, "Polarization diversity DPSK demodulator on the silicon-on-insulator platform with simple fabrication," in *Optical Fiber Communication Conference, OFC* (2013), paper OTh4I.4.

C18 **F. Da Ros**, R. Borkowski, D. Zibar, and C. Peucheret, "Impact of gain saturation on the parametric amplification of 16-QAM signals," in *European Conference on Optical Communication, ECOC* (2012), paper We.2.A.3.

C19 Z. Lali-Dastjerdi, O. Ozolins, Y. An, V. Cristofori, **F. Da Ros**, N. Kang, H. Hu, H.C. Hansen Mulvad, K. Rottwitt, M. Galili, and

C. Peucheret, "Demonstration of cascaded in-line single-pump fiber optical parametric amplifiers in recirculating loop transmission," in *European Conference on Optical Communication, ECOC* (2012), paper Mo.2.C.5.

C20 **F. Da Ros**, K. Rottwitt, and C. Peucheret, "Gain optimization in fiber optical parametric amplifiers by combining standard and high-SBS threshold highly nonlinear fibers," in *Conference on Lasers and Electro-Optics, CLEO* (2012), paper CM4N.5.

C21 Z. Lali-Dastjerdi, **F. Da Ros**, K. Rottwitt, M. Galili, and C. Peucheret, "Pulse distortion in saturated fiber optical parametric chirped pulse amplification," in *Conference on Lasers and Electro-Optics, CLEO* (2012), paper JW2A.82.

C22 **F. Da Ros**, and C. Peucheret, "QPSK phase regeneration in saturated degenerate dual-pump phase sensitive amplifiers," in *IEEE Photonics Conference, IPC* (2012), paper MM3.

Contents

Chapter 1

Introduction

The 1980s have represented a turning point in the field of telecommunication with the deployment of the first transatlantic fiber optics cable (TAT-8) between Europe and North America in 1988. The transmission bitrate at the time was 280 Mbps, a somehow insignificant number if compared with some of the recently demonstrated bitrates which exceeds the 1-Pbps threshold [1,2], i.e. with a seven orders of magnitude increase in less than 30 years. Such tremendous improvement has been made possible by numerous advances in several key technologies for optical communication systems.

First of all, the development of laser diodes emitting around 1550 nm, combined with the improvements in optical fiber fabrication allowed exploiting the low transmission losses of that wavelengths window (0.2 dB/km).

Following, the developments in the field of all-optical amplification culminated with the introduction of erbium-doped fiber amplifiers (EDFAs) in 1987 [3]. Providing amplification all-optically removed the need for electronic repeaters, thus discarding opto-electronic and electro-optic converters. At the same time, the broad EDFA amplification bandwidth (∼30 nm) enabled a significant boost in transmission speed allowing the introduction of wavelength-division multiplexing (WDM) transmission.

Next, the migration from amplitude-modulated (OOK) to phase-modulated (BPSK and QPSK) signals in the early 2000s combined the advantage of a decreased sensitivity, thanks to balanced detection, and a narrower spectral occupancy [4].

Another leap forward has been made possible by the commercial introduction of coherent receivers around 2006 [5], which opened the doors to the use of more advanced modulation formats where the information is encoded

in both the amplitude and the phase of the optical carrier. Additionally, the full access to the complex optical field enabled by coherent detection allowed applying the advances in digital signal processing (DSP) achieved for radio-frequency systems to the world of optical communications. Digital signal processing provides interesting features such as dispersion compensation, as well as a further doubling of the bitrate enabling the transmission of polarization-division multiplexing (PDM) signals.
Currently, a strong focus has been directed towards looking into a fifth physical dimension (after amplitude, phase, frequency, and polarization) to be exploited for encoding information, namely space. The use of multi-core [1] and multi-mode [2] transmissions have been the key to breach the Petabit threshold.

1.1 Motivation

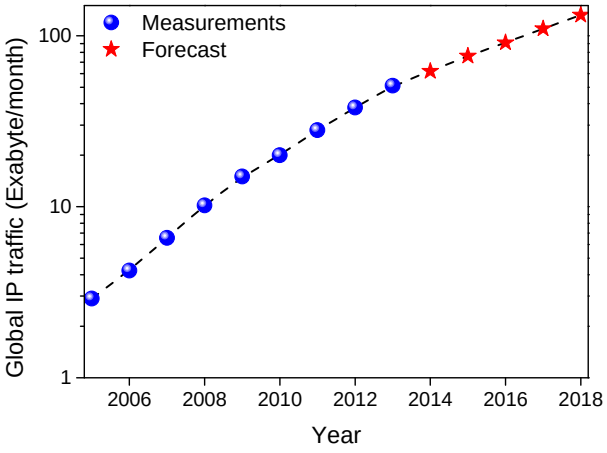

Figure 1.1: Monthly data traffic increase per year: measurements and forecasts from CISCO® VNI [6].

The significant increase in demand for capacity coming from the introduction of more bandwidth-hungry services, such as high-definition video streaming and online gaming, just to name a few that acquired high popularity recently, has been the driving force pushing for higher speed transmissions. As highlighted in Fig. 1.1, the global IP traffic has been steadily increasing in the past years with a forecasted growth rate above 20% for the next five years [6].

In order to cope with such continuously growing demand, techniques to increase the spectral efficiency, i.e. the amount of information that can be encoded in a given spectral bandwidth, have been receiving a strong focus from the research community [4].
Several directions have been pursued to achieve such a goal. The use of more advanced modulation formats such as quadrature amplitude modulation (QAM), allows squeezing more bits of information into one single transmitted symbol. Additionally, the use of spectral and temporal shaping provides a further increase in spectral efficiency. The use of orthogonal signals either in the time domain, as for Nyquist WDM, or in the frequency domain, as for orthogonal frequency-division multiplexing (OFDM), enables decreasing the channels spacing and in turn the spectral bandwidth per channel.

While these techniques boost the transmission speed, they also increase the requirements in terms of received signal quality. The received optical signal-to-noise ratio (OSNR) for error-free transmission unfortunately scales with the size of the signal constellation. As optical amplifiers add noise to the signal with a typical noise figure around $4-6$ dB, the number of times amplification can be provided before the signal becomes incomprehensible at the receiver is decreased with the modulation format complexity, therefore lowering the maximum transmission reach for advanced modulation formats.
A well-known technique to ensure that a higher OSNR is maintained throughout the transmission consists on increasing the launched power at the span input. However, a strong electrical field propagating through a silica fiber excites Kerr nonlinearity in the material which, in turn, distorts the signal, eventually limiting the maximum capacity-distance product achievable.
Signal regeneration, low-noise amplification, and nonlinear distortion compensation are, therefore, desirable functions which are widely investigated nowadays.
Furthermore, a communication network may require several other functionalities including switching, wavelength conversion, and data format conversion among others.

At the present moment, most of the functionalities currently implemented make use of electrical signal processing [7]. That happens not only for historical reasons but also because electrical signal processing offers a number of advantages, spacing from reliable performances and small footprints to a high degrees of integration and low energy consumption.
Information communication technologies accounted alone for around 6% of

the global energy consumption in 2013 [8] with a carbon footprint of around $2 - 2.5\%$ [9]. The potential to decrease the energy consumption is, then, one of the key aspects driving both optical and electrical signal processing.

All-optical signal processing has the potential to be competitive, at least for simple processing functions [7], as it avoids conversion of signals between optical and electrical domain for processing.
Furthermore, while the technological advances in electronics have been able to keep up the pace with the increase in transmission bitrates, all-optical processing is mostly based on ultra-high speed nonlinear effects (order of fs) taking place in optical fibers or other nonlinear waveguides and, therefore, may ultimately be more suitable for high-speed processing. Finally, recent progresses in the fabrication of silicon waveguides [10], as well as other nonlinear materials such as chalcogenide glasses [11] and III-IV semiconductors [12] narrow the gap between optics and electronics also in term of footprint and potential for on-chip integration.

Nevertheless, all-optical signal processing still requires further research before reaching the maturity necessary for practical applications.
Along this direction, the application of all-optical signal processing to advanced modulation formats is the main topic of this thesis.

1.2 Scope and structure of the thesis

Nonlinear optics and in particular parametric amplification are essential tools to provide the all-optical signal processing functionalities discussed in this thesis.

The use of a strong optical pump injected in a nonlinear medium to provide amplification through parametric processes has been investigated as early as in the 1960 [13, 14].
However, it is only in more recent years, with improvements in the fabrication of nonlinear media, as well as the availability of high output power booster EDFAs, that the interest towards parametric amplification has been drastically increased with several impressive breakthroughs being reported in terms of high gain [15, 16], broad bandwidth [17, 18], and low-noise amplification [19].
Moreover, the applications of parametric processes are far from being limited to amplification alone. Parametric amplifiers have been demonstrated to be effective for optical signal processing as they can provide, for

example, broadband wavelength conversion [20], optical sampling [21], and signal regeneration [22, 23].

The goal of this thesis is to further investigate applications of parametric amplification for all-optical signal processing with a two-fold focus. On the one side a strong interest is directed towards advanced modulation formats spacing from binary phase-shift keying (BPSK), quadrature phase-shift keying (QPSK), and up to WDM PDM 16-QAM. On the other side, different nonlinear media are investigated including Kerr nonlinear materials such as standard highly nonlinear fibers (HNLFs) and silicon waveguides, together with a second-order nonlinear material such as periodically poled lithium niobate (PPLN) waveguides. Furthermore, both phase-insensitive (Chapter 3 and Chapter 4) and phase-sensitive (Chapter 5 and Chapter 6) configurations have been considered.

Chapter 2 introduces theoretically the topic of optical parametric amplification, reviewing the fundamental physical effects affecting the propagation of an electromagnetic wave at optical frequencies through a dielectric medium. The interplay between dispersion and Kerr nonlinearity resulting in parametric amplification is highlighted in terms of phase matching requirements, achievable signal gain in phase-insensitive and phase-sensitive operation, and gain saturation characteristics. Numerical simulations support the analytical derivations to provide a better understanding of the topic. Finally, an overview of the state-of-the-art results achieved with phase-insensitive and phase-sensitive amplifiers is provided.

Chapter 3 reports the use of fiber optical parametric amplifiers (FOPAs) to provide amplification of 16-QAM signals. Signal performances are numerically investigated operating the single-pump FOPA both in unsaturated and saturated regimes. A modulation-state dependent analysis highlights the main causes of signal distortion for saturated amplification. Furthermore, a figure of merit (FOM), introduced by Elschner *et al.* [24] to describe the effects of cross-talk for WDM amplification, can be applied to characterize saturation-induced distortion, providing an accurate description. The numerical findings are then confirmed by experimental results for a 14-Gbaud 16-QAM signal.

In Chapter 4, the use of optical phase conjugation (OPC) as an effective technique to provide dispersion and Kerr nonlinearity compensation is

introduced, focusing on the link requirements for the compensation to be effective. The application of a dual-pump polarization insensitive FOPA to provide black-box OPC is then discussed, exploring how to fulfill the key requirements for a practical OPC device and focusing on the optimization process. The performance improvements providing mid-span spectral inversion (MSSI) by using the implemented OPC device are presented for a single- and five-channel 28-Gbaud PDM 16-QAM signal. Two link configurations are considered: a dispersion-compensated link using standard lumped EDFA-based amplification and a dispersion-uncompensated link using distributed Raman amplification with backward pumping.
The results presented in Chapter 4 are the outcomes of a collaboration with I. Sackey (Technische Universität Berlin and Heinrich Hertz Institute). The experiments have been carried out during an external research stay in the Submarine and Core System (SCS) group at the Fraunhofer Institute for Telecommunications, Heinrich Hertz Institute, Berlin, Germany.

Chapter 5 reports the first demonstration of all-optical phase regeneration for differential phase-shift keying (DPSK) signals using a silicon platform. A novel waveguide design with a reverse-biased p-i-n junction fabricated along the waveguide allows decreasing the impact of nonlinear absorption, thus increasing the efficiency of the nonlinear interaction. High-efficiency wavelength conversion leading to low-penalty idler generation is presented. Furthermore, in a continuous wave (CW) static demonstration of phase-sensitive amplification, appreciable phase-sensitive extinction ratio (PER) levels in excess of 20 dB are obtained for the first time, enabling all-optical phase regeneration for a 10-Gbps DPSK signal in the silicon waveguide.
The results presented in Chapter 5 are the outcomes of a collaboration with D. Vukovic (DTU Fotonik) and A. Gajda (Technische Universität Berlin and IHP) carried out at DTU Fotonik. The waveguides have been designed by A. Gajda and fabricated in a Bi-CMOS foundry at IHP, Frankfurt (Oder), Germany.

In Chapter 6, a novel phase-discrimination scheme first proposed by Webb *et al.* [25] is investigated numerically and experimentally to provide QPSK-to-2×BPSK modulation format and wavelength conversion. First, the scheme is introduced and an application to increase the phase-noise tolerance of conventional QPSK receivers is numerically analyzed. Static characterization, i.e. under CW operation, is presented for three different

nonlinear media: a standard Ge-doped HNLF, a PPLN waveguide, and a silicon waveguide, showing similar results. The successful simultaneous recovery of both QPSK field-quadratures is demonstrated at 10-Gbaud. The bit-error ratio (BER) performances measured for the HNLF and the PPLN waveguide highlight similar performances, mainly hindered by a sub-optimum phase-locking feedback scheme employed to compensate for slow thermal phase-drifts between signal and pumps.
The silicon waveguide has been fabricated at IHP as Chapter 5, and the experiments in PPLN have been conducted together with Ass. Prof. Y. Fukichi (Tokyo University of Science).

Chapter 7 concludes the thesis summarizing the key results and it provides a brief outlook on possible future developments of the findings presented here.

Chapter 2

Fundamentals of parametric amplification

2.1 Introduction

This chapter aims at providing a brief introduction on the propagation of optical waves through nonlinear media such as HNLFs or silicon waveguides as well as outlining the key properties of optical parametric amplifiers (OPAs). In Section 2.2, the theory of electromagnetic waves propagation in dielectric media is described starting from the nonlinear Schrödinger equation (NLSE). The different physical effects are separately commented upon with main focus on dispersion and Kerr nonlinearity. Furthermore, the impact of nonlinear absorption in silicon waveguides is discussed, since understanding the repercussion of two-photon absorption (TPA) and free carrier (FC) effects lays the foundations for following the discussion presented in Chapter 5. Finally, scattering processes are also introduced. Parametric amplification is presented in Section 2.3, theoretically discussing the key concepts of phase matching and amplification in phase-insensitive and phase sensitive operation. Stimulated Brillouin scattering (SBS) has strong relevance for the practical realization of OPAs in HNLFs, namely FOPAs. Section 2.4 is therefore specially devoted to commenting on the various techniques employed for stimulated Brillouin scattering (SBS) mitigation highlighting their advantages and limitations. Finally Sections 2.5 and 2.6 present an overview of the stat-of-the-art in applications of OPAs in phase-insensitive and phase-sensitive configurations with a strong focus on FOPAs.

2.2 Optical wave propagation

The propagation of an electromagnetic wave through a dielectric medium is described by Maxwell's equations, which in the case of an homogeneous medium can be combined to derive the wave equation [26]:

$$\nabla \times \nabla \times \mathbf{E} + \frac{1}{c^2}\frac{\partial^2 \mathbf{E}}{\partial t^2} = -\mu_0 \frac{\partial^2 \mathbf{P}}{\partial t^2}\,, \tag{2.1}$$

where $\mathbf{E}$, $\mathbf{P}$, μ_0 and c are the electric field, the induced electric polarization, the vacuum permeability and the speed of light in the medium, respectively.

For optical waveguides, the *weakly guiding approximation* is commonly applied in order to simplify the derivation [26]. Under this condition, the optical field can be assumed as linearly polarized and separable in transverse and longitudinal components as well as decomposed in a fast oscillatory term at a certain optical frequency and in a slowly varying envelope (*slow varying envelope approximation*).

The electrical field can then be expressed as:

$$\mathbf{E} = \hat{\mathbf{x}} F(x,y,t) A(z,t) e^{i(\beta(\omega_0)z - \omega_0 t)}\,, \tag{2.2}$$

with $\hat{\mathbf{x}}$, $F(x,y,t)$, $A(z,t)$, β and ω_0 are the polarization unit vector, the transverse field component (propagation is assumed along z), the field amplitude, the propagation constant and the optical frequency, respectively.

From such an expression, the wave equation (2.1) can be used to derive the NLSE describing the propagation of the field amplitude ($A(z,t)$) through the medium. In order to keep the discussion as general as possible, only the most relevant terms which are discussed in this thesis have been included, even though their relevance is strongly dependent on the specific medium considered.

The NLSE can be expressed as:

$$\frac{\partial}{\partial z}A = -\frac{\alpha}{2}A + \left(\sum_{n=1}^{N}(-i)^{n+1}\frac{\beta_n}{n!}\frac{\partial^n}{\partial t^n}\right)A + i\gamma|A|^2 A - \frac{\beta_{TPA}}{2A_{\text{eff}}}|A|^2 A + i\beta_F A\,, \tag{2.3}$$

where α represents the linear propagation loss term, β_n the n-th order dispersion term, γ and β_{TPA} Kerr and TPA coefficients, A_{eff} the effective area, and β_F the FCs effects. The various terms are discussed separately in the following subsections. In order to keep a simple and compact expression, the contributions of nonlinear scattering effects have been neglected

in Equation (2.3). Nevertheless, stimulated Raman scattering (SRS) and to a larger extent SBS have a significant impact for parametric amplification in HNLFs. Their contribution is therefore still discussed in this section.

2.2.1 Linear losses

An optical wave propagating through a dielectric medium is attenuated by several physical effects such as Rayleigh scattering, scattering from core-cladding interface, and absorption mechanisms.

Concerning the nonlinear media discussed in this thesis, namely germanium-doped HNLFs, silicon waveguides and PPLN waveguides, the different materials and levels of maturity of the fabrication technology lead to diverse linear losses at telecom wavelengths ($\sim$ 1550 nm) as summarized in Table 2.1.

Table 2.1: Typical values for attenuation coefficient (α) at $\sim$ 1550 nm.

Ge-doped HNLF	Si waveguides	PPLN waveguides
0.5-1 dB/km	1-2 dB/cm	<0.1 dB/cm

An important parameter that can be derived from the attenuation coefficient is the effective length (L_{eff}), defined as:

$$L_{\text{eff}} = \frac{1 - e^{-\alpha L}}{\alpha}, \tag{2.4}$$

where L is the physical length.

2.2.2 Chromatic dispersion

As introduced in Equation (2.2), the electrical field propagation along the z-direction is determined by the propagation constant β, which is related to the effective refractive index of the medium via $\beta = \omega n_{\text{eff}}/c$ [20]. The refractive index of dielectric media is frequency dependent and so is, in turn, the propagation constant.

Taylor expanding the propagation constant around the central frequency ω_0 yields to:

$$\begin{aligned}\beta(\omega) \approx \beta_0 + \beta_1(\omega - \omega_0) + \frac{\beta_2}{2}(\omega - \omega_0)^2 + \frac{\beta_3}{6}(\omega - \omega_0)^3 \\ + \frac{\beta_4}{24}(\omega - \omega_0)^4 + \dots,\end{aligned} \tag{2.5}$$

where $\beta_j = (d^j\beta/d\omega^j)_{\omega=\omega_0}$.

By definition the group velocity, i.e. the speed at which the wave envelope propagates, is equal to $v_g = d\omega/d\beta$. A non-zero second-order derivative of β, indicated by β_2, leads, therefore, to a distortion of non-CW signals during their propagation as different frequency components travel with different speeds, i.e. they temporally disperse. The parameter β_2, is thus known as group-velocity dispersion (GVD).

In order to minimize the signal distortion, it is beneficial to operate around the wavelength (λ_0) where $\beta_2 = 0$, that is the zero-dispersion wavelength (ZDW). However, around the ZDW, higher-order derivative of β, such as β_3 and β_4, acquire importance.

Alternatively to β_2 and β_3, it is common to describe the dispersion of optical fibers using the derivatives of β as a function of the wavelength. This leads to defining the *chromatic dispersion coefficient* (D) and the *dispersion slope* (S), expressed as:

$$D = -\frac{2\pi c}{\lambda^2}\beta_2 \qquad S = \left(\frac{2\pi c}{\lambda^2}\right)^2 \beta_3 + \left(\frac{4\pi c}{\lambda^3}\right)\beta_2 \tag{2.6}$$

The chromatic dispersion coefficients as functions of the wavelength for the two HNLFs used throughout this thesis are reported in Fig. 2.1.

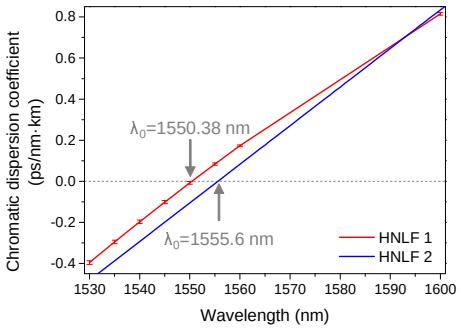

Figure 2.1: Measured chromatic dispersion coefficient for HNLF 1 (used in Chapters 3 and 6) and calculated dispersion coefficient from D and S measured at 1550 nm for HNLF 2 (used in Chapter 4). The measurements have been kindly provided by OFS-Denmark for HNLF 1 and Sumitomo Electrics for HNLF 2.

The dispersion of both HNLFs is designed to have the ZDW around 1550 nm and a low dispersion slope.
Chromatic dispersion is actually the result of two different contributions,

namely *material dispersion*, which depends only on the property of the material, and *waveguide dispersion*, which is instead related to the waveguide geometry. While the material dispersion is rather fixed with only minor effects coming from doping concentrations, the second term is what enables to tune the waveguide dispersion to the desired profile (dispersion engineering) by designing the cross-section of the waveguide itself.

However, the dependence of the dispersion on the waveguide geometry leads to undesirable longitudinal fluctuations of the ZDW due to the limited precision of fabrication processes. Such fluctuations have been measured to reach values as high as 20 nm over 1.7 km for a standard HNLF [27] and they strongly impair the nonlinear interaction (Section 2.3).

Recently improvements in the fabrication techniques and a new fiber design have allowed decreasing such levels down to 0.2 nm for a 100-m long HNLF [28]. Nevertheless, a sub-nanometer precision would be required for optimum nonlinear mixing [29] not yet achievable with current fabrication techniques.

2.2.3 Third-order Kerr nonlinearity

In media with a third-order susceptibility ($\chi^{(3)}$), such as optical fibers and silicon waveguides, the effect of nonlinear polarization can be understood as an intensity dependence of the refractive index. If an electromagnetic wave with power P propagates through the medium, its refractive index changes according to:

$$n = n_0 + n_2 \frac{P}{A_{\text{eff}}}\,, \tag{2.7}$$

with n_0, n_2 and A_{eff} being the material refractive index, the *nonlinear index coefficient* and the effective area of the propagating mode, respectively [26]. The effective area A_{eff} is a fundamental property defining the area of the optical mode and can be calculated according to Equation (2.8)

$$A_{\text{eff}} = \frac{\left(\iint |F(x,y)|^2 dxdy\right)^2}{\iint |F(x,y)|^4 dxdy}\,, \tag{2.8}$$

where $F(x,y)$ represents the transverse component of the optical field. The definition in Equation (2.8) implicitly assumes the weakly guiding approximation. That is not necessarily verified for silicon waveguides where the index contrast between core and cladding is larger than in optical fibers. For silicon waveguides then, also the longitudinal component of the field may need to be taken into account in the calculation as described in [30].

Going back to the NLSE, as in Equation (2.3), the contributions of n_2 appears through the *nonlinear coefficient* (γ) defined as:

$$\gamma = \frac{\omega n_2}{c A_{\text{eff}}} \,. \tag{2.9}$$

As for the dispersion, the nonlinear coefficient is the results of two contributions. On the one side it depends on the chosen medium, through n_2, and on the other side on the waveguide geometry which affects A_{eff}. The effective area can be tuned by designing the waveguide cross-section as well as the refractive index difference between core and cladding and it provides a measure of the confinement of the field.

Typical values of the nonlinear coefficients for Ge-doped silica HNLFs are in the range 5-20$\times 10^{-3}$ W^{-1}·m^{-1}, while the values can be increased to 2-8$\times 10^{2}$ W^{-1}·m^{-1} for silicon waveguides. In silicon, a two-orders of magnitude higher nonlinear refractive index is combined with a smaller effective area of the waveguides (around 0.1 μm^2 unlike the 10 μm^2 of HNLFs) to provide significantly increased nonlinearities.

An intensity dependent refractive index results in several nonlinear effects, the most important in HNLFs and silicon waveguides are self-phase modulation (SPM), cross-phase modulation (XPM) and four-wave mixing (FWM).

When a monochromatic wave at ω_1 propagates through a Kerr medium, its intensity modulates the refractive index and in turn the phase of the wave itself, thus the name of SPM. The phase shift experienced by a wave of power P propagating in a medium characterized by a certain γ and L_{eff} can be simply expressed as:

$$\Phi^{(SPM)} = \gamma P L_{\text{eff}} \,. \tag{2.10}$$

Similarly, when two waves at ω_1 and ω_2 co-propagate through the same nonlinear medium, the phase of the first wave is modulated by the refractive index changes induced by ω_1 itself (SPM) and by ω_2 (XPM). However, due to the form of $\chi^{(3)}$, XPM is twice as effective as SPM, leading to a phase shift on wave one of:

$$\Phi_1^{(XPM)} = 2 \cdot \gamma P_2 L_{\text{eff}} \,. \tag{2.11}$$

Finally, if a third wave (ω_3) is added, other than being affected by SPM and XPM, it is also phase modulated by the beating component at $\omega_1 - \omega_2$ between the first two. This effect results in the creation of sidebands at $\omega_3 \pm (\omega_2 - \omega_1)$. Due to the generation of a forth frequency component

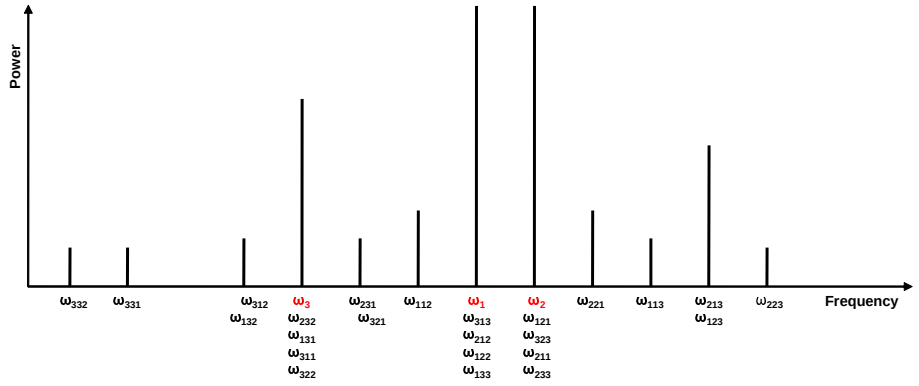

Figure 2.2: FWM products generated from two strong waves at ω_1 and ω_2 and a weak one at ω_3 at the input of a fiber. Inspired by [31], $\omega_{jkl} = \omega_j + \omega_k - \omega_l$.

from the initial three, this process is called FWM and it is used intensively throughout this thesis.
Note that ω_1 and ω_2 are similarly modulated, therefore, out of three initial waves, nine new frequency components, $\omega_{jkl} = \omega_j + \omega_k - \omega_l$, are generated as can be seen in Fig. 2.2. The results of degenerate FWM processes are also included since FWM can also take place if $\omega_1 = \omega_2$, that is if only two waves are co-propagating. FWM is regulated by two conservation rules, namely energy and momentum conservation.
Energy conservation determines the frequency relation between the newly generated waves and the original frequency components.
Conservation of linear momentum then adds a further condition on the phase relation between the waves: $\Phi_4 = \Phi_1 + \Phi_2 - \Phi_3$. As the phase of the waves is related to the propagation constant, it can be written as:

$$\Delta\beta = \beta(\omega_1) + \beta(\omega_2) - \beta(\omega_3) - \beta(\omega_4) = 0\,, \tag{2.12}$$

also known as linear phase matching condition. The FWM efficiency is, therefore, strongly affected by dispersion. As the various interacting frequencies experience different propagation speeds, the resulting walk-off effects disrupt the phase matching condition, decreasing the efficiency.
In Section 2.3, the concept of nonlinear phase matching is introduced, where the nonlinear phase rotation is used to compensate for the dispersion-induced phase-shift. Focusing only on the impact of dispersion, in HNLFs, the walk-off effect is worsened by the presence of the fabrication-induced

dispersion fluctuations as introduced above. HNLFs are designed with a smaller core diameter than conventional standard single mode fiber (SSMF) in order to exploit a higher confinement (lower A_{eff}) to increase the nonlinear coefficient. Therefore, higher fabrication precision would be required to minimize the dispersion fluctuations.
While Kerr nonlinearity is the main source of nonlinearity in HNLFs and silicon waveguides, since the second-order susceptibility ($\chi^{(2)}$) is made null or negligible by the material amorphous structure or its crystal symmetry, that is not the case for PPLN waveguides. In PPLN, $\chi^{(2)}$ effects are dominant. They are classified in second-harmonic generation (SHG), sum-frequency generation (SFG) and difference frequency generation (DFG) and consist on the interaction between two frequency components to generate a third. In this thesis, however, only cascaded SHG and DFG are being used in order to obtain a nonlinear interaction functionally-equivalent to FWM. The cascaded effect can then be described through an induced third-order nonlinearity where $\chi^{(3)}_{\text{eff}} \propto |\chi^{(2)}|^2$ as discussed in [32].
Finally, all the aforementioned processes are characterized by a response time of the order of femtoseconds, making them interesting for all-optical processing of high-bitrate signals [33].

2.2.4 Nonlinear absorption mechanisms

The nonlinear materials discussed here are all transparent at telecom wavelength. However, multi-photon absorption may play a role and needs to be considered.

Germanium-doped silica HNLFs and PPLN waveguides have energy band gaps of around 8.4 eV and 4.0 eV, respectively. Therefore, multi-photon absorption has not been reported even for very high intensity [20].

In contrast, silicon has an energy band gap of around 1.12 eV, corresponding to the energy of a photon at a wavelength of around 1100 nm [34]. While at telecom wavelengths (1550 nm) a single photon has not enough energy to match the bandgap of the material, the simultaneous absorption of two photons does. This effect is therefore called two-photon absorption (TPA) and its impact is significant up to the mid-infrared region and becomes negligible only above 2200 nm [35]. TPA is described by the TPA parameter β_{TPA}, which takes typical values of $3 - 9 \times 10^{-12}$ m/W around 1550 nm and represents an additional loss mechanism.

However, the consequent accumulation of a number of free electrons and holes in the waveguide is even more detrimental. The effect of these

so called free carriers (FCs) is two-fold: on the one side they absorb light causing a third loss mechanism known as free carrier absorption (FCA). On the other side they induce a change in the refractive index of the material, namely free carrier dispersion (FCD). In Equation (2.3), such effects are described by the term β_F which can be expressed as:

$$\beta_F = \frac{n(\omega)}{n_{\text{eff}}} \left(\omega \frac{\sigma_{FCD}}{c} + i \frac{\sigma_{FCA}}{2} \right) N_c \,, \tag{2.13}$$

where σ_{FCD}, σ_{FCA} and N_c are the FCD and FCA cross-sections and the density of FCs, respectively. Typical values for the cross-sections are $\sigma_{FCD} = -5.3 \times 10^{-27} (\lambda/\lambda_r)^2$ m^3 and $\sigma_{FCA} = 1.45 \times 10^{-21} (\lambda/\lambda_r)^2$ m^2 with $\lambda_r = 1550$ nm [36], while the carrier density can be calculated through:

$$\frac{\partial}{\partial t} N_c(z,t) = \frac{\beta_{TPA}}{2h\nu_0} \frac{|A(z,t)|^4}{A_{\text{eff}}^2} - \frac{N_c}{\tau_0} \,, \tag{2.14}$$

where the fundamental parameter is τ_0, called *effective carrier lifetime*, which includes all the effects of recombination, diffusion and drift. Carrier lifetimes of the order of a few nanoseconds have been measured for silicon waveguides [37].
FCA and FCD are the main effects limiting the use of silicon waveguides for nonlinear processing. On the one hand the additional absorption caused by FCA decreases the effective power that can be used for the nonlinear interaction. On the other hand, the refractive index change due to FCD has an opposite sign compared to Kerr nonlinearity therefore further restricting the maximum phase shift achievable [36].

Several methods have been proposed and are being investigated to decrease the carrier lifetime, either acting on the material itself or through additional structures. They are discussed in details in Chapter 5.

2.2.5 Brillouin scattering

Electrostriction is the property of some dielectric materials to become compressed if subjected to a strong electric field. When a strong pump propagates through the medium, variations in the electric field generate changes in the material density and consequently an acoustic wave which, in turn, modulates the medium refractive index with the creation of a Bragg diffraction gratings that back-scatters the light beam. The incident and scattered waves generate an interference pattern, which reinforces the acoustic wave

increasing, in turn, the scattered power. Such self-sustaining effect is known as stimulated Brillouin scattering (SBS).
Nonlinear materials such as silicon and PPLN waveguides may be fairly resilient to SBS, however, this effect represents a major limitation in HNLFs [38–40].

The fundamental parameters defining SBS are the Brillouin frequency downshift (ν_B), the Brillouin gain (g_B), and the Brillouin gain bandwidth ($\Delta\nu_B$). For the conventional Ge-doped HNLFs used throughout this work, typical values for the frequency downshift, Brillouin gain and Brillouin bandwidth are around $\nu_B = 8 - 11$ GHz, $g_B = 3 \times 10^{-11}$ m/W and $\Delta\nu_B$ =10−100 MHz, respectively [38]. The limited Brillouin bandwidth results in a weaker backscattered wave in case of injected waves with a broad linewidth ($\Delta\nu_p$). Under the assumption of an injected wave with a Lorentzian spectral profile, the gain scales approximately as:

$$g_B' = g_B \frac{\Delta\nu_p}{1 + (\Delta\nu_B/\Delta\nu_p)^2}\,, \tag{2.15}$$

where g_B is the peak Brillouin gain [20].
This dependence on the linewidth of the injected wave is a key property for one of the most common suppression technique as discussed in Section 2.4. Since SBS relies on a positive feedback mechanism, a power threshold (P_{th}) can be defined after which the growth of the acoustic wave and back-scattered power start causing a substantial decrease of the incident wave. Fig. 2.3(a) shows output and backscattered powers measured for a 500-m long HNLF (HNLF 1 of Chapters 3 and 6). A linear increase in output power for increasing input levels is clearly visible in the region where Rayleigh scattering is the major backscattering contribution (low power). As SBS becomes dominant, i.e. once the input power reaches $P_{th} \approx 15$ dBm, the output power starts to saturate and the backscattered power increases steeply.

The difference in contribution of Rayleigh and SBS is highlighted in Fig. 2.3(b) where the backscattered power spectra at the input of the HNLF are shown for different input power values as a function of the relative frequency ($\Delta\nu$) with respect to the input wave frequency. The two peaks, at $\Delta\nu = 0$ and $\Delta\nu = 10$ GHz for Rayleigh scattering and SBS, respectively, indeed reach the same height for an input power equals to P_{th}.

Theoretically, it is common to define P_{th} such that the back-scattered power is a percentage μ of the output power. A well-known estimate for

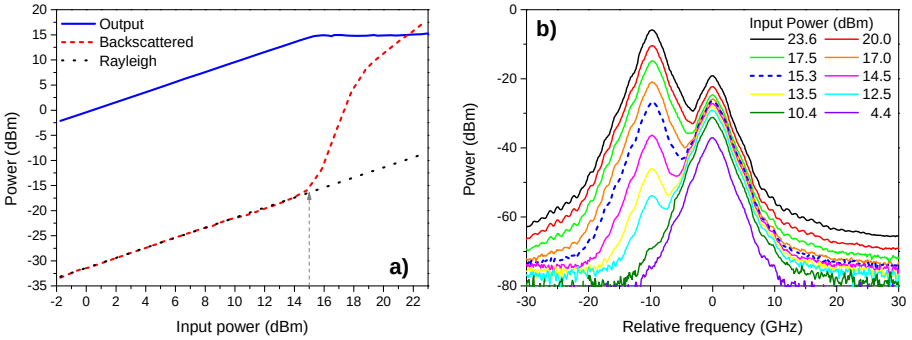

Figure 2.3: (a) Output, backscattered and Rayleigh power as a function of the input power in HNLF 1: the arrow marks P_{th}. (b) Measured backscattered spectra showing the Rayleigh peak and the 10-GHz frequency downshifted SBS peak: the dashed spectrum (15.3 dBm) shows the same peak height for SBS and Rayleigh.

$\mu = 100$ % defines the threshold as:

$$P_{th} = 21\frac{A_{\text{eff}}}{g_B L_{\text{eff}}}\,. \tag{2.16}$$

Even though Equation (2.16) is only an approximation, it has the benefit of underlining the increase of the backscattered power with the optical confinement (decrease of A_{eff}) and with the waveguide length. It becomes clear then that since the backscattering scales with A_{eff} and L_{eff} similarly to the nonlinear phase shift, SBS represents a major issue for nonlinear processing in HNLFs.
Additionally, SBS is also a source of intensity noise induced by the backward propagating wave [41].
Throughout this thesis, SBS has been mitigated, wherever needed, by using phase dithering to broaden the pumps linewidth, as discussed in details in Section 2.4 or keeping the power per optical wave well below P_{th}.

2.2.6 Raman scattering

A second inelastic scattering process, stimulated Raman scattering (SRS) involves, instead, the interaction between an optical wave and the molecular structure of the transmission medium with the generation of optical phonons. The main properties of SRS can be described similarly to SBS, defining a frequency downshift (ν_R), a Raman gain (g_R) and a Raman gain

bandwidth ($\Delta\nu_R$). For HNLFs, typical values are around $\nu_R = 13$ THz, $g_R = 6 \times 10^{-13}$ m/W and $\Delta\nu_R = 1$ GHz [26]. In silicon waveguides, Raman gain values up to three orders of magnitude higher have been reported [42], making SRS a more critical process than in HNLFs where SBS is dominant.

However, due to the relatively narrow bandwidth used for the schemes investigated in this thesis if compared to ν_R, SRS is considered negligible also for silicon waveguides. Only in Chapter 4 SRS is taken into account due to the broadband operation (40 nm) of the scheme discussed. A slight adjustment of the power levels at the HNLF input pre-compensates for the Raman-induced transfer of power from short- to long-wavelengths waves.

2.3 Optical parametric amplifiers

Parametric amplification is a well-known technique to provide amplification and wavelength conversion in materials characterized by $\chi^{(2)}$ [43] or $\chi^{(3)}$ [31] nonlinearity.
As discussed in Section 2.2, cascaded $\chi^{(2)}$ effects can be considered equivalent to $\chi^{(3)}$ effects, therefore in the following the derivation is mainly focused on Kerr nonlinearity. The discussion can, however, be easily extended to SHG/DFG and SHG/SFG.
The FWM interaction between three optical waves, two strong pumps (ω_1 and ω_2) and a weak signal (ω_3), leads to the generation of nine new frequency components. However, out of those nine, only the strongest is usually considered for practical applications and corresponds to the idler at $\omega_4 = \omega_1 + \omega_2 - \omega_3$. Fig. 2.4 shows the frequency allocation of the three waves involved in the FWM interaction covering the three scenarios of main interest for parametric amplification: a dual-pump non-degenerate OPA, a dual-pump degenerate signal-idler OPA and a single-pump OPA respectively. The two latter configurations are actually degenerate cases of the first: a signal-idler degenerate ($\omega_3 = \omega_4$) and a pump degenerate ($\omega_1 = \omega_2$) case, respectively.

Starting from the more general case of a dual-pump non-degenerate OPA and assuming co-polarized waves, the NLSE (2.3) can be split into four

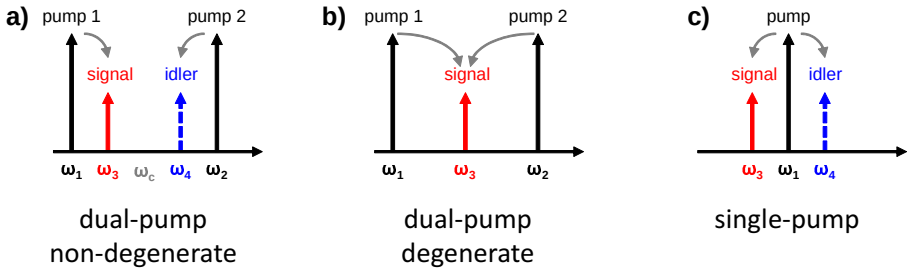

Figure 2.4: Wavelength allocation and nomenclature of the waves involved in the FWM interaction for (a) a dual-pump non-degenerate OPA, (b) a dual-pump signal-idler degenerate OPA, and (c) a single-pump OPA.

coupled propagation equations, one for each wave, leading to:

$$\frac{dA_1}{dz} = i\gamma \left[|A_1|^2 A_1 + 2\sum_{l\neq 1} |A_l|^2 A_1 + 2A_3 A_4 A_2^* e^{i\Delta\beta z} \right], \tag{2.17}$$

$$\frac{dA_2}{dz} = i\gamma \left[|A_2|^2 A_2 + 2\sum_{l\neq 2} |A_l|^2 A_2 + 2A_3 A_4 A_1^* e^{i\Delta\beta z} \right], \tag{2.18}$$

$$\frac{dA_3}{dz} = i\gamma \left[|A_3|^2 A_3 + 2\sum_{l\neq 3} |A_l|^2 A_3 + 2A_1 A_2 A_4^* e^{-i\Delta\beta z} \right], \tag{2.19}$$

$$\frac{dA_4}{dz} = i\gamma \left[\underbrace{|A_4|^2 A_4}_{SPM} + \underbrace{2\sum_{l\neq 4} |A_l|^2 A_4}_{XPM} + \underbrace{2A_1 A_2 A_3^* e^{-i\Delta\beta z}}_{FWM} \right], \tag{2.20}$$

where $\Delta\beta$ depends on the dispersion properties of the medium as defined in Equation (2.12). Linear losses as well as TPA and FC effects are being neglected to keep the focus on the interaction between Kerr nonlinearity and dispersion providing parametric amplification.

These field equations can be rewritten by defining $A_i(z) = \sqrt{P_i(z)} e^{\Phi_i(z)}$ in order to highlight the evolution of the power of each wave as well as their

relative phase $\theta_{rel} = \Delta\beta + \Phi_4(z) + \Phi_3(z) - \Phi_2(z) - \Phi_1(z)$:

$$\frac{dP_1}{dz} = \frac{dP_2}{dz} = -4\gamma\sqrt{P_1P_2P_3P_4}\sin(\theta_{rel})\,, \tag{2.21a}$$

$$\frac{dP_3}{dz} = \frac{dP_4}{dz} = +4\gamma\sqrt{P_1P_2P_3P_4}\sin(\theta_{rel})\,, \tag{2.21b}$$

$$\begin{aligned}\frac{\partial\theta_{rel}}{\partial z} =& \Delta\beta + \gamma(P_1 + P_2 - P_3 - P_4) + \\ &+ 2\gamma\sqrt{P_1P_2P_3P_4}\left(\frac{1}{P_3} + \frac{1}{P_4} - \frac{1}{P_1} - \frac{1}{P_2}\right)\cos(\theta_{rel})\,.\end{aligned} \tag{2.21c}$$

From Equations (2.21a) and (2.21b), it is clear that, in absence of losses the power gets transferred from pumps to signal and idler, or vice versa, according to the relative phase θ_{rel} between the waves.

Starting from such coupled equations, the fundamental properties of OPAs in terms of phase matching condition and gain spectrum, as well as gain saturation and phase-sensitive amplification, are discussed in details in the following.

2.3.1 Phase matching condition

Momentum conservation is fundamental for FWM and parametric interaction in general. The requirement translates directly into a condition on the relative phase difference θ_{rel} between the interacting waves.
Assuming $\theta_{rel} \approx \pi/2$, i.e. close to phase-matching condition, the term depending on $\cos(\theta_{rel})$ in Equation (2.21c) can be neglected and a *phase matching parameter* (κ) can be defined as:

$$\frac{\partial\theta_{rel}}{\partial z} \approx \Delta\beta + \gamma(P_1 + P_2 - P_3 - P_4) = \Delta\beta_L + \Delta\beta_{NL} = \kappa\,, \tag{2.22}$$

The parameter κ consists of the sum of two contributions: the linear part ($\Delta\beta_L$) defined in Equation (2.12) and a nonlinear term ($\Delta\beta_{NL}$) related to the nonlinear phase shift due to SPM and XPM.

Disregarding the case of strong pump depletion, i.e. assuming $P_1+P_2 \gg P_3+P_4$, the nonlinear contribution is always positive and can be canceled out only by ensuring a negative $\Delta\beta_L$. The desired condition $\kappa = 0$ that maximizes FWM efficiency [20] can then be achieved.

In a dual-pump OPA, the phase matching condition can be expressed Taylor expanding $\beta(\omega)$ around the zero-dispersion frequency ω_0:

$$\kappa = \beta_3(\omega_c - \omega_0)\cdot\left[(\omega_3 - \omega_c)^2 - \omega_d^2\right] + \Delta\beta_{NL} = 0\,, \tag{2.23}$$

where $\omega_c = (\omega_1 + \omega_2)/2$ and $\omega_d = (\omega_1 - \omega_2)/2$. Furthermore, ω_c is assumed to be close to ω_0 such that second-order dispersion effects can be neglected. For a single-pump OPA, a similar relation can be derived directly from Equation (2.23) just setting $\omega_c = \omega_1$ and $\omega_d = 0$.

These relations highlight the need to operate with the pump average frequency (ω_c) in the anomalous dispersion regime of the medium in order to have a negative linear phase matching contribution. For example, standard HNLFs are typically characterized by a positive dispersion slope as shown in Fig. 2.1, the phase-matching condition thus requires $\omega_c < \omega_0$ or alternatively $\lambda_c > \lambda_0$ as discussed in the following subsection.

Furthermore, the phase-matching properties are strongly dependent on the dispersion slope β_3. The smaller the slope, the lower the frequency dependence of κ and the broader the frequency region over which $\kappa \approx 0$ can be achieved. This consideration helps understanding the need for a central frequency in the anomalous dispersion regime but still close to ω_0.

2.3.2 Phase-insensitive gain

The nonlinear phase shift is not only critical in defining the phase matching condition, but also determines the achievable signal gain. This can be clearly seen from Equation (2.21b) where the growth of signal and idler is proportional to $\gamma P_1 P_2$.

If two strong pumps and a signal are injected into the nonlinear medium, an idler is then immediately generated from vacuum fluctuations by the other interacting waves [31].
Using Equation (2.17) and considering that $A_4(0) = A_i(0) = 0$, then, after an infinitesimal propagation length δz the idler field can be approximated as:

$$A_i(\delta z) = i\gamma A_{P1} A_{P2} A_s^* e^{-i\Delta\beta\,\delta z}\delta z\,, \tag{2.24}$$

where the indexes $P1$, $P2$, s and i have been used to highlight more explicitly the roles of pumps, signal and idler, and correspond to 1, 2, 3 and 4, respectively. The phase of the idler can be derived from Equation (2.24) resulting in $\Phi_i = \pi/2 + \Phi_{P1} + \Phi_{P2} - \Phi_s - \Delta\beta\delta z$. The relative phase $\theta_{rel} = \pi/2$, and thus power flows from the pumps to signal and idler [31].

Under the assumptions of lossless medium, no pump depletion (P_{P1}, $\mathrm{P}_{P2} \gg \mathrm{P}_s$) and negligible signal and idler SPM and XPM effects (weak signal), an expression for the signal gain and idler conversion efficiency (CE)

can be easily derived [20]:

$$G = \frac{P_s(L)}{P_s(0)} = \left(1 + \left|\frac{\eta\gamma\sqrt{P_{P1}P_{P2}}}{g}\sinh(gL)\right|^2\right), \tag{2.25}$$

$$\mathrm{CE} = \frac{P_i(L)}{P_s(0)} = \left(\left|\frac{\eta\gamma\sqrt{P_{P1}P_{P2}}}{g}\sinh(gL)\right|^2\right), \tag{2.26}$$

where $\eta = 1$ and 2 for single- and dual-pump, respectively, and the parametric gain coefficient is given by:

$$g^2 = \left[(\eta\gamma\sqrt{P_{P1}P_{P2}})^2 - (\kappa/2)^2\right], \tag{2.27}$$

A comparison between the two expression highlights that in the high gain regime, the difference between gain and CE becomes negligible.
For a single-pump OPA and assuming a large nonlinear phase shift (high g), Equation (2.26) can be particularized under two conditions: a signal located around the phase matching wavelength ($\kappa \approx 0$) and a signal close to the pump ($\kappa \approx 2\gamma P_{P1}$).
In the first case, Taylor expanding Equation (2.26), yields:

$$G \approx \frac{1}{4}\exp 2\gamma P_{P1} L_{\mathrm{eff}}\,. \tag{2.28}$$

Equation 2.28 shows that the gain increases exponentially with the nonlinear phase shift, therefore, the wavelength region in which nearly perfect phase matching ($\kappa \approx 0$) can be achieved is known as *exponential gain region.*

In the second case, instead, the expression can be simplified as in [31] leading to a quadratic dependence between gain and nonlinear phase shift. This wavelength region is known as *quadratic gain region* with the gain expressed as:

$$G \approx (2\gamma P_{P1} L_{\mathrm{eff}})^2 \tag{2.29}$$

Two examples of gain spectra for a single- and dual-pump OPA, respectively, are shown in Fig. 2.5. The spectra have been obtained solving the coupled equations (2.17) for a 500-m long HNLF (HNLF 1) with nonlinear coefficient, ZDW and dispersion slope equal to $\gamma = 11.7$ W^{-1}·km^{-1}, $\lambda_0 = 1550.4$ nm and $S = 0.0185$ ps/nm·km, respectively, and a total pump power of 30 dBm. In the following, all the figures show results obtained

simulating the propagation into this HNLF. However, identical consideration can be drawn for OPAs based on other second- or third-order nonlinear media.

In Fig. 2.5, for both FOPA configurations, two central wavelengths 0.5 nm above and below the ZDW have been considered.

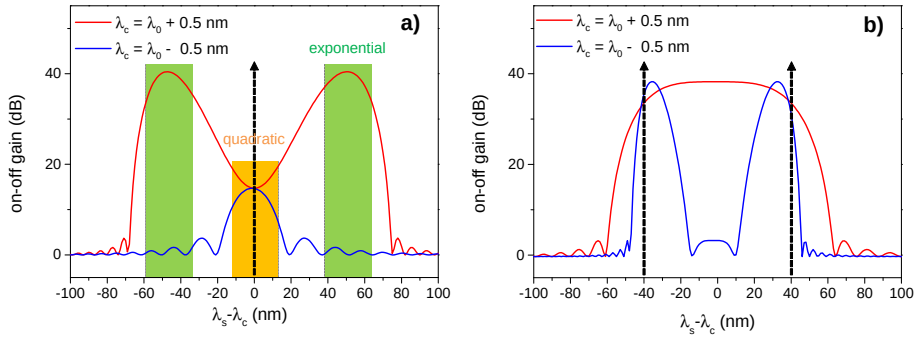

Figure 2.5: Gain spectra for (a) single- and (b) dual-pump FOPA: HNLF 1 characterized by L=500 nm, $\gamma = 11.7$ W^{-1}·km^{-1}, λ_0 1550.4 nm and S=0.0185 ps/nm·km respectively and 30 dBm of total pump power. In (a) exponential (green) and quadratic (orange) gain regions are highlighted.

As discussed above, the central wavelength needs to be positioned in the anomalous dispersion regime in order to obtain a negative linear phase matching and thus cancel out the nonlinear contribution. For a nonlinear medium with a positive dispersion slope S, the condition translates into $\lambda_p > \lambda_0$. If the central wavelength is below the ZDW, amplification can still be achieved but the efficiency is limited in value and bandwidth by the phase mismatch.

A comparison between the gain spectra achievable in single- and dual-pump configurations, shows the advantages of a dual-pump scheme. For a single-pump OPA, only two signal frequencies satisfy the condition $\kappa = 0$, i.e. $\omega_s = \omega_c \pm \sqrt{2\gamma P_P/(\beta_3(\omega_c - \omega_0))}$ with quadratic and exponential gain regions clearly visible in Fig. 2.5(a). In a dual-pump OPA, instead, thanks to the extra degree-of-freedom given by the additional frequency component, a broad range of frequencies can achieve $\kappa \approx 0$.
Furthermore, similar gain levels can be achieved for the same total pump power in the two cases, therefore only half power per pump is required in a dual-pump OPA with additional benefits in terms of SBS.

Finally, the scaling of the gain with the pump power can be seen from

the spectra of Fig. 2.6 for a single-pump OPA.

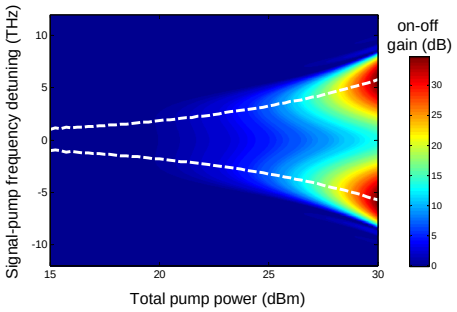

Figure 2.6: Evolution of the parametric gain spectra as a function of the pump power and the signal-pump frequency detuning for a single-pump FOPA: white dashed lines mark the phase matching wavelengths.

It is important to remark that, as the phase matching condition depends on the pump power through $\Delta\beta_{NL}$, higher pump powers shift the position of the maxima, i.e. the phase-matched wavelengths, further away from the pump wavelength as highlighted by the dashed lines.

2.3.3 Gain saturation

The analysis of the gain has been carried out, so far, under the assumption of undepleted pumps. However, as the pumps provide gain to signal and idler, their power will inevitably decrease. It is therefore intuitive to expect a decrease in gain as the signal power increases.

This effect can be seen from Equation (2.21), considering that the relative phase θ_{rel} defines the direction of the power flow: either from the pumps to signal and idler or vice versa. The strength of the power flow decreases with the difference in power between pumps and signal and idler, and the flow reverses direction once signal and idler become comparable in power with the pumps.

However, in Equation (2.21) the effects of SPM and XPM on signal and idler have been neglected. Such assumption is not satisfied anymore as the power of the two waves grows.
The simple model based on coupled equations is not sufficient to accurately describe saturation effects. The full NLSE equation needs to be considered and it has been solved using the split-step Fourier method described in Appendix A.

The same gain spectra as in Fig. 2.5(a), i.e. for a single-pump FOPA, have been calculated varying the input signal power. As the input signal power increases, the pump gets depleted ultimately resulting in the gain reduction highlighted in Fig. 2.7(a). The shaping of the gain spectrum due to saturation affects mainly the exponential gain regions, i.e. the regions where the gain is the highest, while the quadratic region is not affected.

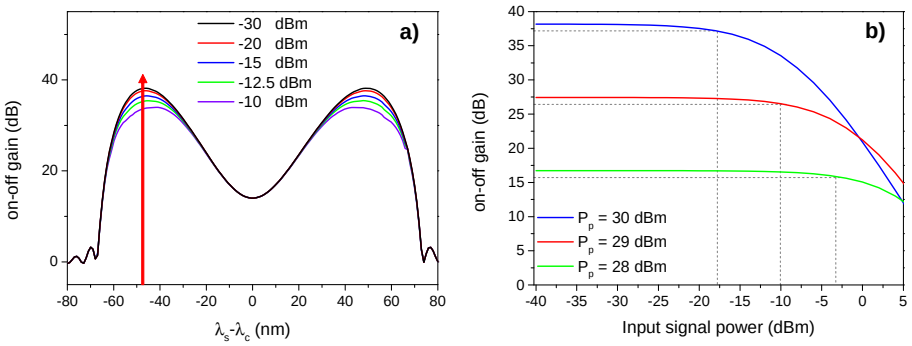

Figure 2.7: (a) Gain spectra for different input signal powers highlighting the saturation effects in the exponential gain region for 30 dBm of pump power. (b) Signal gain ($\lambda = 1503$ nm, red arrow in (a)) as a function of the input signal power for three different pump power levels: dashed lines mark the 1-dB saturation power.

The gain has also been calculated focusing on the performances of a signal located at $\lambda_s = 1503$ nm, i.e. approximately at the phase-matching wavelength. In this case, three different pump power values have been considered, resulting in the curves of Fig. 2.7(b). Saturation kicks off for lower input signal powers when the pump power is increased. A higher pump power means higher gain and in turn higher pump depletion. Defining the saturation threshold as the input signal power leading to a 1-dB gain reduction, the simulations show a threshold of around -18 dBm, -10 dBm and -3 dBm for 30 dBm, 29 dBm and 28 dBm of pump power, respectively.

The saturation properties can be directly related to the power ratio between the pump at the nonlinear medium input and the signal at the output ($P_p(0)/P_s(L)$) as proposed in [24] and discussed further in Section 3.3.

2.3.4 Phase-sensitive amplification

In the discussion so far, it has always been assumed that only pumps and signal are injected into the nonlinear medium. The idler phase then auto-

matically fulfills $\theta_{rel} = \pi/2$ and the change in direction of the power flow can be obtained through variations in the power balance between the waves via the nonlinear component of phase-matching.

However, if also an idler is present at the OPA input, the parametric process can be controlled by tuning the phase relation between the waves. Starting once again from the coupled equations (2.17) and assuming unsaturated operation, a simple relation can be derived linking the fields of signal and idler at the OPA output to their fields at the input [44, 45].

$$\begin{aligned} A_s(z) &= \mu(z)A_{s,0} + \nu A^*_{i,0}\,, \\ A^*_i(z) &= \nu^*(z)A_{s,0} + \mu^*(z)A^*_{i,0}\,, \end{aligned} \tag{2.30}$$

where $A_{s,0} = A_s(0)$, $A_{i,0} = A_i(0)$ and

$$\mu(z) = \cosh(gz) + i\frac{\kappa}{2g}\sinh(gz)\,, \qquad \nu(z) = i\eta\gamma\frac{\sqrt{P_{p1}P_{p2}}}{g}\sinh(gz)\,, \tag{2.31}$$

satisfying the relation $|\mu(z)| - |\nu(z)|^2 = 1$, with $\eta = 1$ and 2 for single- and dual-pump, respectively.
From Equation (2.30), an expression for the output signal power and phase can be easily derived [46]:

$$P_s(L) = |\mu|^2 P_{s,0} + |\nu|^2 P_{i,0} + 2|\mu||\nu|\sqrt{P_{s,0}P_{i,0}}cos(\Delta_\Phi)\,, \tag{2.32a}$$

$$\Phi_s(L) = \arctan\left(\frac{|\mu|\sqrt{P_{s,0}}\sin(\Phi_\mu + \Phi_{s,0}) + |\nu|\sqrt{P_{i,0}}\sin(\Phi_\nu + \Phi_{i,0})}{|\mu|\sqrt{P_{s,0}}\cos(\Phi_\mu + \Phi_{s,0}) + |\nu|\sqrt{P_{i,0}}\cos(\Phi_\nu + \Phi_{i,0})}\right), \tag{2.32b}$$

where Φ_μ and Φ_ν are the phases of the complex coefficients μ and ν, respectively, and $\Delta_\Phi = \Phi_\mu - \Phi_\nu + \Phi_{s,0} + \Phi_{i,0}$. Assuming perfect phase matching ($\kappa = 0$) and equal input power for signal and idler, the signal gain can be derived as:

$$G_s(z) = \cosh(2gz) + \sinh(2gz)\sin(\Phi_{s,0} + \Phi_{i,0})\,. \tag{2.33}$$

The gain is therefore defined by the phase relation between signal and idler at the OPA input.
For phase-sensitive processes, it is of great interest to consider the maximum

amplification and de-amplification (minimum gain) achievable, which are expressed as:

$$\begin{aligned} G_{max} &= \exp\left(+2gz\right), \qquad \text{for} \quad \Phi_{s,0} + \Phi_{i,0} = \pi/2\,, \\ G_{min} &= \exp\left(-2gz\right), \qquad \text{for} \quad \Phi_{s,0} + \Phi_{i,0} = -\pi/2\,. \end{aligned} \tag{2.34}$$

These conditions on the phase relation between signal and idler differ from the perhaps expected requirements for constructive (2π phase difference) and destructive interference (π phase difference). However, the additional $\pi/2$ phase rotation can be understood noticing that all the OPA configurations of Fig. 2.4 lead to a phase-conjugation relation between signal and idler.

It is interesting, then, to compare the maximum gain achievable for an OPA in phase-insensitive (Equation (2.28)) and phase-sensitive (Equation (2.34)) operation. From these equations, it is clear that a four-fold increase in the gain can be obtained once the idler is injected together with the signal into the nonlinear medium, i.e. by only doubling the input power. The 6-dB improvement provided by the phase-sensitive configuration can, however, only fully be reached assuming a large gain (exponential gain region) and proper optimization of phase and amplitude of the idler. As discussed above, a phase detuning leads to a decrease in the gain with a periodicity of π. Similarly, a power imbalance between signal and idler decreases the efficiency of the interference and in turn the gain, as discussed for a dual-pump non-degenerate FOPA in [47].
The normalized signal gain as a function of the input signal phase is shown in Fig 2.8(a) for a dual-pump signal-idler degenerate OPA (see Fig. 2.4).

The curves have been numerically simulated using the coupled equations of (2.21), adjusted to account for the degenerate signal-idler configuration [20]. Pumps wavelengths and HNLF are the same as for Fig. 2.5. For the sake of an easier comparison, the curves for different pump powers have been phase-shifted to align the gain minima to the same input signal phase. Being $\theta_{rel} \propto \gamma\sqrt{P_{p1}P_{p2}}L$, as the pumps power levels increase the gain trends are phase-shifted. However, the artificial shift to align them corresponds simply to a phase shift of the pumps to compensate for the nonlinear rotation.

To evaluate the impact of the pump power on the phase-sensitive gain, a commonly used and easy to measure metric is the PER defined as the ratio between maximum and minimum gain. As shown by Equation (2.34), maximum and minimum gain are connected by $G_{max} = 1/G_{min}$, therefore

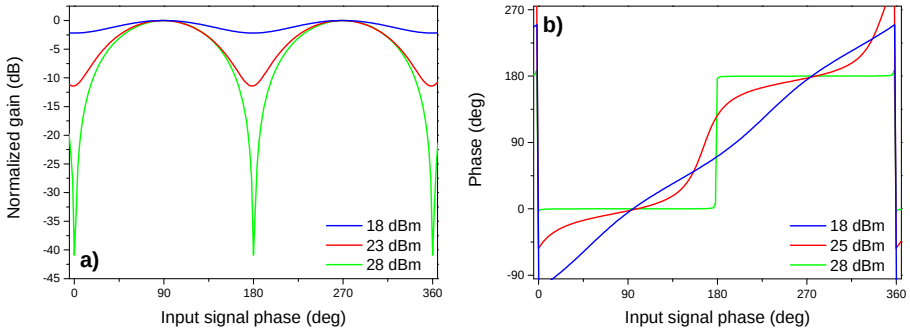

Figure 2.8: (a) Normalized gain and (b) output signal phase as a function of the input signal phase for a dual-pump signal-idler degenerate OPA for different total pump power levels. Pumps wavelengths and HNLF parameter are the same as in Fig. 2.5.

the PER is simply the square of the maximum gain.
In Fig 2.8(a), the three total pump power levels lead to significant difference in the achievable PER. A good understanding of this effects comes immediately comparing the expression for gain and CE in Equation (2.26). In an OPA operating in the high pump power regime, the difference between signal gain and idler CE becomes negligible, therefore automatically ensuring similar power levels for signal and idler, which maximize the phase-sensitive interaction. A low pump power, instead, results in a sub-optimum interference between the degenerate waves and in turn a lower PER.

Other than controlling the gain through the signal phase, another major property of phase-sensitive amplification (PSA) is its ability to provide an output signal phase characterized by two discrete phase states. Assuming once again perfect phase-matching, equal signal and idler power and equal phases ($\Phi_{s,0} = \Phi_{i,0}$), the output signal phase can be derived as [46]:

$$\Phi_s(L) = \arctan\left(\frac{\cosh(2gL)\sin(\Phi_{s,0}) + \sinh(2gL)\cos(\Phi_{s,0})}{\cosh(2gL)\cos(\Phi_{s,0}) + \sinh(2gL)\sin(\Phi_{s,0})}\right). \quad (2.35)$$

In the limit of large gain (gL»1), the argument of the arctangent tends towards one, i.e. a function with two discrete states as highlighted in Fig 2.8(b) where the output signal phase is shown as a function of the input signal phase.

The output signal phase for a total pump power of 28 dBm shows the aforementioned arctangent trend which is most beneficial for providing phase regeneration for two-phase level signals such as BPSK signals. This

is introduced in Section 2.6 and discussed later on throughout Chapters 5 and 6. However, decreasing the pump power, and consequently the gain, the step-like transfer function becomes less steep reaching an almost linear trend.

Notice that the flatness of the output phase transfer function is critical for such applications, but rather difficult to measure experimentally. The preferred metric to determine the phase-regeneration capabilities of an OPA is, instead, the PER, as it can be directly linked to the transfer function of the output signal phase through the phase-sensitive gain. The relation is clearly visible comparing Figs. 2.8(a) and (b).

2.4 Brillouin scattering suppression techniques

High gain OPAs are desirable for both phase-insensitive and phase-sensitive amplification. However, as discussed in Section 2.2.5, in fiber-based OPAs (FOPAs) SBS provides a major limitation to the pump power that can be effectively used for the parametric interaction.
A strong effort has therefore been directed towards decreasing the impact of SBS in FOPAs with various techniques being investigated.
The most promising approaches are:

- Techniques acting physically on the fiber.
  - *Fiber-core doping* to reduce the Brillouin gain (g_B).
  - *Temperature and strain gradients* to vary the Brillouin shift (ν_B) along the fiber and generate backscattered waves which are spectrally overlapping only partially.
- *In-line isolators* to periodically block the backscattered wave.
- *Pump spectral broadening* beyond the Brillouin bandwidth ($\Delta\nu_B$) such that the various frequency components lead to contributions which are spectrally overlapping only partially.

Each of those techniques has advantages and disadvantages, and is therefore suitable for different applications, as discussed below.

2.4.1 Fiber-core doping

Coupling between acoustic and optical modes is fundamental to provide the positive feedback that seeds the growth of SBS. Decreasing the overlapping

between the two modes significantly increases the SBS threshold. Standard HNLFs make use of germanium doping in the fiber core to enhance the nonlinear index. If Al_2O_3 is introduced as an additional dopant, the strength of the coupling between acoustic and optical waves can be reduced. In fact, aluminum has the property of increasing the refractive index at optical frequencies while decreasing it at acoustic frequencies [48–50]. This approach has been successfully demonstrated to enhance the Brillouin threshold [51] with only minor decrease in nonlinearities. The main drawback of this solution is, however, the strong increase in propagation losses with first demonstration reporting values as high as 15 dB/km [51]. Further improvement led to a decrease in the value down to 7 dB/km [52], still one order of magnitude higher than common values for purely Ge-doped HNLFs (0.7 dB/km).
Additionally, Al-doping leads to challenges in terms of splicing to SSMFs, with splicing losses above 1.5 dB/splice.
Nevertheless, such Al-doped HNLFs have been successfully used for providing phase-sensitive functionalities [53–55].

2.4.2 Temperature and strain gradients

Temperature or strain gradients applied to the fiber aim at generating a non-uniform Brillouin shift along the fiber such that a only partial overlap between the Brillouin gain spectra along the fiber seeds less efficiently the backscattered wave. Even though temperature gradients have been successfully demonstrated [56], straining enables a more permanent solution not requiring active temperature control of the fiber [51, 57–60].
Additionally, straining can be optimized and applied to Ge-doped HNLF whose fabrication technology has reached a good level of maturity, unlike for the Al-doping solution.
An example of measured Brillouin gain spectrum with and without straining is shown in Fig. 2.9 from [59]. Straining has the clear effect of broadening the gain spectrum and thus reducing the total backscattered power.

However, a major drawback of generating non-uniformity along the fiber is that not only SBS is affected, but also the dispersion properties of the fiber are impacted leading to a dispersion gradient.
As discussed in the previous section, the dispersion properties are critical for parametric amplification as they control the phase-matching condition. While in a specific demonstration it has been shown that straining can be used to actually remove existing dispersion fluctuations [61], in general a dispersion gradient is strongly detrimental in a FOPA as it causes a decrease

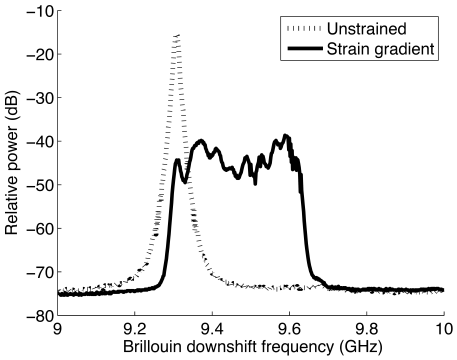

Figure 2.9: Measured Brillouin gain spectrum of an HNLF with and without straining from [59].

in both gain and amplification bandwidth.
Recently, two potential solutions to this issue have been proposed, either relying on designing a fiber with the desired dispersion fluctuations to be removed by the straining, i.e. pre-distorting the fiber dispersion [62], or more promisingly by designing and fabricating HNLFs robust against strain-induced dispersion variations [63, 64].
Nevertheless, as underlined in [64], straining has a detrimental impact worsening polarization-mode dispersion.

2.4.3 In-line isolators

Isolators inserted in between HNLF segments allow blocking the backscattered wave. Considering two fiber segments with an isolator in between, the Brillouin field generated in the second segment, if sufficiently attenuated by the isolator, does not seed efficiently the backscattered wave in the first segment which needs to start growing from a lower level as sketched in Fig. 2.10(a). Even though the need of suppression in excess of 80 dB has been theoretically forecasted for this scheme to provide effective suppression [65], benefits have still been experimentally demonstrated [60, 66]. One main challenge of the scheme is, however, the phase-mismatch between the interacting waves introduced by the propagation through the isolator, especially if SSMF pigtailed. Fig. 2.10(b) shows some simulation results where the same configuration and HNLF property as in Fig. 2.5 have been used but the fiber has been split into two 250-m long segments with a length of SSMF in between.

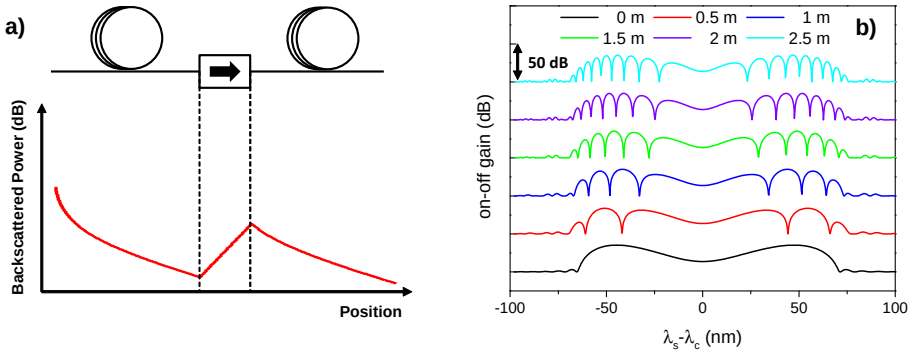

Figure 2.10: (a) Backscattered power evolution along two HNLF segments with an isolator in between. (b) Single-pump FOPA gain assuming an isolator with pigtails of increasing length in between two 250-m long HNLF segments. The lengths refer to the overall pigtails length (assumed SSMF) and the spectra have been translated for clarity.

The calculated spectra clearly show the decrease in gain bandwidth as well as the presence of side lobes due to phase-sensitive interaction, even for such short lengths of SSMF pigtails. In order to solve this issue, pigtail lengths of the order of a few centimeters are needed [60].
Additionally another limitation of this solution is the poor scalability due to the insertion losses of the isolators which have been neglected for the calculations of Fig. 2.10.

2.4.4 Pump spectral broadening

Other than acting on the nonlinear medium, one of the most-common technique used to increase the SBS threshold of an optical fiber relies on modifying directly the high-power optical wave. In Equation (2.15) the dependence of the Brillouin gain on the optical wave linewidth clearly highlights that spectrally broadening the pump allows weakening the backscattered wave. Intuitively, this can be understood in the sense of different spectral components leading to only partially overlapping Brillouin spectra, achieving a similar effect as with a non-uniform Brillouin shift. The most straightforward method to broaden a CW wave is through modulation, either in amplitude or in phase. Amplitude modulating the wave acting as a pump in an OPA automatically results in gain modulation of the signal, that is amplitude noise. Phase modulation, instead, does not get transferred to the signal [20], and even though it affects phase matching, which may result

in amplitude noise as well, its impact is lower, hence making it a preferable choice.
Phase modulation has been implemented for SBS suppression either using a number of radio frequency (RF) tones [67], electrical white noise [68,69] or pseudo-random binary sequences (PRBSs). The use of RF tones is, however, the most common technique since it has shown to lead to lower performance degradation compared to using PRBSs [70]. Additionally, external modulation is preferred compared to direct laser modulation [67].

The chosen frequency values as well as their modulation indices are critical in determining the increase in SBS threshold. First of all, the aim is to obtain side bands that are not spectrally overlapping, therefore the lowest modulation frequency should be chosen higher than twice the Brillouin gain bandwidth ($\Delta\nu_B$). Then, defining the modulation index as $\pi/2$-times the ratio of the peak-to-peak voltage of the driving signal to the half-wave voltage of the phase modulator (see Appendix B), a modulation index of $\sim$1.44 leads to the generation of two side bands of equal amplitude as the original optical carrier [71]. Splitting the pump spectrum into three components spaced by more than $2 \times \Delta\nu_B$ leads to an increase in the power threshold by a factor 3 (5 dB).
Generalizing the reasoning for N modulation tones, if the RF tones are spaced such that $f_{i+1} > 3 \times f_i$, and the same modulation index of 1.44 is used for each tone, the power of the original optical carrier can be split into 3^N spectral components. As the Brillouin spectra of two components so generated do not overlap, a SBS threshold improvement equal to $N \times 5$ dB can be expected.

The benefits of pump broadening can be clearly seen in Fig. 2.11, where the backscattered power as a function of the input power is reported for different number of modulating tones.

Each added modulation tone leads to an increase in P_{th} of approximately 4.5 dB in fairly good agreement with the theoretical 5 dB.
Even though the scheme is suitable for a FOPA providing amplification, by using one of the configurations of Fig. 2.4 for applications requiring wavelength conversion, the pump phase modulation gets transferred to the newly generated idler degrading its performances [72]. In fact, in a single-pump FOPA through FWM the phase modulation applied to the pump is mapped into the idler multiplied by two since $\Phi_i = 2 \cdot \Phi_p - \Phi_s$. One way of overcoming this source of degradation for the idler requires to use a dual-pump FOPA, where the phase of the idler in this case can be expressed as $\Phi_i = \Phi_{p1} + \Phi_{p2} - \Phi_s$. If the two pumps are phase-conjugated, the con-

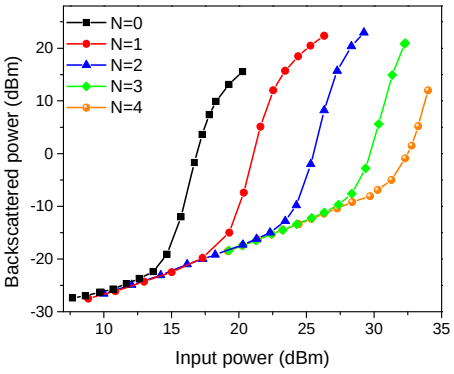

Figure 2.11: Backscattered power as a function of the input power for a number N of modulating tones, spacing from 0 up to 4, corresponding to 75 MHz, 275 MHz, 875 MHz and 2.71 GHz. These measurements have been obtained from a polarization-maintaining HNLF different from HNLF 1.

tributions to the idler phase coming from the pumps cancel out [73, 74]. This approach is known as counter-phasing [75] and it can be practically implemented independently modulating the two pumps with two identical electrical signals having a relative delay such that the pumps are phase conjugated in the FOPA.
Alternatively, counter-phasing could be achieved all-optically using an additional FWM stage for the pumps generation [76]. In case of broadband operation though, dispersion leads to a significant walk-off between the pumps and consequently to a sub-optimum counter-phasing which degrades the idler performances [77]. While walk-off effects can be compensated for by tuning the relative delay in the first scheme, the all-optical approach may give a lower flexibility.
Similar techniques can also be applied when avoiding the phase-conjugation of the field is required. Choosing an idler generated through a so called Bragg-scattering process, i.e. with a phase given by $\Phi_i = \Phi_s - \Phi_{p1} + \Phi_{p2}$, co-phasing of the pumps can be applied to obtain the cancellation of phase modulation transferred from the two pumps [78].
An even more interesting approach recently proposed allows to remove not only the transfer of phase modulation but even the inherent phase noise due to the laser linewidth. This scheme relies on the use of pumps which are both phase-coherent and phase-correlated [79].
While these solutions are simple and effective for phase-insensitive applications, using phase-modulation for PSA is challenging as it may disturb the

phase coherence between the interacting waves [54].
For PSA applications, then, fiber straining or Al-doping are more suitable solutions to decrease the impact of SBS.

2.5 Applications of phase-insensitive amplifiers

Parametric amplification can be used to implement several critical functionalities in an optical communication system, ranging from pure amplification to wavelength conversion and all-optical signal regeneration. This section gives a brief overview of the most important achievements demonstrated using phase-insensitive amplifiers focusing on FOPAs and PPLN-based OPAs.

First of all, the use of OPAs for amplification is of particular interest as it allows tuning the amplification band, both in terms of central wavelength and amplification bandwidth, simply by means of the dispersion characteristics of the nonlinear medium and the pumps wavelengths. Parametric amplification with gain as high as 70 dB for single- [15] and 60 dB for dual-pump [16] FOPAs, have been reported. The former result has been achieved by increasing the SBS threshold of 20 dB through phase modulation of the pump with 5 modulation tones. For the latter demonstration, 4 tones sufficed, as a dual-pump scheme requires a 3-dB lower power per pump compared to a single-pump FOPA to achieve similar gain levels.
Furthermore, broadband amplification up to 100 nm of 3-dB amplification bandwidth has been demonstrated for both single- [17] and dual-pump [18] FOPAs. Finally, promising results in terms of in-line amplification have been reported for long-haul transmission showing fairly similar performances when compared with EDFA-based links [80,C19].
The aforementioned results have all been obtained for CW operation. The use of pulsed pumps is a well-known technique to boost the nonlinear interaction with a higher peak power and at the same time suppress SBS spectrally broadening the pumps. However, pulsed-pumping is not well suited for providing amplification in optical communication systems as it requires careful time-alignment of pumps and signals, as well as removes the desirable characteristics of modulation format and bitrate transparency. Nevertheless, it is worth mentioning the impressive result obtained in silicon waveguides where positive parametric off-chip gain has been achieved in the mid-infrared region but under pulsed operation to remove the impact of nonlinear absorption [81].

Even though the potential of opening new communication bands overcoming fiber losses through parametric amplification outside of the typical

EDFA bandwidths would be highly beneficial for increasing the capacity of optical fibers, the importance of OPAs is far from being limited to providing amplification.
Wavelength conversion is indeed an important functionality provided by OPAs, directly related to the ability to provide high gain and broad amplification bandwidth. As discussed in Section 2.3, for high gain regimes, the difference between signal gain and idler CE becomes negligible, enabling CE values as high as 70 dB, not achievable using other wavelength-conversion methods such as semiconductor optical amplifiers (SOAs) [20]. A high output idler power is indeed required in order to have a sufficient idler OSNR for further transmission after wavelength conversion.
Furthermore, the idler wavelength can be easily tuned by adjusting the pumps wavelengths and the scheme is suitable for WDM operation, processing multiple channels at the same time thanks to the broad bandwidth of OPAs. A single-pump FOPA has been used to successfully convert a 1300-nm signal to over 2 μm in a HNLF [82]. Pulsed operation was, however, required to mitigate further SBS and enhance the nonlinear interaction.
Such feature other than being beneficial for networks based on wavelength switching can be employed to provide dispersion [83, 84] and nonlinearity [85, 86] compensation, as discussed in Chapter 4.
Additionally, since FWM does not lead to the generation of only one copy of the signal, the scheme is therefore suitable for providing multicasting. The generation of more than 60 copies of the signal (over a 140-nm window) with low signal degradation has been shown in [87].

Gain saturation is generally an undesirable feature of OPAs as it restricts the maximum output power. The limiting property, however, can be beneficially exploited for providing amplitude regeneration. While operating the OPA in the linear regime directly transfers the input signal power fluctuations due to amplitude noise into output power fluctuations, saturating the amplifier allows decreasing such fluctuations [88]. Amplitude regeneration has been demonstrated for high-speed on-off keying (OOK) signals up to a bitrate of 640 Gbit/s in both HNLFs [22] and PPLN waveguides [89].
Additionally, saturation-based regenerators have the property of preserving the phase of the original signal. Therefore amplitude regeneration can be provided also for phase-modulated signals such as BPSK [90] and QPSK [91].

Parametric amplification with pulsed pumps adds complexity to the system and is therefore avoided for pure amplification. There are, however, applications where the additional gating functionality provided by pulsed pumps can be exploited. That is the case for optical time-division

multiplexed (OTDM)-signal demultiplexing and all-optical sampling. Several techniques can efficiently demultiplex an OTDM signal by dropping one of the tributaries. Some of the most common methods, such as nonlinear optical loop mirrors [92] and Kerr shutters [93], make use of XPM. Alternatively, FWM with pulsed pumps allows to time-gate the generated idler through $A_i \propto A_{P1}A_{P2}$ and operation for bitrates up to 640 Gbit/s has been demonstrated [94].

Similarly, the gating property of pulsed parametric amplification can be employed also to provide all-optical sampling and evaluate high-speed optical signals in real-time, thus overcoming the bandwidth limitations of current electronics. If the pulsed-pump repetition rate is $(B - \Delta f)/M$, where B, Δf and M are the signal bitrate, the scanning rate and the bit-rate reduction factor, respectively, a low speed detector can be used to evaluate the sampled high-speed signal [95]. All-optical sampling based on parametric amplification has been successfully reported for 200-Gbit/s signals using $\chi^{(2)}$ nonlinearities in a KTP crystal [96] and 300-Gbit/s signals through Kerr nonlinearity in a FOPA [21].

2.6 Applications of phase-sensitive amplifiers

The ability to control the gain by tuning the signal phase provided by OPAs in phase-sensitive operation extends even further the applications of parametric amplification for communication systems.

The possibility to amplify only one quadrature of the complex optical field while attenuating the orthogonal one leads to the most interesting capability of providing noiseless amplification. In order to understand this property, it is important to underline that, in an ideal OPA, the main source of noise added to the signal is due to amplification of vacuum fluctuations [97]. When the OPA is operated in phase-insensitive mode and defining the noise figure as the ratio between input and output signal-to-noise ratio (SNR) in the electrical domain, the limit in phase-insensitive amplifiers is 3 dB. However, if the OPA is operated in phase-sensitive mode, the signal experiences a 6-dB higher gain (Section 2.3) while the vacuum fluctuations are still only phase-insensitively amplified leading to an ideal noise figure of 0 dB once both signal and idler are considered as the "input signal". A noise figure of 1.45 ± 0.2 dB was measured for 9 dB of gain at 1 μm in [98]. More interestingly a recent experiment has reported a record noise figure of 1.1 dB using a phase-sensitive FOPA with 26.5-dB gain at telecom wavelengths [19].

Providing low-noise amplification opens up numerous opportunities. First of all, the possibility of extending the maximum transmission distance by decreasing the OSNR degradation and therefore the overall noise figure of an optical link is of great interest [99]. Using PPLN-based OPAs as in-line amplifiers a reach extension of more than 80% has been reported over a pure EDFA-based link for DPSK signals [100]. Such impressive result was, however, achieved in a dual-pump signal-idler degenerate configuration, which is limited to single-channel operation. The use of non-degenerate configurations can enable extending the benefits of phase-sensitive amplification to WDM operation [101,102]. A 3-dB receiver sensitivity improvement over simple EDFA-based amplification has been reported for a dual-channel QPSK signal using a single-pump OPA [103]. The price to pay for such an extension, though, is a decrease in spectral efficiency as signal, idler and pump need all to be transmitted through the link.

Nevertheless, the simultaneous transmission of both signal and idler through the same link allows not only to improve the amplifier noise figure but to further provide compensation for the nonlinear distortion accumulated during the transmission. As signal and idler are phase-conjugated, their coherent superposition in the OPA allows canceling out some of the nonlinear effect and increase the transmission reach [104,105].

Additionally, the same quadrature-selectivity of the gain can be used to provide phase-squeezing. As introduced in Section 2.3, phase-sensitive amplifiers are characterized by an output-to-input phase relation which, for high gain, is a two-level function, thus suitable to provide phase-regeneration for BPSK signals as discussed in Chapter 5. The concept is schematically illustrated in Fig. 2.12 where the phase-squeezing operation clearly shows the reduction in phase noise on the regenerated signal (Fig. 2.12(c)).

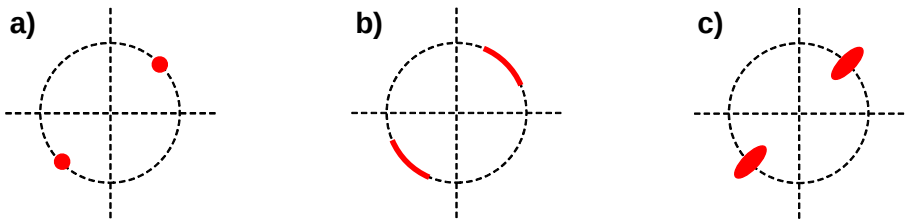

Figure 2.12: BPSK constellation diagrams: (a) ideal signal, (b) signal with phase noise, (c) signal after phase-squeezing regeneration.

All-optical phase regeneration for BPSK signals has been demonstrated using several configurations: single-pump degenerate FOPAs based on interferometers [106], single-pump non-degenerate OPAs with the idler generated through an additional phase-insensitive OPAs [107, 108], dual-pump degenerate OPAs [109] and dual-pump non-degenerate OPAs [110].
The non-degenerate configurations are the most interesting as they may enable WDM [101, 102]. At the moment, however, only simultaneous regeneration of a maximum of two modulated WDM channels has been reported using SOAs [111] and only very recently in an HNLF [112].
If instead of mixing the signal with its phase conjugated copy a different harmonic is chosen, a phase-sensitive OPA can be used to provide M-PSK regeneration. The generalization relies on the mixing between an M-PSK signal and its M-1-th harmonic leading to a staircase output-versus-input phase trend providing analog-to-digital conversion [113].
In particular mixing signal and third harmonic allows regenerating QPSK-modulated signals [114] and even 8-QAM-modulated signals [55], provided that the OPA is operated in the unsaturated regime.
One main drawback of using phase-squeezing for phase-regeneration is the conversion of phase fluctuations into amplitude fluctuations as sketched in Fig. 2.12(c), which follows directly the non-flat gain of Fig. 2.8. In order to minimize the amplitude noise added to the signal after phase regeneration, the OPA can be operated in saturation, enabling simultaneous phase and amplitude regeneration [115]. The scheme can be applied only to purely phase-modulated signals as saturation distorts signals with multiple amplitude levels (Chapter 3).
Alternatively, a more complex OPA configuration where the signal interacts with two different phase harmonics, namely M-1-th and M+1-th, can be used to minimize the PER while preserving the flatness of the step-like phase transfer function [116]. The improvement comes, however, at the price of requiring the mixing between six waves compared to the conventional four. The complexity of the scheme is thus significantly increased and additional FWM stages are required to generate all the phase-locked waves enabling the phase-sensitive interaction.

The applications of the two-level phase transfer function provided by a standard phase-sensitive OPA are not limited to BPSK regeneration. If the signal is modulated in the QPSK modulation format, instead, QPSK-to-BPSK demultiplexing can be achieved. This has been successfully demonstrated using an extended version of a dual-pump degenerate OPA

with a third pump injected at the input stimulating the generation of a BPSK-modulated idler [117]. The phase relation between signal and pumps can then be tuned to demultiplex one optical quadrature at the time.
Additionally, if a fourth pump wave is also present at the input of the nonlinear medium, two BPSK-modulated idlers can be generated. Fine tuning of the phase and power relations between the waves then allows ensuring that each of the two quadratures of the complex optical signal field is demultiplexed into a different idler, thus providing simultaneous access to both BPSK signals [25]. This scheme is investigated in details in Chapter 6.

Finally, optical frequency combs have been attracting a significant interest in recent years for their application not only in metrology and spectroscopy but also in coherent optical communication [118], low-jitter short optical pulses generation and microwave waveforms generation [119]. Several techniques for generating stable and high quality frequency combs are established. While throughout this thesis mainly phase modulation with a high modulation index has been used, resonant structures such as micro-ring resonators as well as supercontinuum generation in HNLFs or mode-locked lasers are more commonly employed as they lead to broader combs. As the comb is usually generated from a single or few seed lines, comb lines generated further away from the main seed suffer from lower power as well as reduced OSNR. The ability to provide low-noise amplification as well as gain shaping makes OPA particularly suitable for amplifying frequency combs [120].

2.7 Summary

This chapter provides a theoretical overview of optical parametric amplifiers (OPAs) starting from a brief summary of the main physical effects affecting an electromagnetic wave at optical frequencies when propagating through a dielectric medium. The focus is mainly directed towards Kerr-nonlinear media such as HNLFs and silicon waveguides as they are the media used in most of the experimental and numerical investigation presented in this thesis. Parametric amplification is, thus, discussed introducing the concept of phase-matching to describe the origin of parametric gain in both phase-insensitive and phase-sensitive operation. The effect of gain saturation is also covered.
Then, several methods to mitigate the impact of SBS in FOPAs are outlined,

highlighting advantages and limitations for each approach.
Finally the state-of-the-art in terms of applications for both phase-insensitive and phase-sensitive optical parametric amplifiers is summarized.

Chapter 3

Parametric amplification of 16-QAM signals

3.1 Introduction

The continuously increasing demand for capacity has resulted in intensive investigations of spectrally efficient multilevel modulation formats [4]. Among those, 16-quadrature amplitude modulation (QAM) is of great interest, as it provides a four-fold increase in the bit rate, for a given symbol rate, combined with the ability to exploit advances in digital coherent receivers [121, 122].
Additional capacity increases may be provided by expanding the current optical communication transmission bands. Optical amplification based on erbium-doped fiber amplifiers (EDFAs) is a well-established and mature technology, which has been employed in optical communication systems for more than three decades. Nevertheless, optical parametric amplifiers (OPAs) may have the potential to compete with EDFAs as they provide several advantages first of all in terms of amplification bandwidth. As discussed in Section 2.5, 100-nm bandwidths and amplification for wavelength regions different from the conventional C- and L- amplification bands of EDFAs have been reported.
However, for future applications, it is critical to understand the limitations of OPAs, especially with respect to amplification of advanced modulation formats.

Along this direction, the use of fiber optical parametric amplifiers (FOPAs) for in-line amplification of wavelength-division multiplexing

(WDM) transmission systems has been extensively investigated in the last years, with promising performances for amplification of long-haul transmissions being reported in [80,C19]. The main challenges to be addressed consist in minimizing the inter-channel crosstalk resulting from the propagation in the highly nonlinear fiber (HNLF) used as amplification medium, as well as implementing polarization-insensitive schemes. The most promising solutions to the latter rely on orthogonally-polarized pumps or on the use of polarization-diversity schemes as is discussed in Chapter 4.

Regarding the interchannel crosstalk, it has been shown in [80, 123] that, as long as the number of channels is limited and the pump power is sufficiently high, the performance degradation caused by crosstalk effects is low. Furthermore, some guidelines enabling low-penalty amplification are given in [24, 124] in terms of the minimum pump-to-signal power ratio.

A high pump-to-signal power ratio is indeed easily achievable by decreasing the input signal power but may not necessarily lead to optimum performance. In fact, three out of four sources of noise in a FOPA, namely amplified quantum noise, Raman photon seeded excess noise, and pump residual noise, are related to amplified spontaneous emission (ASE) and only the fourth one, i.e. pump transferred noise due to pump relative intensity noise (RIN), may worsen the noise figure for increasing signal power levels [125, 126]. While the latter contribution can be kept low using high-quality (low-RIN) lasers for the pumps, the other three are more challenging to address. Generally, as the input power of an amplifier is decreased, the optical signal-to-noise ratio (OSNR) of the output signal is inevitably limited by ASE. This statement may apply to FOPAs as it would to EDFAs. Therefore, from the point of view of OSNR degradation, it would be beneficial to have a high input signal power into the amplifier, provided a suitable high-quality pump is used.

In the same direction, a significantly higher signal input power can lead to saturation effects in FOPAs, which have been proven beneficial for providing amplitude regeneration as they act as amplitude equalizers. Saturation-based amplitude regeneration has been successfully achieved for several one-amplitude-level modulation formats such as on-off keying (OOK) [88, 127], differential phase-shift keying (DPSK) [22, 90], and quadrature phase-shift keying (QPSK) [91].

The effects on multi-level signals such as 16-QAM, however, are less favorable. Since FOPAs rely on the ultra-fast Kerr nonlinearity in HNLFs, the effect of gain saturation results in a symbol-dependent gain, hence in distortions of the 16-QAM constellation as discussed in the following

sections.

Investigations on the use of phase-insensitive parametric amplification for multilevel modulation formats have only been initiated recently. The bit-error ratio (BER) performance of a parametrically-amplified single-channel 16-QAM signal has been theoretically analyzed [128] and experimentally reported within the linear regime of a FOPA [129]. The investigation focused on the importance of a pump with high OSNR and low RIN to provide amplification with low OSNR penalty.

In this chapter, the analysis is extended to include both linear and saturated operation of the FOPA. First the setup used for both numerical and experimental investigations of the saturation effects is introduced in Section 3.2. Then the numerical results are reported in Section 3.3 focusing on the error vector magnitude (EVM) metric to quantify the distortion since, by enabling a segregation between symbols, it provides a better insight than the BER on the physical phenomena causing the signal degradation. A figure of merit (FOM) proposed in [24] to quantify the crosstalk effects for WDM amplification is also employed to derive some practical rules to ensure low signal distortion after amplification. The numerical findings are then compared with experimental results in Section 3.4, confirming the concurrent effects of gain saturation and nonlinear phase rotation highlighted by the simulations. Finally, the key points are summarized in Section 3.5.

3.2 Setup description

A schematic of the investigated system is represented in Fig. 3.1.

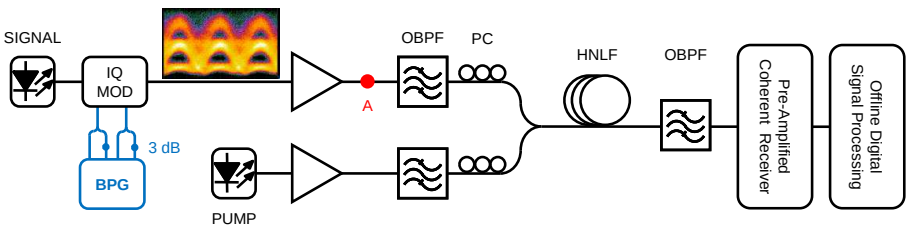

Figure 3.1: Experimental setup for investigating the performances of a FOPA for amplification of 16-QAM signals: the inset shows the optical eye diagram after modulation. Point A marks where the OSNR has been defined before the FOPA for the numerical analysis.

A continuous wave (CW) signal at 1550 nm from a external cavity laser

(ECL) with 100 kHz of linewidth is modulated in the 16-QAM modulation format at 14 Gbaud using a conventional IQ modulator driven by two decorrelated 4-pulse amplitude modulation (PAM) electrical signals. The 4-level signals are generated by combining pseudo-random binary sequences (PRBSs) signals of length $2^{11} - 1$ from a bit pattern generator (BPG).

The signal is amplified to the desired power level using an EDFA and out-of-band ASE is filtered out with an optical band-pass filter (OBPF) (0.8 nm full-width at half-maximum (FWHM) bandwidth) before combining it with a CW pump from another narrow-linewidth ECL at 1557.5 nm amplified to 28 dBm and bandpass filtered with a second 0.8-nm FWHM OBPF.

The polarizations of signal and pump have been aligned by means of polarization controllers (PCs) for maximum four-wave mixing (FWM) efficiency and injected into the HNLF. The HNLF length, attenuation, zero-dispersion wavelength, dispersion slope, and nonlinear coefficient are L =500 m, α =0.7 dB/km, λ_0 =1550.4 nm, S =0.0185 ps/(nm^2·km), and γ =10.7 W^{-1}·km^{-1}, respectively.

At the output of the HNLF, the amplified signal is selected with an OBPF (1-nm FWHM bandwidth) and injected together with a narrow-linewidth local oscillator (LO) in a 90° hybrid whose outputs are connected to a pair of balanced photodiodes (BPDs). Analog-to-digital conversion is then performed followed by offline digital signal processing (DSP).

While for the numerical analysis the coherent receiver has been assumed ideal and the only processing performed has been Viterbi & Viterbi carrier recovery with QPSK partitioning [130], in the experimental investigation the real-time sampling oscilloscope (RTO) (13-GHz bandwidth) providing the analog-to-digital operates at 40 GSamples/s and the offline processing consists of re-sampling, carrier-offset estimation, time-domain equalization using a multi-modulus algorithm and Viterbi & Viterbi carrier recovery.

3.3 Numerical investigation of saturation effects

Numerical simulations have been carried out by solving the nonlinear Schrödinger equation (NLSE) describing the wave propagation in the HNLF by the split-step Fourier method (Appendix A).

The on-off gain spectrum provided by the FOPA has been calculated sweeping the signal wavelength for different signal input power levels in order to investigate the effect of gain saturation. The spectra are shown in Fig 3.2(a) and the decrease in gain in the exponential-gain region (gray area) can be clearly seen when the input power is above -10 dBm. The

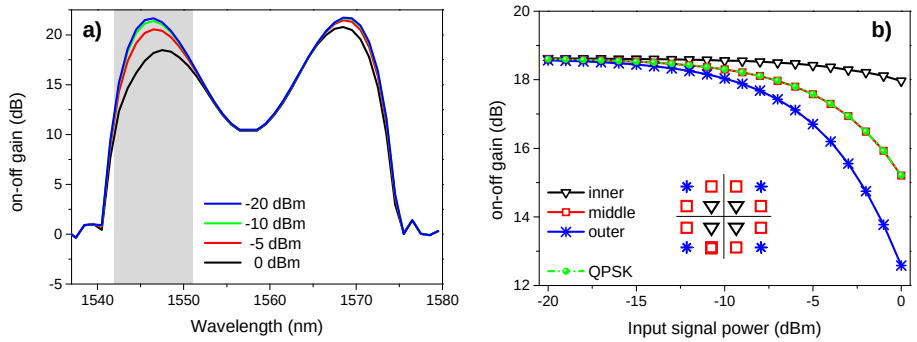

Figure 3.2: (a) on-off gain spectra for different input signal powers showing the on-set of saturation effects for the exponential-gain region (gray area). (b) on-off gain as a function of the input signal power for the different constellation clusters, grouped into inner, middle, and outer, respectively, as shown in the inset. The on-off gain for QPSK constellation clusters is also reported as a reference.

impact of saturation in shaping the gain spectrum is discussed in more details in Section 2.3. The slight asymmetry in the saturated gain spectra is due to third-order dispersion [131].

Furthermore, the gain has also been characterized on a per-cluster basis for a signal centered at 1550 nm, where a "cluster" is defined as the set of received points corresponding to the transmission of the same modulation state among the sixteen possible in the QAM constellation. The results are shown in Fig 3.2(b), where the sixteen curves, one for each cluster, are actually split into three groups depending on the power of the transmitted symbol in the 16-QAM constellation. These groups will be referred to as outer, middle, and inner clusters, according to their power levels, and color coded as shown in the inset of Fig 3.2(b). The curves for clusters belonging to the same group are perfectly overlapping. Note that the middle clusters show the same performance as a QPSK-modulated signal, reported as a reference, since in both cases the power carried by the clusters equals to the average signal power.

The gain investigation on a per-cluster basis allows highlighting the difference between the three groups in terms of input signal power leading to the onset of gain saturation.

The impact of such gain differences on the signal performances has been analyzed using the EVM metric, still on a per-cluster basis. The EVM has been calculated as the root-mean-square error between the received symbol

S_i and the ideal symbol $S_{0,k}$, choosing a data-aided approach in order to evaluate accurately the signal distortion [132].

$$\mathrm{EVM}_k = \sqrt{\frac{\frac{1}{N}\sum_{i=1}^{N}|S_i - S_{0,k}|^2}{\max_l |S_{0,l}|^2}}, \tag{3.1}$$

The EVM has been calculated separately for the sixteen constellation clusters according to Equation (3.1) in order to resolve symbol-dependent effects unlike using an averaged metric such as BER. Furthermore, it has been shown in [133] that nonlinear phase noise can actually lower the BER for high-order QAM signals even though the constellation is distorted. A slight distortion can enlarge the symbol separation, thus decreasing the BER and leading to draw wrong conclusions regarding the actual signal distortion. Prior to the EVM calculation, received and ideal constellations have been normalized in average power and the received constellation has been phase-rotated according to the results of the Viterbi & Viterbi carrier recovery. The use of such algorithm estimates the carrier phase with a $\pi/2$ uncertainty as it relies on removing the phase modulation raising the symbols to the forth power [130]. In order to deal with such uncertainty the set of EVMs has been calculates for all four possible received constellation rotations and the set of lowest EVMs has been considered.

The analysis is first performed on an ideal 16-QAM signal with no noise added (infinite OSNR). The EVM is shown in Fig. 3.3 as a function of the average signal power at the HNLF input for two baud rates: 14 Gbaud and 28 Gbaud. As for the gain saturation, only three curves are shown for outer, middle, and inner clusters, respectively, together with the EVM performance for a QPSK signal.

It can be noticed that the EVM performances are baud-rate independent as expected from the ultra-fast nature of parametric processes. Regardless of the cluster, the EVM increases with increasing input power, however at different rates. The distortion is the strongest for the outer clusters, as expected, since they carry the highest power. However, the second most distorted clusters turn out to be the inner ones. It is essential to remember that, due to the ultra-fast nature of the Kerr nonlinearity, the saturation is caused by the instantaneous power carried by each symbol, and not by the average power. As shown in Fig. 3.2(b), the gain experienced by each symbol can be directly related to its power, thus the outer clusters saturate first and the inner clusters last. In the saturation regime, the outer clusters experience a lower gain. Therefore, they are being shifted towards a lower

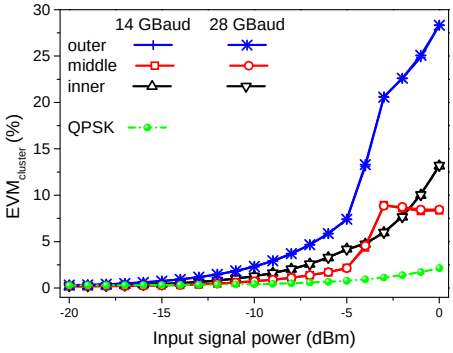

Figure 3.3: EVM as a function of the input signal power for the different constellation clusters, grouped in inner, middle, and outer cluster respectively. A curve for QPSK constellation clusters is also reported as a reference.

power level in the output constellation, compared to an ideal constellation with the same average power. Simultaneously the inner clusters are only slightly affected by the saturation and thus are relatively shifted towards higher power. The combination of these effects, schematically sketched in Fig. 3.4, results in an amplitude squeezing of the constellation as the gain difference between outer and inner clusters reaches almost 6 dB for 0 dBm of input signal power (Fig. 3.2(b)). The EVM for both sets of clusters grows since they are shifted away from their original position in an ideal constellation. The lowest EVM increase is therefore experienced by the clusters the least affected by this power limiting effect, i.e. the middle ones, as their gain curve is in-between outer and inner clusters.

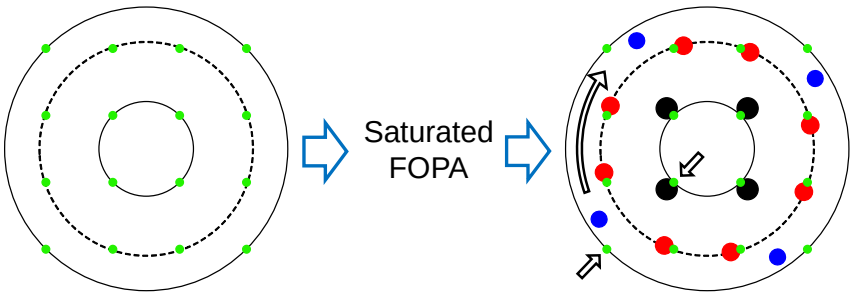

Figure 3.4: Schematic representation of constellation diagrams at the input and output of a saturated FOPA with the arrows highlighting amplitude-squeezing and nonlinear phase rotation effects.

Furthermore, for high input power (around -3 dBm) the EVM trend for the middle clusters reaches a stable value. This can be explained by considering a second power-dependent effect, namely nonlinear phase rotation, which affects the relative position of the clusters. The cluster-dependent power, together with the gain difference, results in a relative nonlinear phase shift between the three power levels. In the specific case of the middle clusters in saturation, even though the spreading and shaping of the cluster points increases with the power, the phase rotation is the dominant contribution to the EVM as it rotates the clusters from their original position. As the rotation does not increase so sharply with the input power though, the EVM gets pinned down to a constant value.

The results of Fig. 3.3 assume an ideal input signal with infinite OSNR and, even though investigating such scenario is interesting to focus on the interplay between gain saturation and nonlinear phase rotation, the nonlinear interaction between signal and ASE noise taking place in the FOPA should also be taken into account. In order to provide a more complete picture taking into account this second major source of signal degradation, the EVM performance is further analyzed injecting a noisy signal in the HNLF. Complex white Gaussian noise is added to the signal at point 'A' in Fig. 3.1, according to the desired OSNR specified over the usual 12.5-GHz bandwidth (0.1 nm).
The out-of-band noise is suppressed with the OBPF before injecting the signal into the FOPA. Fig. 3.5 reports the averaged EVM (EVM_{tot}) as a function of the signal power for various input signal OSNR levels. An averaged metric is considered here as the cluster dependent behavior shows the same features already pointed out in the analysis with no noise added.

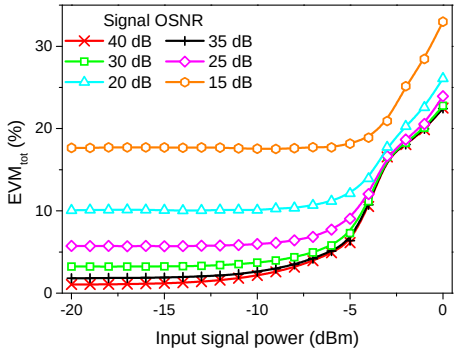

Figure 3.5: Average EVM as a function of the input signal power for different input signal OSNR values before the FOPA (point 'A' in Fig. 3.1).

The lower the OSNR, the higher the amplitude-to-phase noise conversion and thus the higher the EVM can be expected. In the linear regime this is exactly what is observed: the output signal distortion is increased as the OSNR of the input signal decreases. When saturation effects start coming into play, the EVM increases sharply with the input signal power and the gap between the curves decreases. This suggests that the distortion induced by the saturation, i.e. the gain difference combined with the relative nonlinear phase rotation between the clusters, dominates over the noise conversion. In addition, the threshold at which the saturation effects become dominant is moved towards higher power as the OSNR is decreased to further underline the interplay between the two effects.

In [24], the use of a FOM metric based on the power ratio between input pump ($P_p(0)$) and output signal ($P_s(L)$) has been introduced to investigate the effective noise figure of a FOPA taking crosstalk effects into account. Such a metric can also be employed to relate the gain saturation directly to performances degradation for the single-channel scenario investigated here.

Using once again a signal with no noise added at the input to the FOPA, the averaged EVM has been calculated for several input signal power levels. Additionally, the pump power and the fiber nonlinear coefficient have been varied to account for different unsaturated gain levels and saturation conditions, i.e. different input signal power levels leading to gain saturation.

Fig. 3.6(a) reports the EVM as a function of the $P_p(0)/P_s(L)$ ratio, together with the gain decrease, defined as the on-off gain normalized to its unsaturated gain at low input signal power. All the curves lie perfectly superimposed confirming the validity of the chosen FOM to provide an estimate of the FOPA performances.

Setting a threshold for the maximum allowed degradation to an EVM of 5%, corresponding to a BER of around 1×10^{-9} [132], the input pump should be at least 16 dB higher than the output signal (dashed lines in Fig. 3.6(a)).

A ratio above 16 dB directly translates into tolerating a maximum gain decrease of less than 1 dB due to saturation. These results compare well with the more recent experimental results from [124] where the interplay between saturation and crosstalk effects from WDM amplification are investigated and a ratio of 17 dB is suggested for keeping the OSNR penalty below 1 dB.

In order to further test the generality of such results, as for the findings of Fig. 3.3(a), the bit-rate independence has been verified with 28-Gbaud and 56-Gbaud 16-QAM signals showing, as expected, perfectly superimpos-

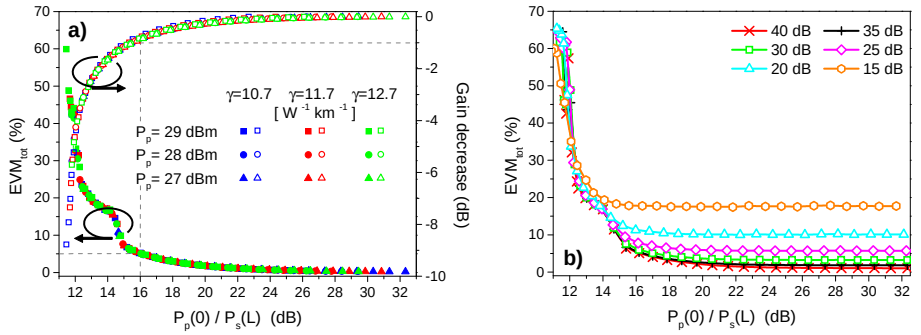

Figure 3.6: (a) Average EVM and saturation-induced gain decrease for an ideal signal with no noise added as a function of the input-pump-to-output-signal power ratio for different pump power and fiber nonlinear coefficients. (b) Average EVM as a function of the $P_p(0)/P_s(L)$ FOM for different input signal OSNR levels defined at point 'A' in Fig. 3.1 (12.5-GHz reference bandwidth).

ing performances.

Finally, the FOM is proven effective also when taking into account noise conversion in the FOPA, i.e. when a noisy signal is injected into the HNLF. A degraded signal OSNR leads just to an upshift of the curve in the linear regime (high FOM values) to account for the initial signal degradation worsened by the amplitude-to-phase noise conversion in the FOPA but does not affect the overall trend that eventually converges to the same sharp increase in EVM with the decrease of pump-to-signal ratio. This can be seen in Fig. 3.6(b) where the trends for different input signal OSNR conditions are shown. As mentioned for the results of Fig. 3.3(b), this behavior confirms the interaction between saturation-induced distortion and noise conversion in the HNLF.

3.4 Experimental verification of numerical findings

In order to verify the numerical findings, the signal distortion is also evaluated experimentally by amplifying a 14-Gbaud 16-QAM signal through a setup fundamentally similar to the one represented in Fig. 3.1 with the only exception of the pump path. In fact, for high-gain FOPAs, stimulated Brillouin scattering (SBS) needs to be addressed (Chapter 2.4). The pump

linewidth is therefore broadened by phase modulation using three radio frequency (RF) tones (94 MHz, 274 MHz, and 970 MHz) [67], shifting the SBS threshold of the HNLF from around 15 dBm to over 28 dBm as shown in Fig 3.7(a).

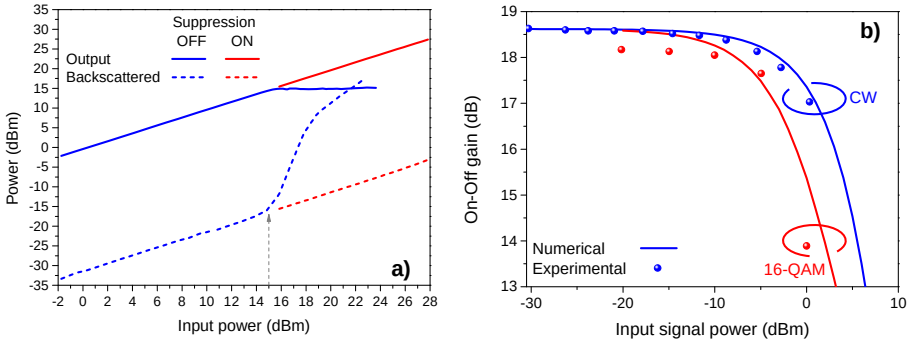

Figure 3.7: (a) Output and backscattered power with and without phase dithering for SBS suppression: dashed arrow marks the power threshold without modulation. (b) on-off gain for CW and 16-QAM signals: comparison between numerical results and experimental measurements.

Remark that the phase modulation of the pump in first approximation does not get transferred to the signal but only to the idler [20, 71]. Therefore, in order to keep the computational requirements low, the SBS suppression had been neglected in the numerical model. Techniques to avoid degradation also of the idler are discussed in Chapter 4.

A comparison between the calculated and measured gain is shown in Fig. 3.7(b) for CW and 16-QAM signals. In both cases good agreement can be seen.

Fig. 3.8(a) reports the normalized constellation diagram at the input of the FOPA while Fig. 3.8(b) and (c) show the output constellations for an input power of -20 dBm and 0 dBm, i.e. when the FOPA is operated in the linear and saturated regime, respectively.

When operating the FOPA in the linear regime no additional distortion can be seen comparing the constellation diagrams at the input and the output. In both cases the clusters are centered around the ideal constellation points. BER performances similar to [124, 129] are thus expected. As the amplifier is operated in saturation, the distortion becomes evident. Superimposing the received constellation at the FOPA output with an ideal 16-QAM constellation, it can be seen that the outer clusters are shifted to

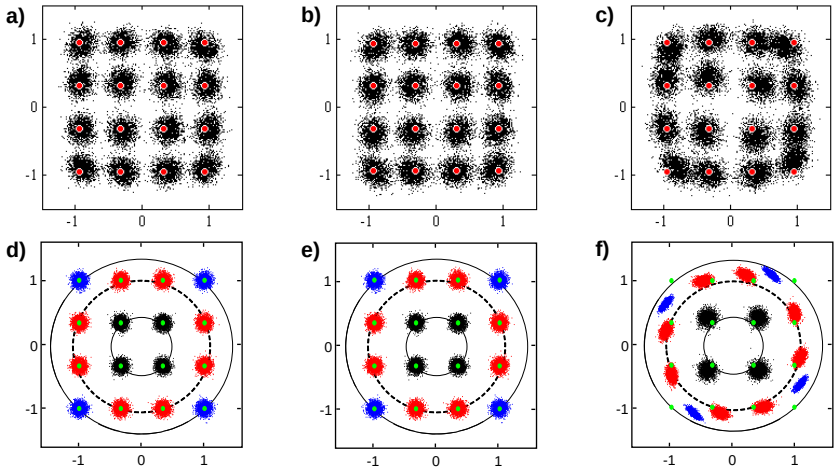

Figure 3.8: Normalized constellation diagrams at the FOPA input (a,d) and output for $P_s(0) = -20$ dBm (b,e) and $P_s(0) = 0$ dBm (c,f): (a-c) experimental and (d-f) numerical (OSNR=25 dB) results. The red/green dots indicate the position of the clusters in an ideal constellation for experimental and numerical results respectively.

lower power while the inner cluster are moved in the opposite direction.

The experimental constellation diagrams (Figs. 3.8(a-c)) are compared with the numerical results (Figs. 3.8(d-f)) and good agreement is shown between the output constellations both in linear and saturation regimes, with the same power squeezing and nonlinear phase rotation characteristics being highlighted for $P_s(0) = 0$ dBm.

3.5 Summary

In this chapter the impact of saturation on the parametric amplification of 16-QAM signals has been analyzed numerically and experimentally. The EVM metric is used to numerically quantify the distortion. The respective role of the main detrimental effects, namely the gain and the nonlinear phase rotation difference experienced by the symbols according to their power level, has been clarified with good agreement between numerical findings and experimental results. Furthermore, the interplay between amplitude-to-phase noise conversion and saturation effects has been numerically highlighted. Finally a FOM proposed in [24] for describing crosstalk effects in a FOPA for WDM operation is shown effective to account

for saturation-induced signal distortion even in a single-channel scenario, providing a rule-of-thumb in terms of the maximum input-pump-to-output-signal power ratio leading to low distortion. Such FOM has also been experimentally investigated for 16-QAM WDM signals in [124] where similar conclusions are drawn.

Chapter 4

Kerr nonlinearity compensation for 16-QAM transmission

4.1 Introduction

To respond to the ever increasing demand for capacity, current optical networks are migrating towards higher bitrates by the use of more complex modulation formats, as introduced in Chapter 3. There, the focus has been directed towards investigating the limitation of fiber optical parametric amplifiers (FOPAs) as subsystems for amplification of 16-quadrature amplitude modulation (QAM) signals.
This chapter instead focuses on one of the critical consequences of transmitting such complex modulation formats, i.e. an increase in the received signal optical signal-to-noise ratio (OSNR) required for error-free detection. In order to accommodate such requirements, higher optical power levels need to be launched into the transmission link. However, nonlinear distortion caused by the Kerr effect in optical fibers sets an upper bound to the total power that can be transmitted before degrading the signal performance [134, 135]. Therefore, being able to compensate for nonlinear distortion would allow increasing the received OSNR without compromising the transmission reach. Along such direction, several techniques have been proposed, initially focusing on designing proper dispersion maps for the link [136, 137]. For deployed links, however, such approaches are unpractical and the interest has been shifted towards solutions that can be applied without significantly modifying the existing

link. Two main categories of solutions are showing great potential, acting either in the electrical or in the optical domain. From one side, algorithms providing digital back-propagation (DBP) are being investigated to invert Kerr effects using digital signal processing (DSP) [138–140]. This approach has the main drawback of scaling poorly with the number of channels due to the high requirements in terms of electrical receiver bandwidth and computational power. Multi-channels applications have been successfully demonstrated performing the compensation on a per-channel basis, i.e. mainly compensating only for self-phase modulation (SPM) [141, 142]. However, SPM is not the main contribution leading to signal degradation [134]. Comparison between single- and multi-channel DBP for wavelength-division multiplexing (WDM) systems indeed highlights the lower improvement achievable when cross-phase modulation (XPM) and four-wave mixing (FWM) are neglected [138, 139, 143–145]. Multi-channel DBP has been experimentally demonstrated but at the expenses of requiring an electrical receiver bandwidth of over 112 GHz, which strongly limits its applications for practical system [140].
Alternatively, the compensation can be achieved all-optically using optical phase conjugation (OPC) to provide mid-span spectral inversion (MSSI) [85, 86, 146, 147]. With the OPC placed in the middle of the link, the spectral inversion allows compensating for the nonlinear distortion accumulated in the first half of the link through propagation in the second half. This approach is, then, the all-optical equivalent of DBP and enables to relax significantly the requirements on the receiver electronics [85, 86, 146–159].
Recently, a hybrid approach making use of a coherent superposition between a signal and its phase-conjugated copy having propagated through the same link has also been proposed [104, 160]. Such a technique has been successfully demonstrated both implementing the superposition in the digital domain, i.e. after detecting both waves [160], as well as using a phase-sensitive FOPA to provide the superposition all-optically [104]. The main drawback in this case is the halving in spectral efficiency as two copies of the same signal need to be transmitted. Furthermore, the coherent superposition in the digital domain suffers from the same WDM-scalability issues as DBP in terms of electrical bandwidth, while the all-optical scheme requires to maintain a stable phase relation between the waves, condition challenging to achieve. An interesting comparing with the two superposition techniques can be found in [161].

In this chapter, nonlinear compensation for 16-QAM signals through OPC is discussed. First, the use of OPC for Kerr nonlinearity compensation

is introduced in more details in Section 4.2. Then, as signal amplification in optical parametric amplifiers (OPAs) automatically provides the generation of a high-quality phase-conjugated copy of the signal (idler), the design of a FOPA-based black-box OPC device is presented in Section 4.3. The key optimization aspects to fulfill the requirements for transparent operation in an optical communication system are highlighted. Section 4.4 reports the device performances. The improvements provided by the FOPA-based OPC in terms of nonlinear compensation have been analyzed for two different system scenarios: a dispersion-managed link, where each span is fully dispersion compensated, and a dispersion-uncompensated link. The experimental setup is described in Section 4.5 and the results for single and WDM cases are provided for dispersion-compensated and uncompensated links in Sections 4.6 and 4.7, respectively. Finally the key points are summarized in Section 4.8.

4.2 Fundamentals of optical phase conjugation for Kerr nonlinearity compensation

The propagation of electromagnetic waves in silica optical fibers has been discussed in Chapter 2. The main effects impacting signal propagation are fiber losses, fiber dispersion, and Kerr nonlinearity, with the latter two strongly impairing the transmission. In the direction of addressing these issues, OPC has been firstly introduced by Yariv *et al.* in 1979 as a promising technique to provide dispersion compensation [83]. However, when some specific conditions are fulfilled, OPC can also be employed to provide simultaneous dispersion and Kerr-nonlinearity compensation as introduced by Pepper *et al.* in 1980 [148].

Since then, the use of OPC has been experiencing an increasing interest with several impressive results being demonstrated [85, 149–151]. Such interest has been further reinforced by the migration of optical networks towards phase modulation formats (differential phase-shift keying (DPSK), quadrature phase-shift keying (QPSK)) which are more strongly affected by nonlinear phase noise [86, 153–155, 158, 159].

Conjugating an optical signal corresponds, in the time domain, to reversing the sign of its chirp and thus temporally inverting the position of the frequency components as sketched in Fig. 4.1.

In order to explain how OPC can be applied to provide Kerr nonlinearity compensation, the starting point is the nonlinear Schrödinger equation (NLSE) (Chapter 2.2) which, taking into account losses, disper-

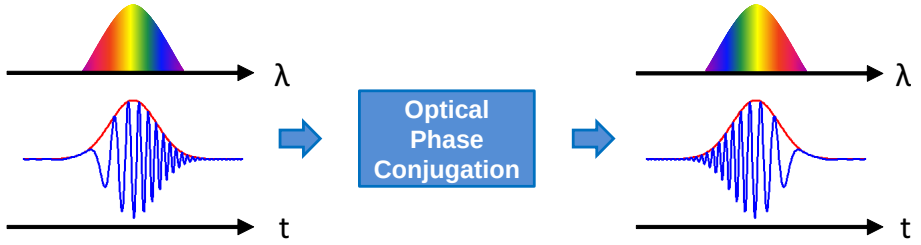

Figure 4.1: Schematic representation of the OPC operation highlighting the temporal inversion of the signal frequency components.

sion up to the third order and Kerr nonlinearity, can be written as:

$$\frac{\partial A}{\partial z} = -i\frac{1}{2}\beta_2\frac{\partial^2 A}{\partial t^2} + \frac{1}{6}\beta_3\frac{\partial^3 A}{\partial t^3} - \frac{\alpha}{2}A + i\gamma|A|^2 A\,. \tag{4.1}$$

Following the approach of [156], the following differential operators can be defined:

$$\begin{aligned}
\hat{D}_2 &= -\frac{1}{2}\beta_2\frac{\partial^2}{\partial t^2}\,,\\
\hat{D}_3 &= \frac{1}{6}\beta_3\frac{\partial^3}{\partial t^3}\,,\\
\hat{D}_{loss} &= -\frac{\alpha}{2}\,,\\
\hat{D}_{NL} &= \gamma|A|^2\,.
\end{aligned}$$

Introducing the operators in Equation (4.1), a more compact version of the equation can be expressed in the form:

$$\frac{\partial A}{\partial z} = (i\hat{D}_2 + \hat{D}_3 + \hat{D}_{loss} + i\hat{D}_{NL})\,A\,. \tag{4.2}$$

The simplest scenario where OPC enables to provide dispersion and nonlinearity compensation is an homogeneous transmission link with the OPC operation placed within the link. The optical signal is spectrally inverted such that the dispersion and nonlinear effects accumulated on the second part of the link cancel out the effects of the propagation in the first part.

For an ideal compensation however, strict requirements are set on the optical link itself as well as on the position of the OPC device. Using the unrealistic approximation that $|A(t)|^2$ is not dependent on z for the sake of a simpler derivation, Equation (4.2) can be solved as in the following [156]:

$$A^*(L_1+L_2,t) = A^*(0,t)e^{i(\hat{D}_2+\hat{D}_{NL})(L_2-L_1)+(\hat{D}_3+\hat{D}_{loss})(L_1+L_2)}\,, \tag{4.3}$$

where L_1 and L_2 are the length of the transmission segment before and after the OPC operation respectively.

Equation (4.3) shows that the conditions for achieving ideal compensation are:

- The length of the two segments should be equal ($L_1 = L_2$) in order to provide chromatic-dispersion compensation, i.e. the OPC operation should be performed in the middle of the link (MSSI). In this derivation, an homogeneous link, i.e. with the same physical properties of the fibers in the two segments, is assumed. In case of different dispersion properties, Equation (4.3) can be generalized obtaining $\beta_2^{(1)} L_2 = \beta_2^{(2)} L_1$, with $\beta_2^{(i)}$ represents the second-order dispersion for segment i. The requirements for providing dispersion compensation is therefore that the overall dispersion accumulated before and after the OPC should be the same, relaxing the need to conjugate the signal exactly in the middle of the link.

- The impact of third-order dispersion should be negligible. The conjugation operation allows inverting the even contribution to the signal phase, therefore only the even-order dispersion terms (β_{2n}) can be compensated for [156].

- Propagation losses should be minimized. The initial approximation of $|A(t)|^2$ being independent on z applies only if the losses are negligible, that is if α is small.

While the first requirement can be easily satisfied, second and third are more challenging to control.

In general the impact of third-order dispersion is minimal, since the effect of second-order dispersion is dominant. However, the most common approach to provide OPC relies on the use of FWM or functionally-equivalent cascaded effects providing the generation of a phase-conjugated copy of the signal at a different wavelength. The scheme therefore leads to a less-than-ideal compensation as the signal propagating before OPC and its conjugated copy after OPC experience different values of dispersion due to β_3.

The most critical condition, however, is the third one concerning the low fiber attenuation required. Several techniques have been investigated in order to converge towards a flat power distribution across the transmission link mimicking a lossless link.

The easiest solution to such a problem would be to significantly decrease the amplifier spacing, therefore minimizing the power excursion.

Even though this approach has been successfully demonstrated [85, 150], its practical application is limited since it would result in a significant and undesirable increase of the number of repeaters along a transmission link.

Alternatively, an effective method to decrease the power variation throughout the link relies on replacing lumped amplification using erbium-doped fiber amplifier (EDFA) with distributed Raman amplifiers [147].

An ideally lossless link is still challenging to realize. However, as shown by Watanabe and Shirasaki in [151], this requirement can be relaxed as long as the ratio between nonlinear effects and dispersion ($\gamma P(z)/\beta_2(z)$) in the transmission segments before and after the OPC operation can be made symmetrical. For practical transmission links with dispersion and power distributions which are symmetrical with respect to the position of the OPC operation, simultaneous dispersion and nonlinearity compensation can be achieved [152].

In the scenario of a link with uniform dispersion and OPC operation performed at the mid-point of the link (MSSI), Raman amplification can be used on the second half of the link to achieve the symmetric power distribution [146].

The MSSI concept can, however, be generalized understanding that the condition on $\gamma P/\beta_2$ simply requires that the nonlinear effects should be experienced by the same temporal shape for both phase-conjugated and original signals. The main contribution to changes in the temporal shape of an optical signal is coming from dispersion, therefore the previous statement translates directly into requiring that the same nonlinear effects are applied to signal and phase-conjugated copy when the two have accumulated opposite amounts of dispersion [156]. This generalization of the MSSI approach is called mid-nonlinearity temporal inversion (MNTI) [156].

The MNTI approach, unlike the more specific case of MSSI, allows efficient compensation when an integral and not local nonlinearity-dispersion symmetry of the link is realized, adding flexibility to the scheme. For example, the use of appropriately designed dispersion maps has been shown to enable the compensation also for links with strongly asymmetrical power distributions as reported in [155].

However, as previously mentioned, for deployed transmission links, changing significantly the dispersion map is rather unpractical. In this direction, two alternatives slightly shifting the position of the OPC by adding an additional shorter fiber span before the OPC device have been proposed [157]. The difference between the two approaches consists on adding either an additional linear propagation region or a nonlinear one. In the

case of linear propagation, a length of dispersion compensating fiber (DCF) is added to compensate for the dispersion of the linear region[1] in the last transmission span.
The nonlinear propagation solution, instead, is based on introducing an extra nonlinear region, i.e. both an additional amplification stage and simple standard single mode fiber (SSMF) with no dispersion compensation. In this case the fiber length should correspond to the nonlinear length of one span. Note that, even though both solutions are interesting to enhance the symmetry of the system for nonlinear compensation, additional dispersion compensation at the receiver is required due to the added fiber length.

All the solutions briefly discussed have been mainly focused on compensating for nonlinear effects in the case of amplitude modulated signals. When phase modulation is considered, the nonlinear phase noise effect, known also as "Gordon-Mollenauer" effect, should also be considered as an additional impairment degrading the signal transmission. Unlike the distortion caused by SPM, XPM, and FWM, nonlinear phase noise is not a deterministic source of degradation but rather a random process [156]. Nonlinear phase noise can, therefore, be only partially compensated even in an ideal system with a constant power distribution, as the noise contributions in the two sections of the link (before and after OPC) cannot be made equal. For practical systems however, the distortion due to nonlinear phase noise requires ultra-long haul (thousands of km) transmission links to become significant and may still be dominated by other Kerr effects such as SPM [156]. Therefore, the transmission links (Sections 4.6 and 4.7) considered to test the effectiveness of the optimized OPC device (Section 4.3) have been chosen following only power and dispersion symmetry arguments, while keeping the scenarios realistically close to deployed links.

Additionally, for WDM systems, the relative frequency deviations between the channels has been highlighted as another source of stochastic variations impairing the effectiveness of compensation for both optical (OPC) and electrical (DBP) techniques. A frequency drift of one of the free-running transmitters with respect to the frequency grid leads to stochastic time-dependent variations of the overall power distribution and, thus, of the nonlinear effects, as discussed in a very recent analysis from Alic *et al.* in [162]. A potential solution suggested could be the use of frequency-locked channels generated from a frequency comb. Due to the novelty of this analysis and the practical issues of not using free-running transmitters,

[1]The term "linear region" refers to the last part of the span, i.e the whole span length minus the nonlinear length where nonlinear effects are dominant.

as well as the fact that still significant improvement can be obtained also for systems based on free-running lasers, this issue is not addressed in this thesis.

The two scenarios investigated in this chapter to test the performances of the optimized OPC device consist of a dispersion-compensated link with lumped EDFA-based amplification (Case A) and a dispersion-uncompensated link using distributed Raman amplification with backward pumping (Case B).

The power-dispersion distribution along the link for Case A is sketched in Fig. 4.2.

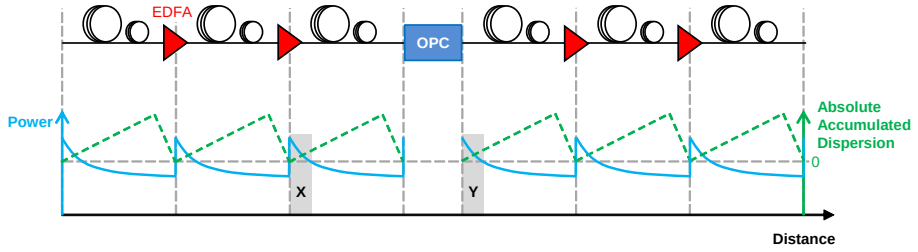

Figure 4.2: (Case A) Power and accumulated dispersion distributions along a fully dispersion-compensated link using EDFA-based lumped amplification.

As each span is fully dispersion compensated (dashed line in Fig. 4.2), the signal accumulates the same amount of dispersion in nonlinear regions before and after the OPC device, thus leading to the same pulse shape in time for signal and conjugated copy. That can be clearly seen, for example, for the nonlinear regions marked with "X" and "Y" respectively. In this case then, the overall segments before and after the OPC operation are not symmetrical in power. However, the condition requiring that the temporally-inverted pulse experiences the same nonlinear effects when it has the same pulse shape (MNTI) is satisfied allowing to achieve nonlinear compensation as shown in Section 4.6.

With the advent of coherent communications and electrical dispersion compensation, current optical networks mainly rely on dispersion-uncompensated links deployed in the field, exploiting the advantage provided by the dispersion-induced walk-off in decreasing nonlinear interaction between signals. Therefore the use of MSSI for a dispersion-uncompensated transmission link is of high interest, especially since the compensation

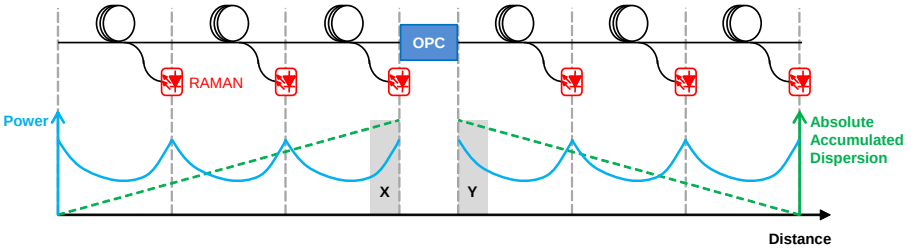

Figure 4.3: (Case B) Power and accumulated dispersion distributions along a fully dispersion-uncompensated link using distributed Raman amplification with backward pumping.

of nonlinear impairments can be combined with dispersion compensation. Fig. 4.3, then, shows the power-dispersion distribution along the link for Case B.

In this scenario, the two segments are characterized by symmetric accumulated dispersion profiles with respect to the OPC device. In order to achieve also power symmetry, the use of backward Raman amplification allows reducing the power excursion along a span in order to mimic a lossless link. Also with this approach then, the nonlinear areas before and after the OPC operation (for example "X" and "Y", respectively) show similar nonlinearities and accumulated dispersion fulfilling the requirement for nonlinear compensation with performances analyzed in Section 4.7. Additionally, unlike in Case A where the dispersion compensation is achieved with a specific dispersion-compensating element, for this link the dispersion compensation is automatically performed by the spectral inversion of the signal in the middle of the link (MSSI).

4.3 Design of an OPC device using a FOPA

For practical application, an OPC device should provide low losses and broadband operation as well as modulation format transparency and polarization independence [156]. Towards this direction, nonlinear compensation was firstly demonstrated for 16-QAM signals in [159] and then in [154]. However, operation was restricted to single polarization and especially in [159] was limited in performances by the penalty introduced by the OPC itself. In [153, 158], polarization-independence was achieved, but only quadrature phase-shift keying (QPSK) operation was reported.

As discussed in Chapter 2.5, FOPAs combine a broad amplification band-

width with a positive conversion efficiency, therefore being suitable candidates as OPC devices. However, stimulated Brillouin scattering (SBS) represents a major limitation to the achievable gain as well as acts as an additional noise source, as discussed in Chapter 2.2. In order to decrease the impact of SBS, the threshold can be increased by broadening the pump linewidth through phase dithering. As discussed in Chapter 2.4, in order to avoid the transfer of phase noise to the idler, a dual-pump FOPA can be used modulating the two pumps such that they are π-shifted in phase. This approach is known as counter-phasing [75] and it has been implemented here by using two channels of an arbitrary waveform generator (AWG) to drive two phase modulators (PMs) one per pump. The use of an AWG allows independent tuning of amplitude and phase for each modulation tone used to broaden the pumps. The amplitudes have been adjusted targeting a modulation index of 1.44 for each tone in order to provide good SBS suppression [67], while the delay has been optimized on a ps-scale such that the π-phase shift is achieved in the highly nonlinear fiber (HNLF), therefore pre-compensating for the dispersion-induced walk-off in the fibers before the HNLF [77].

Starting from these consideration, a dual-pump FOPA using counter-phasing satisfies the first two requirements, namely low losses and broadband operation with potentially low idler degradation.
Another important criterion for practical application is the polarization independent operation. There are mainly two approaches to address this requirement: using orthogonally polarized pumps [158] or implementing a polarization-diversity scheme based on a loop configuration [75, 163].

The use of orthogonally polarized pumps gives the strong advantage of limiting FWM between the pumps, which depletes pump power and causes additional XPM on signal and idler. However, polarization mode dispersion (PMD) in the HNLF may affect the performances disrupting the orthogonality condition. A polarization-diversity loop is more resilient towards PMD, while other issues related to the dual propagation direction arise such as additional noise and FWM contribution from Rayleigh and Brillouin back scattering effects. The back-scattered waves from the co-propagating direction interact with the waves in the counter-propagating direction and vice-versa as discussed in [164]. In this investigation, a polarization-insensitive loop has been chosen as the number of modulating tones as well as the on-off gain have been kept low enough to limit such effects. Furthermore, in order to achieve broadband operation the pumps are positioned 40 nm apart leading to weak FWM interaction between them.

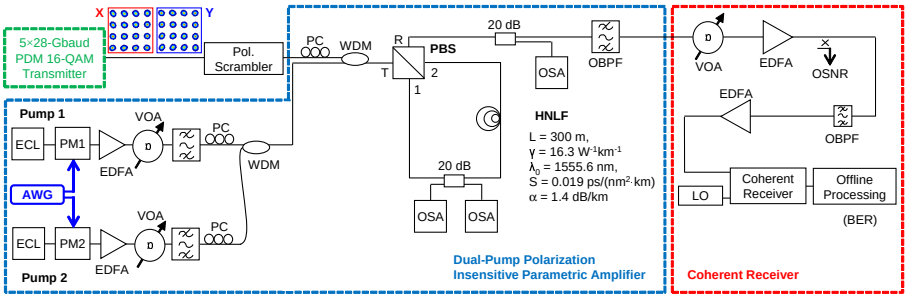

Figure 4.4: Experimental setup for testing the dual-pump polarization-insensitive FOPA to be used as OPC device.

Combining the dual-pump approach with the polarization-diversity loop and applying counter-phasing, the resulting setup is sketched in Fig. 4.4.

The setup consists of a WDM 16-QAM transmitter, the FOPA, and a coherent receiver. Five continuous wave (CW) external cavity lasers (ECLs) on a 50-GHz grid centered at 1550.12 nm are modulated in the 16-QAM modulation format at 28 GBaud. A polarization emulator (Pol-mux) is then used to generate a polarization-division multiplexing (PDM) signal, followed by a decorrelation stage to fully decorrelate all five channels. Before entering the FOPA, a scrambler is used to randomize the state of polarization (SOP) of the signal. More details about the transmitter can be found in Section 4.5.

The FOPA consists of two ECLs serving as CW pump sources at 1534 nm and 1574 nm with linewidths of 25 kHz and 100 kHz, respectively. The pumps are separately modulated using PMs driven in counter-phasing by two sinusoidal tones (69 MHz and 253 MHz; modulation index of 1.44 [67]) generated by a two-channel AWG increasing the SBS threshold whilst minimizing the transfer of pump phase modulation to the generated idlers [75]. The pumps are amplified by EDFAs (output OSNRs of 59 dB and 56 dB for the C- and L-band pumps, respectively) with their power levels controlled via variable optical attenuators (VOAs) thus ensuring constant pumps OSNR values. Out-of-band amplified spontaneous emission (ASE) noise is suppressed by optical band-pass filters (OBPFs) with full-width at half-maximum (FWHM) bandwidths of 0.8 nm before combining the pumps through a WDM coupler.

A second WDM coupler is used to combine pumps and signal before sending them to the diversity loop consisting of a polarization beam splitter (PBS) and a standard HNLF. Fiber length, attenuation, zero dispersion wavelength, dispersion slope, and nonlinear coefficient are

L =300 m, α =1.4 dB/km, λ_0 =1555.6 nm, S =0.019 ps/(nm^2·km), and γ =16.3 W^{-1}·m^{-1}, respectively. The total signal power at the PBS is kept constant at -5 dBm throughout the evaluation except for the gain saturation analysis. In order to match the gain in both loop directions and, thus, demonstrate polarization-insensitive operation, the SOPs of the pumps are tuned via two polarization controllers (PCs) while the signal SOP is randomized by the polarization scrambler. A 20-dB coupler in the loop is used to monitor the pumps power levels in both directions and a PC to ensure that the waves at the output of the HNLF exit at port-R of the PBS. The output spectrum after the diversity loop is monitored by an optical spectrum analyzer (OSA) via a 20-dB coupler. At the FOPA output an OBPF with a 4-nm FWHM bandwidth is used to select either the amplified signal or the idler and to suppress the pumps.

At the receiver, the signal is noise-loaded using a standard pre-amplified receiver where a VOA in front of a noise-loading EDFA allows varying the received OSNR. The channel under test is then selected by an OBPF, amplified to a constant power level, and injected, together with a local oscillator (LO) with a 100-kHz linewidth in the coherent receiver. Finally offline processing is performed, including frequency-offset estimation, adaptive equalization, blind carrier phase estimation, and error counting.

4.4 OPC device performances

As mentioned in Section 4.3, the optimization of the counter-phasing is critical in order to ensure minimal performances degradation by the OPC operation. Each of the two modulating tones has been tuned to achieve the desired (1.44) modulation index for both PMs, with a slight mismatch in amplitude to compensate for small differences in half-wave voltage between PM 1 and PM 2. Afterwards, the delay between the two electrical signals driving the PMs has been adjusted looking at the electrical spectrum of the heterodyne-detected idler at the HNLF output. The idler, generated from a purely CW signal (modulation and Pol-mux stage switched off) has been coherently detected and the electrical spectrum at the real-time sampling oscilloscope (RTO) is shown in Fig. 4.5(a) after fine tuning of delays and amplitudes, i.e. optimum counter-phasing. A suppression of the pump dithering tones above 33 dB could be achieved, in line with what reported in [75].

Furthermore, in order to investigate the impact of a delay mismatch between the two modulations, a third 805-MHz tone has been used and the

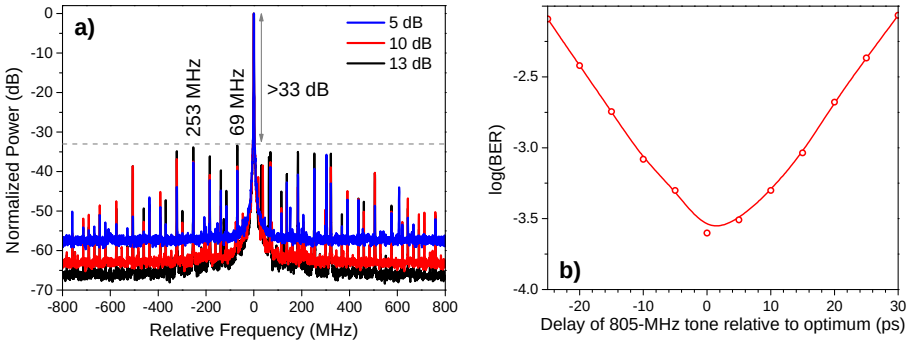

Figure 4.5: (a) CW idler spectra after RTO-acquisition showing suppression of pump phase modulation tones by more than 33 dB. (b) Idler BER (OSNR=26 dB, on-off gain=13 dB) as a function of the counter-phasing time-detuning for a third 805-MHz modulation tone.

relative delay between the 805-MHz sinusoidal signals applied to PM1 and PM2 has been varied between -25 ps and 30 ps with respect to the optimum detuning. The delay optimization has been verified using a single-channel 16-QAM signal at the OPC input and measuring the BER of the generated idler for 26 dB of OSNR with an on-off gain of 13 dB. The BER as a function of the delay relative to the optimum values is shown in Fig. 4.5(b). Clearly the performance degrades rapidly with a sub-optimum counter-phasing. A more detailed analysis of the impact of a sub-optimum delay can be found in [77]. In the analysis that follows, the tone at 805 MHz has been switched off since the SBS suppression achieved with two tones (69 MHz and 253 MHz) was sufficient and the additional pump broadening could have led to additional distortion [164].

Another required property for a black-box OPC device is its broad operation bandwidth as well as polarization-insensitive operation. For the gain bandwidth measurement, the WDM coupler (signal-pumps combiner) is temporarily replaced with a simple coupler. This characterization is performed with the pumps SOPs set for polarization-independent operation and polarization-scrambling of the CW-probe signal, whose wavelength is swept from 1535 nm to 1572 nm. The total pump power into the loop is tuned to 28.2 dBm, 29.9 dBm, and 30.8 dBm for 5 dB, 10 dB, and 13 dB on-off gain, respectively. The results are summarized in Fig. 4.6(a), where a flat gain with a 1-dB bandwidth of 24 nm at 5-dB on-off gain is shown. The bandwidth reduces to 18 nm as the gain is increased to 13 dB. A slight

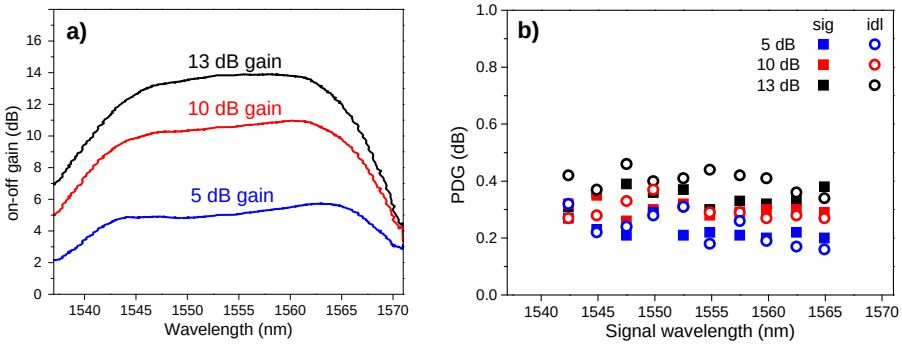

Figure 4.6: (a) on-off gain spectra and (b) PDG as a function of the signal wavelength for amplified signal and idler at different on-off gain levels.

gain tilt resulting from the Raman effect is also visible though its impact is kept low by setting the C-band pump power around 1.8 dB higher than the L-band pump power.

The polarization-insensitive operation is proven by measuring the polarization-dependent gain (PDG), defined as the ratio between maximum and minimum gain as the SOP of a single-channel single-polarization (Pol-mux bypassed) 16-QAM signal at the FOPA input is scrambled. The measurements are performed using the zero-span function of an OSA (∼60 s sweeping time) for both signal and idler. A low scrambling rate is chosen to minimize averaging effects and the results are reported in Fig. 4.6(b). The signal wavelength is varied from 1542.5 nm to 1565 nm, i.e. the flat region of the gain profile (Fig. 4.6(a)) and the PDG measurements are carried out for 5-dB, 10-dB, and 13-dB gain showing only weak fluctuations ranging from 0.2 dB to 0.5 dB with similar signal/idler performances. At higher gain, the pump-power splitting is more critical due to the exponential gain regime, resulting in slightly higher PDG values, nevertheless still below 0.5 dB. Note that the PDG fluctuations for the gain spectra measurements of Fig. 4.6(a) have been averaged out and are therefore not shown.

Another critical property necessary for a practical OPC device is a low (ideally zero) penalty introduced by the conversion. The BER versus received OSNR performances have then been checked keeping the total signal power set to −5 dBm for both single-channel and WDM scenarios. The signal power level has been chosen in order to safely avoid detrimental saturation effects for all the three gain levels considered. In fact, even a low gain saturation results in quite significant distortion of the 16-QAM

constellation, as discussed in Chapter 3.

The BER results for single channel and five channels are shown in Fig. 4.7(a) and (b) respectively. For the WDM case, only the average BER is shown, however the spread between the channels is below 0.2 dB even at high gain, i.e. within the measurement error. For both cases, the performance degrades for increasing on-off gain values. Nevertheless, no difference can be seen between signal and idler performances, further confirming the effectiveness of the counter-phasing in suppressing the transfer of phase noise from pumps to idler.

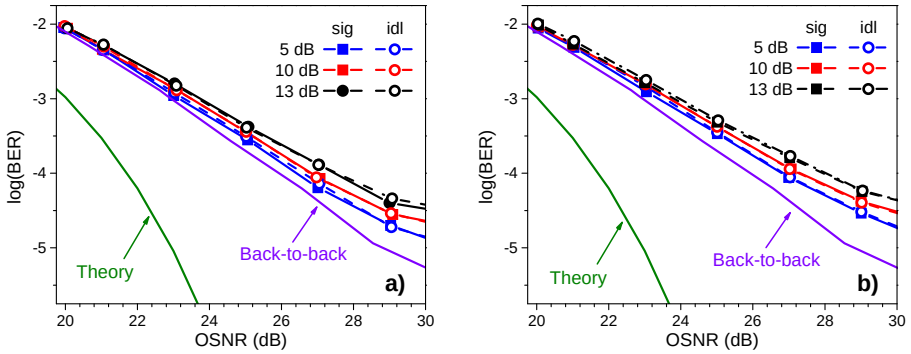

Figure 4.7: BER as a function of the receiver OSNR for amplified signal and idler at different on-off gain levels: (a) single channel and (b) five WDM channels.

Comparing single-channel and WDM scenarios, the degradation due to SPM is worsened by penalty introduced by the WDM operation, mainly attributed to additional interchannel nonlinear effects such as XPM and FWM.

A summary of the measured OSNR penalties for signal and idler in both single-channel and WDM scenarios at a BER of 10^{-4} is given in Fig. 4.8(a) as a function of the selected on-off gain values. In order to keep the distortion experienced in the FOPA low, especially for the WDM case, a limited gain of 5 dB would be more beneficial for practical implementations of an OPC device, leading to an OSNR penalty below 1 dB.

Finally, looking at the input-power operating range, the on-off gain and conversion efficiency (CE) saturation curves are shown in Fig. 4.8(b). This particular characterization is performed in a polarization dependent configuration since the symmetry of the loop configuration ensures similar saturation characteristics for both propagation directions once the pumps

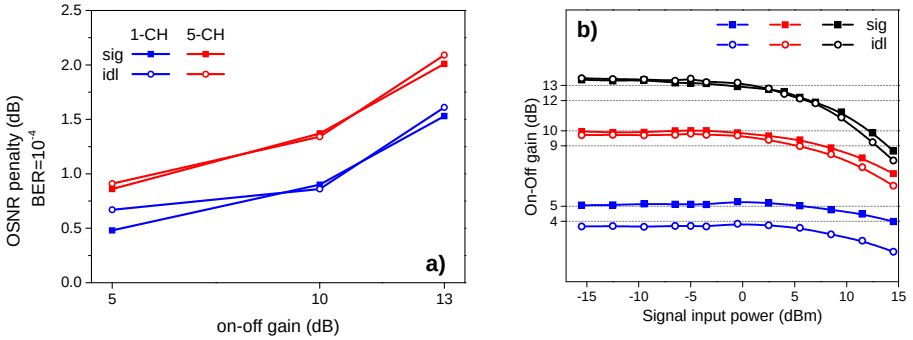

Figure 4.8: (a) OSNR penalty (BER=10^{-4}) for single-channel and WDM scenarios and different on-off gain levels. (b) Gain saturation characteristic as a function of the input signal power: the dashed lines show the 1-dB operation range.

SOPs are properly optimized. The polarizations of the pumps and the signal are aligned to propagate in one direction of the diversity loop without polarization scrambling. As expected, Fig. 4.8(b) shows that the difference between gain and CE decreases with increasing gain. For higher unsaturated gain levels, the gain begins to decrease (saturation) at lower input powers compared to when the unsaturated gain level is lower.

In Chapter 3 it has been shown that low-penalty operation can be obtained once the maximum gain decrease is kept below 1 dB. The power operating range of the device is then defined with respect to the maximum input power leading to a gain variation of 1 dB. An on-off gain of 13 dB allows a range in excess of 20 dB (from -15 dBm to 5 dBm). If the gain is lowered to 5 dB in order to decrease the OPC penalty, the 1-dB operating range is extended up to more than 15 dBm of input signal power, resulting in more than 30 dB of total operating range.

For input power levels below -15 dBm, the OPC device is still expected to introduce low signal distortion. However, such low power values have not been considered since they are of little practical interest and would lead to OSNR degradation due to ASE noise contributions in the FOPA (Section 4.5).

4.5 Experimental setup for Kerr nonlinearity compensation

The performance of the optimized OPC device to provide Kerr nonlinearity compensation is tested in terms of signal-quality improvement after transmission. The experimental setup used is sketched in Fig. 4.9. It consists mainly of the 28-GBaud PDM 16-QAM transmitter, an optical transmission link with the dual-pump polarization-insensitive FOPA used to provide OPC in the middle of the link, and a coherent receiver followed by offline DSP.

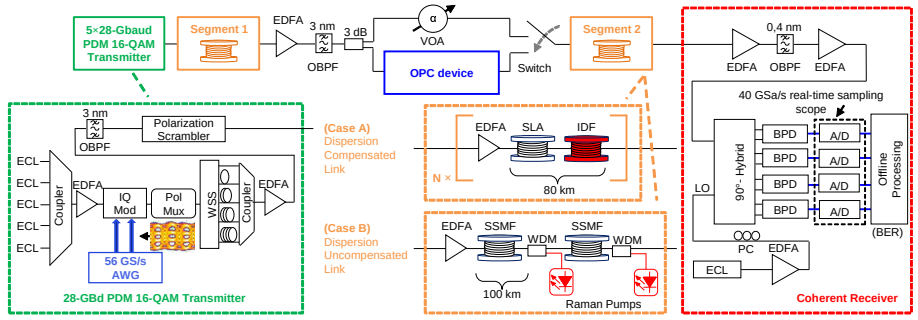

Figure 4.9: Experimental setup for testing the Kerr nonlinearity compensation provided by the OPC operation in the FOPA for two transmission links: (Case A) dispersion-compensated and (Case B) dispersion-uncompensated. Notice that Segment 1 and Segment 2 consist of the same fiber type.

As introduced in Section 4.4, the 5-channel PDM signal is generated by five ECLs on a 50-GHz grid centered at 193.40 THz (1550.12 nm) and modulated in the 16-QAM format at 28 Gbaud using an IQ modulator driven by two-channels of a 56-GSamples/s AWG (13-GHz 3-dB analog bandwidth). The electrical waveforms loaded into the AWG have been linearly pre-distorted to compensate for the non-ideal transfer functions of AWG, electrical cables, and electrical amplifiers. After a split-and-delay PDM emulator (Pol-mux) implementing a delay of more than 500 symbols between the two polarizations, an interleaving stage based on a wavelength selective switch (WSS) fully decorrelates all five channels with a minimum inter-channel delay of 100 symbols in order to mimic a real-world scenario. The full channel decorrelation is paramount in order to correctly evaluate the impact of nonlinearities and nonlinear compensation for WDM systems. As discussed in [159, 165, 166], the conventional odd-even decorrelation scheme fails to reproduce accurately a real situation as the residual

correlation between the next-but-neighbors channels leads to a decrease in the penalty due to inter-symbol interference, but an increase in the impact of nonlinear effects.

The 1.12-Tb/s signal is then amplified by an EDFA, out-of-band ASE noise is filtered out by an OBPF with a 3-nm FWHM bandwidth, and a fast scrambler is used to randomize the SOP, thus demonstrating polarization-insensitive operation.

The scrambled PDM signal is injected into the first N spans of the transmission link (Segment 1). In Section 4.2, the required symmetry of a link with respect to the position of the OPC operation has been discussed, focusing on two specific configurations (Figs. 4.2 and 4.3). These are the two scenarios investigated here: a fully dispersion-compensated transmission link (Case A in Fig. 4.9) and a dispersion-uncompensated link (Case B in Fig. 4.9). In the first scenario, each fully dispersion-compensated span consists of an EDFA and a combination of super-large-effective-area (SLA) fiber followed by inverse dispersion fiber (IDF) for a total span length of 80 km. For the second case, instead, pure SSMF spans are considered with a span length of 100 km. As discussed in Section 4.2, for a dispersion-uncompensated link (Case B), in order to achieve the necessary power-dispersion symmetry before and after the OPC, distributed Raman amplification with backward pumping is used. Such amplification scheme reduces the power excursion across a link, thus obtaining a flatter power distribution [167].

After Segment 1, the signal is amplified by an EDFA followed by a 3-nm wide OBPF to suppress ASE noise, and split into two paths via a 3-dB coupler: one goes through the OPC device, the other bypasses it, corresponding to the straight transmission used as baseline to calculate the improvement provided by the OPC operation. The EDFA has the task to ensure sufficient input power to the FOPA, regardless of the launched power per span, which has been varied to test the tolerance to Kerr nonlinearity. The total signal power into the HNLF providing the OPC operation (see Fig. 4.4) is optimized to around 2 dBm, in order to avoid the saturation induced-distortion in the FOPA, as discussed in Chapter 3, but at the same time maximizing the output power to keep the OSNR degradation low. The optimization carried on for an input signal OSNR of 26 dB is shown in Fig. 4.10(a), clearly showing the trade-off between OSNR and saturation-induced degradation.

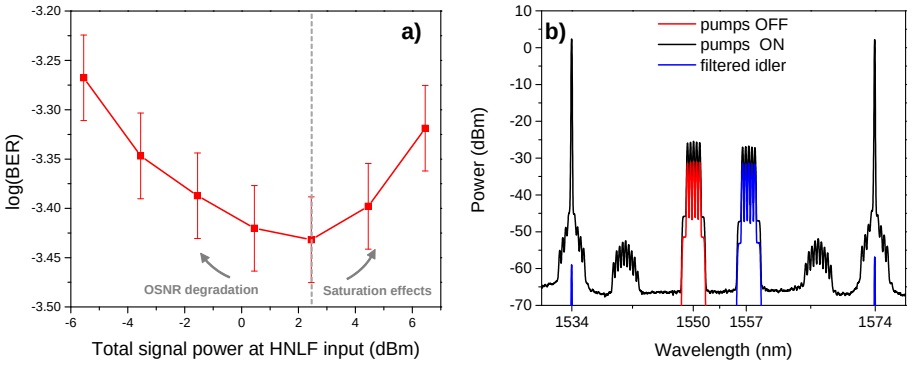

Figure 4.10: (a) Idler BER as a function of the total signal power at the HNLF input: trade-off between saturation effects and OSNR degradation. (b) Optical spectra at output of the polarization-insensitive loop for pump on and off conditions as well as filtered idler at the output of the OPC device.

A total pump power of 28.2 dBm provides an ON-OFF gain of 5 dB as shown in Fig. 4.10(b). This value is chosen to minimize the penalty introduced by the OPC (Section 4.4). At the OPC output the 4 nm-FWHM OBPF provides more than 25 dB of suppression for the pumps (Fig. 4.10(b)).

A switch at the input of the following N spans (Segment 2) allows selecting either the signal directly at the output of Segment 1 ('without OPC') or the idler generated in the FOPA ('with OPC'). Please note that, similarly to [155], a VOA in the path without OPC ensures that the same input power is injected to the first EDFA of Segment 2 in both scenarios, thereby resulting in the same noise accumulation behavior in Segment 2. As the OPC provides low-loss operation, the additional attenuation introduced by the VOA in the 'without OPC'-path is less than 5 dB and mainly due to the relatively high losses (5 dB) of the OBPF used to select the idler at the OPC output. Nevertheless, it has been ensured that no additional OSNR degradation is introduced by the VOA, which would otherwise affect the performance comparison.

The transmission fiber in Segment 2 is of the same kind as the one used for Segment 1, therefore leading to an overall either fully dispersion-compensated or fully dispersion-uncompensated transmission link consisting of $2 \times N$ spans.

At the output of the transmission link the channels are amplified by

the receiver pre-amplifier. The channel under investigation is selected by a narrow-band OBPF (0.4-nm FWHM bandwidth), further amplified and combined with a LO (100-kHz of linewidth) in a 90° optical hybrid. Four balanced photodiodes (BPDs) at the hybrid outputs are connected to four 20-GHz channels of a RTO operating at 40 GSamples/s and providing the analog-to-digital (A/D) conversion. Finally, offline processing is performed including re-sampling, front-end correction, frequency-offset compensation, blind adaptive time-domain equalization using a constant-modulus and multi-modulus algorithm, carrier-phase estimation by blind phase search, de-mapping, and error counting.

In order to investigate the effectiveness of the nonlinearity compensation through OPC, the received Q-factor, derived from the BER has been evaluated by varying the power launched into each span. The results for dispersion-compensated (Case A) and dispersion-uncompensated (Case B) links are discussed in the next sections.

4.6 Results for dispersion-compensated links

Firstly the link consisting of fully dispersion-compensated spans has been considered (Case A) and the performances with and without OPC are reported in this section for both single-channel and WDM transmission.

Fig. 4.11 shows the received constellation diagrams after $N = 3$ and $N = 5$ spans (total length of 480 km and 800 km, respectively) for the optimum launched powers of -4 dBm (without OPC) and -3 dBm (with OPC). The constellations refer to the WDM scenario where the receiver OBPF is tuned on the central channel (CH 3) and both polarizations are shown.

A comparison of the constellations without and with OPC clearly confirms an improvement in the signal quality. Especially after 800-km straight transmission, the constellation diagrams without OPC look distorted with the corner clusters elongated, highlighting the onset of nonlinear distortion. When the signal is phase-conjugated in the middle of the link (with OPC), however, the distortion is decreased and the 16 clusters are more round and better defined.

The full Q-factor curves as a function of launched power with and without OPC for three different transmission lengths corresponding to N = 3, 4, and 5 (480 km, 640 km, and 800 km respectively) are shown in Fig. 4.12.

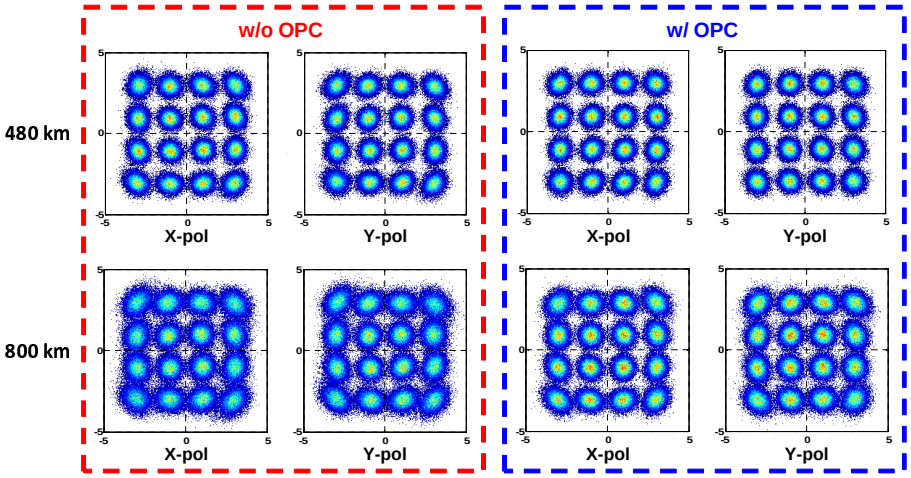

Figure 4.11: Received constellation diagrams (left) without and (right) with OPC for (top) 480 km and (bottom) 800 km dispersion-compensated transmission at the optimum launched powers: -4 dBm without OPC and -3 dBm with OPC. Both X- and Y- signal polarizations are shown.

The Q-factor in dB has been derived directly from the BER as in:

$$\text{Q-factor (dB)} = 20 \log \left(\sqrt{2} \cdot \text{erfc}^{-1} \left(2 \cdot \text{BER} \right) \right). \tag{4.4}$$

To ease the comparison between single channel and WDM cases, the launched power has been defined on a per channel and per polarization basis and for the WDM scenario the received BER has been averaged over the five channels before calculating the Q-factor.

As can be clearly seen in Fig. 4.12, OPC does not reduce the performance of the system in the linear regime for all the transmission lengths considered, meaning that the low penalty introduced by the FOPA is negligible over the OSNR degradation caused by the long-haul transmission.

The improvement provided by the OPC has been defined in terms of difference in the maximum Q-factor values achievable with and without the OPC device. In the single-channel regime (Fig. 4.12(a)), the nonlinearity compensation provided by OPC enables improvements of the Q-factor above 1 dB (480-km transmission) and up to 1.3 dB (800-km transmission) at the expenses of increasing the launched power by 2 dB.

Moving to a WDM scenario (Fig. 4.12(b)), the additional penalty introduced by the OPC device causes a decrease in the improvement. Addition-

ally, the choice of using five free-running lasers may cause a sub-optimum compensation due to relative frequency drifts between the lasers as discussed in [162]. Nevertheless, an increase in Q-factor of 0.56 dB, 0.71 dB, and 0.9 dB, could be achieved for 480 km, 640 km, and 800 km, respectively, provided only 1-dB higher power per channel is launched in the spans.

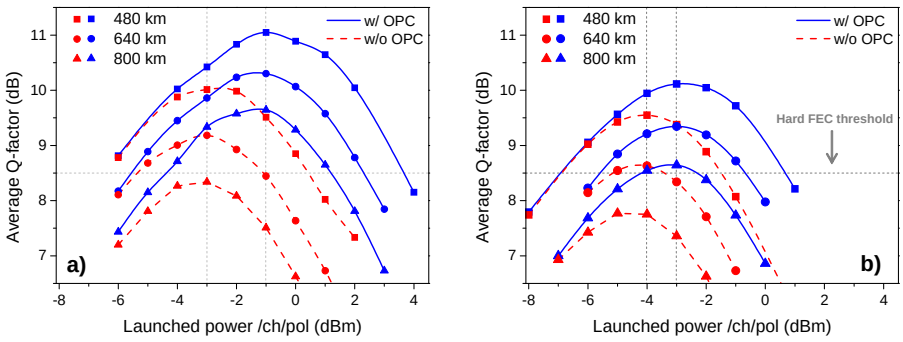

Figure 4.12: Received Q-factor as a function of the launched power per span (per channel, per polarization) for 480-km, 640-km, and 800-km transmission with and without OPC: (a) single channel and (b) 5-WDM channels.

Interestingly, a slight improvement can be seen even when the launched power is equal to its optimum value without OPC (-4 dBm per channel per polarization).
Furthermore, Fig. 4.12 shows that for 800-km transmission without OPC, the degradation is so severe that the hard-decision FEC (HD-FEC) threshold (BER $= 3.8 \times 10^{-3}$, corresponding to Q $= 8.5$ dB) is not reached for either single-channel or WDM transmission. In contrast, employing the OPC in the middle of the link, all the channels show a Q-factor above the HD-FEC threshold, as summarized in Fig. 4.13(a). Note that the wavelength-dependent Q-factor is related to the number of neighbors of each channel, inner channels being more subjected to nonlinear distortion than outer ones. Additionally, the poorer performance of channel 5 with OPC is related to gain-tilting in the in-line EDFAs, yielding a slight OSNR degradation.

For the WDM case, the maximum Q-factor achievable for 800-km transmission with OPC corresponds to the same Q-factor reachable without OPC after 640-km transmission: an increase in the transmission reach by 20% can be obtained with an increase in launched power of only 1 dB. In the single-channel scenario, the reach extension is even larger as the 800-km

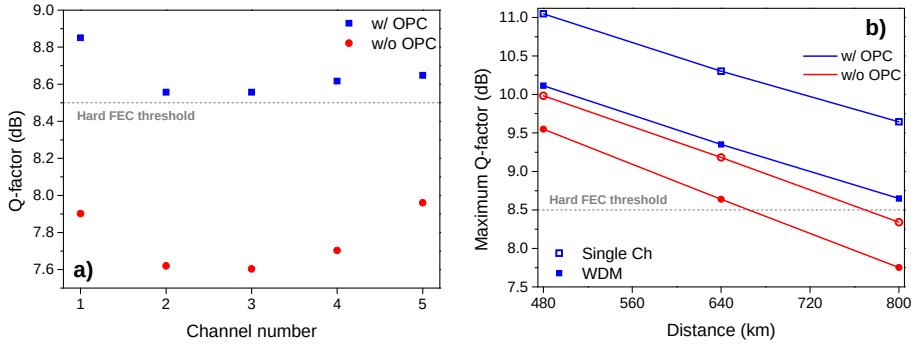

Figure 4.13: (a) Received Q-factor as a function of the channel number after 800-km transmission with and without OPC. (b) Maximum Q-factor as function of the transmission distance with and without OPC for single-channel and WDM transmission.

with-OPC transmission outperforms the 640-km without-OPC transmission by more than 0.5 dB. The increase in launched power required is, however, 2 dB in this case.

Finally Fig. 4.13(b) reports the maximum Q-factor measured as a function of the transmission distance. The comparison of the performances with and without OPC shows that the WDM scenario with the OPC outperforms even the single-channel straight transmission (without OPC).

4.7 Results for dispersion-uncompensated links

In the case of dispersion-uncompensated links, as discussed in Section 4.2, distributed Raman amplification is required to move closer to the required power-dispersion distribution for ideal nonlinear compensation.

The investigated dispersion-uncompensated link makes use of backward-pumped Raman amplification and four spans (corresponding to 400-km transmission). The constellation diagrams with and without OPC for single-channel and WDM transmission at the optimum launched power are shown in Fig. 4.14. The constellation diagrams with nonlinear compensation indeed look cleaner than when no OPC operation is performed. However, for such a short transmission link where nonlinearities are kept low by walk-off effects, the nonlinear distortion is not expected to strongly impair the signal.

The full Q-factor curves as a function of the launched power per span

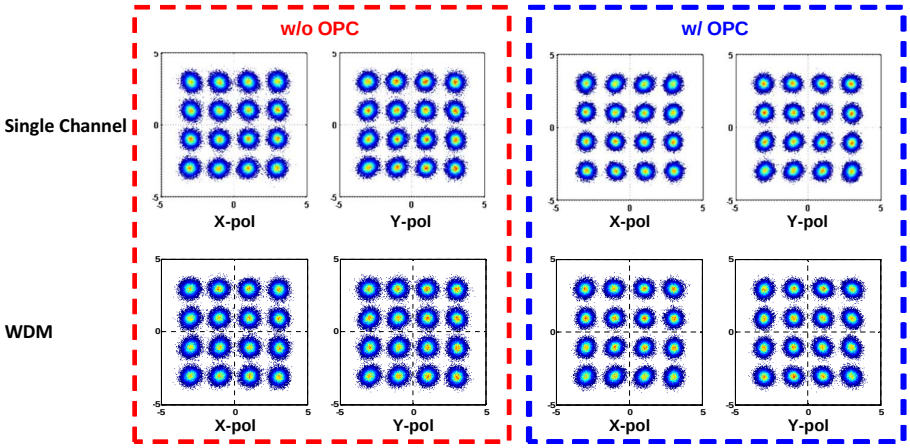

Figure 4.14: Received constellation diagrams (left) without and (right) with OPC for (top) single-channel and (bottom) WDM dispersion-uncompensated transmission at the optimum launched power: -5 dBm without OPC and -2 dBm with OPC. Both X- and Y- signal polarizations are shown.

with and without OPC for single-channel and WDM scenarios are shown in Fig. 4.15(a) and (b) respectively.

Regardless of the short transmission distance, the improvement provided by the OPC device over straight transmission for a single channel is around 1.15 dB (Fig. 4.15(a)) and slightly decreases down to 0.8 dB for the WDM case (Fig. 4.15(b)).

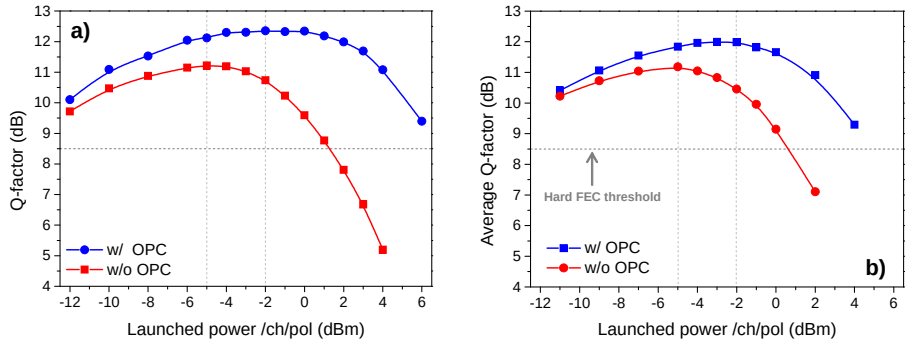

Figure 4.15: Received Q-factor as a function of the launched power per span (per channel, per polarization) for 400-km transmission with and without OPC: (a) single channel and (b) 5-WDM channels.

As a first approximation, the Q-factor scales linearly with the OSNR [168], meaning that a 1.15 dB and 0.8 dB improvements correspond to a reach extension of 30% and 20% respectively. This is a rather conservative estimate since the use of Raman amplification is actually expected to enable an even larger increase in extension reach as discussed in [169, Chapter 12]. Additionally, as seen for the dispersion-compensated link (Fig. 4.12), the signal degradation for longer transmission distances increases and dominates over the penalty introduced by the OPC device, therefore a higher improvement could be expected, potentially allowing an even larger reach extension.

Experimentally it has not been possible to verify the reach extension increasing the transmission distance due to equipment limitations in terms of transmission fiber available.

4.8 Summary

In this chapter, the use of OPC as a promising technique to provide all-optical Kerr nonlinearity compensation is discussed, introducing the conditions on the link under which the compensation can be implemented. Other than the link itself, the requirements for a practical black-box OPC device are used as a starting point to optimize a polarization-independent dual-pump FOPA providing broadband, low losses and low penalty OPC operation. The performances of the OPC device are experimentally demonstrated at 5 dB, 10 dB, and 13 dB on-off gain for 28-GBaud PDM 16-QAM signals in a single- and five-channel system. The maximum polarization dependent gain is reported below 0.5 dB across the 22.5-nm wavelength range (1542.5 nm to 1565 nm) where a flat gain profile is achieved. Signal and idler performance investigations show OSNR penalties at a BER of 1×10^{-4} below 1 dB for both single-channel and WDM cases at 5-dB on-off gain. The scheme is therefore well suited for in-line OPC applications at 5-dB gain for low-loss operation with minimal penalty from the FOPA.

The system performance in terms of Kerr nonlinearity compensation is then investigated using the OPC device to provide MNTI for two link configuration: a fully dispersion-compensated link using lumped EDFA amplification and a fully dispersion-uncompensated link making use of distributed Raman amplification with backward pumping.

Regarding the dispersion-compensated link, the performance has been investigated for 480-km, 640-km, and 800-km transmission. Improvements up to 0.9 dB are reported for WDM transmission, which enables reaching a

BER below the HD-FEC threshold after 800 km, while all the channels after straight transmission have, instead, a BER above such a threshold.

For the dispersion-uncompensated link instead, the available SSMF limited the performances investigation. Nevertheless, an improvement of 0.8 dB is reported for 400-km transmission in a WDM scenario.

All-optical OPC is, thus, a reliable and effective way to provide Kerr nonlinearity compensation and can be applied to several link configurations employing advanced-modulation formats for highly-spectrally efficient communications.

Chapter 5

Phase regeneration in silicon waveguides

5.1 Introduction

The migration of optical systems from amplitude- (on-off keying (OOK)) to phase-modulated signals (differential phase-shift keying (DPSK)) in the last decade has generated a renewed interest in all-optical phase-sensitive signal processing. Several breakthroughs have then being reported very recently, spanning from low noise amplification [19] to DPSK regeneration [23]. The nonlinear media of choice for these results have been mainly highly nonlinear fibers (HNLFs). However, in order to obtain the large nonlinear phase shifts required for practical applications, long interaction lengths are needed due to the relatively low nonlinear coefficients of silica HNLFs. Even though tight spooling of HNLFs has been reported in [170] leading to a significantly smaller footprint, only 8 m have been spooled while practical applications usually require lengths of around hundreds of meters. Furthermore, one of the major practical difficulties with the implementation of phase-sensitive functionalities in silica HNLFs is the mitigation of stimulated Brillouin scattering (SBS), as introduced in Section 2.4. One widely used SBS suppression technique relying on phase dithering of the pumps has been extensively discussed in Chapter 4. For the realization of phase-sensitive functionalities, however, it is critical to preserve the phase coherence between the interacting waves. Phase dithering may disturb such coherence and it is therefore challenging to optimize for phase-sensitive applications as it requires very fine tuning [54].

Alternative nonlinear materials may offer more compact implementa-

tions as well as better SBS immunity. Phase-sensitive amplification has been successfully shown by exploiting second-order nonlinearities in periodically poled lithium niobate (PPLN) waveguides [171–173]. Recently, the first demonstration of phase-sensitive amplification exploiting third-order nonlinearities in a waveguide has been reported using chalcogenide glass [174]. A 10-dB phase-sensitive extinction ratio (PER), i.e. ratio between maximum amplification and de-amplification, could be achieved. However, this was possible only in the pulsed-pump regime in order for the pump average power not to exceed the damage threshold of the waveguide [174].

Silicon is considered as another promising nonlinear material for all-optical signal processing applications thanks to its high nonlinear coefficient and potential for on-chip integration. Additionally, silicon photonics can take advantage of the well-established fabrication know-how from CMOS technology. Nevertheless, as discussed in Section 2.2, at telecommunication wavelengths, two-photon absorption (TPA) strongly restricts the pump power that can be used as it leads to the accumulation of free carriers (FCs), resulting in high loss. Achievable PERs below 1 dB have been recently reported under continuous wave (CW) operation in a standard silicon nanowire [175].

Working in the mid-infra red (IR) region, i.e. for wavelengths above 2.1 μnm, the photon energies are below half of the band gap energy of silicon, thus leading to a significant decrease of TPA and in turn of free carrier absorption (FCA). Thanks to the reduced nonlinear losses, conversion efficiency (CE) values up to -5 dB have been demonstrated around 2 µm using a dispersion engineered waveguide [176]. However, operation in the mid-IR is not compatible with current optical networks where transmission is centered in the low-loss region of optical fibers, i.e. around 1550 nm. Furthermore at around 2.6 µm three photon absorption becomes significant.

Alternatively, the accumulation of FCs and in turn the effects of FCA can be kept small operating in the pulsed regime: a PER of 11 dB was obtained under pulsed operation in a sub-mm silicon slow-light photonic crystal waveguide [177, 178]. Due to carrier lifetimes in silicon of the order of few ns [37], the maximum pulse repetition rate for low-FCA operation is constrained to the MHz regime, unsuitable for telecommunication systems and limiting the practical applications for this solution.

As the maximum repetition rate is dictated by the carrier lifetime, a strong effort has been directed towards decreasing the recombination time. Several approaches have been proposed relying either on modifying the

physical properties of the material, i.e. using amorphous silicon [179, 180], polysilicon [181] or porous silicon [182], or adding additional structures, i.e. a p-i-n [37, 183–185] or a Schottky [186] junction along the waveguide. In amorphous silicon, the well-ordered crystal structure of crystalline silicon is replaced by a random network of atoms with dangling bonds whose density can be decreased through hydrogen passivation. Polysilicon refers to a mixture of amorphous and crystalline silicon, where the grain structure acts as traps and recombination centers for the FCs. Porous silicon, instead, uses the very high surface-area ratio of a nanoporous skeleton in order to decrease the carrier lifetime.

Amorphous silicon has a higher nonlinear coefficient than its crystalline counterpart, leading to a higher figure of merit (FOM) with respect to the ratio between Kerr nonlinearity and TPA [179, 180]. However, practical applications have been mainly demonstrate in pulsed regime [187] and only low CEs have been reported for CW operation further impaired by material degradation over time [188, 189].

A decrease in carrier lifetime by an order of magnitude with respect to crystalline silicon has been demonstrated using polysilicon. However, linear losses are also significantly increased up to 10 dB/cm [181]. A similar trade-off comes also with the use of porous silicon where the lifetime can be decreased at the expense of a strong increase in the FCA cross section of more than two orders of magnitude as well as higher insertion losses and TPA [182, 190].

A more promising approach may consist in implementing a junction along the waveguide, which allows using the strong electrical field generated by an applied reverse voltage bias to sweep the TPA-generated free carriers outside of the waveguide. Consequently, the carrier lifetime is decreased by several orders of magnitude, in turn lowering FCA. The approach has been successfully demonstrated using a reverse-biased p-i-n junction resulting in a decrease in carrier lifetime by more than two orders of magnitude [37] and therefore allowing high-efficiency four-wave mixing (FWM) [183, 191]. Similarly, some preliminary measurements on a metal-semiconductor-metal Schottky junction have also reported a decrease in lifetime by a factor 50 in a photonic crystal waveguide [186].

In this chapter, the use of a p-i-n junction fabricated along the waveguide is shown to provide a sufficient decrease in nonlinear absorption to enable exploiting efficiently nonlinear effects in silicon. First, the waveguide properties and fabrication are introduced in Section 5.2. Then the benefits of a reverse-biased p-i-n junction along the waveguide are experi-

mentally investigated in terms of FWM efficiency and wavelength conversion performances in Section 5.3. Next, the core sections of this chapter present the static characterization of phase-sensitive properties of the waveguides (Section 5.4) and the dynamic performances in terms of providing phase regeneration for 10-Gbaud DPSK signals (Section 5.5). Finally, Section 5.6 summarizes the key results provided in the chapter.

5.2 Waveguide properties and fabrication

Silicon nano-rib waveguides have been fabricated in a BiCMOS foundry at IHP, Frankfurt Oder, Germany, using 248-nm deep UV lithography followed by etching with a silicon-nitride hard mask.

The waveguides have a width of 500 nm, a height of 210 nm, and a slab height of 50 nm. Two doped regions have been introduced at a distance of 600 nm from the waveguide center through implantation of boron and arsenic with concentration of 10^{18} cm^{-3} for the p- and n- regions, respectively. Higher-doped regions (concentration of 10^{20} cm^{-3}) are implanted further away from the waveguide and are contacted by metal layers.

A scanning electron microscope (SEM) image of the waveguide cross-section is shown in Fig. 5.1 (a) highlighting the 100 nm thick silicon oxide buffer layer covered by 90 nm of silicon nitride (Si_3N_4).

The separation between the doped regions is a critical design parameter [185]. Closely packed doped regions decrease the voltage level needed to obtain the high electric field required to effectively decrease the carrier lifetime in the waveguide. However, losses in silicon increase with the doping concentration [192, 193]. It is therefore desirable to avoid a significant overlap between the optical mode and the doped regions that would result in an overall increase of the propagation losses. The distance has then been chosen as a result of such a trade-off, under the constraint of keeping the propagation losses below 1 dB/cm.

The etch depth is a second critical parameter affecting the efficiency of the carrier removal as well as the linear losses and the dispersion properties [185]. A shallow-etched waveguide (slab height around 150 nm) would allow decreasing the linear losses through lowering the overlap of the mode field with the surface roughness. At the same time a higher slab increases the efficiency of the junction enabling to further lower the carrier lifetime. However, the optical confinement decreases causing the optical mode to spread and partially overlap with the doped regions. Additionally, the strong normal dispersion introduced by such waveguide geometry limits

the operation bandwidth of the device. The slab height of 50 nm has, therefore, been chosen as a compromise between losses and efficiency of the nonlinear interaction.

Two designs have actually been fabricated: simple waveguides to be used as references and the more advanced structures with the p-i-n junction added. The measured waveguides are characterized by a length of 1 cm, 2 cm, and 4 cm for both designs. Propagation losses, TPA coefficient, and nonlinear coefficient have been estimated equal to α =1 dB/cm, β_{TPA} =0.5 cm/GW and γ =280 $W^{-1}{\cdot}m^{-1}$, respectively [191].

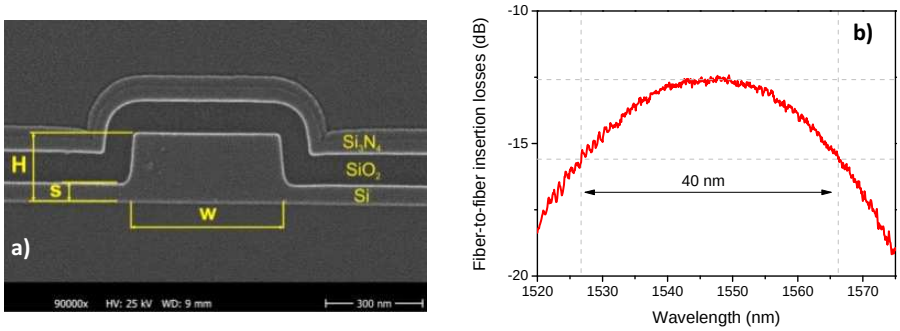

Figure 5.1: (a) SEM picture of the cross-section of a silicon nano-rib waveguide: width W= 500 nm, height H= 210 nm, and slab height s= 50 nm. (b) Fiber-to-fiber insertion losses as a function of the signal wavelength for a 4-cm long waveguide.

The in- and out-coupling is achieved through standard 1D vertical grating couplers with insertion losses of around 4.5 dB/coupler at 1550 nm for TE light coupled at an angle of 9°. The full-width at half-maximum (FWHM) bandwidth of the grating couplers has been measured sweeping the wavelength of a low power CW laser injected into the waveguide and measuring the output power with an optical spectrum analyzer (OSA). The measurements showed a bandwidth of around 40 nm centered in the 1550-nm region with the measured fiber-to-fiber insertion loss as a function of wavelength shown in Fig. 5.1 (b), including the transfer functions of in- and out-coupler. Its value obtained for low power operation is around 12.5 dB in the wavelength region of interest. The use of more optimized grating coupler structures would allow reducing coupling losses to values as low as 0.58 dB per coupler [194] and, thus, significantly decrease the overall insertion losses as well as enabling a higher power into the waveguide. That

would however require more complex fabrication steps and more precise lithography techniques.

In order to investigate the effectiveness of the p-i-n junction in decreasing the carrier lifetime and consequently the nonlinear losses due to FCA, the power levels at the output of two waveguides, one without the junction and the other with the junction reverse-biased with 20 V of direct current (DC) voltage, are compared when the coupled optical power is varied. The results for 4-cm-long waveguides (Fig. 5.2 (a)) show a strong FCA-induced output power saturation when no junction is present, coming up for coupled powers as low as 9.5 dBm. Instead, when a 20-V reverse-biased junction is used, the onset of the output power saturation is shifted up to 22.5 dBm of input power, leading to an output power increase of more than 9 dB. Unless stated otherwise, the DC voltage across the p-i-n junction ('junction voltage') has been estimated by calculating the breakdown voltage of the junction and it is therefore lower than the voltage applied through the DC probes ('contact voltage') [185].

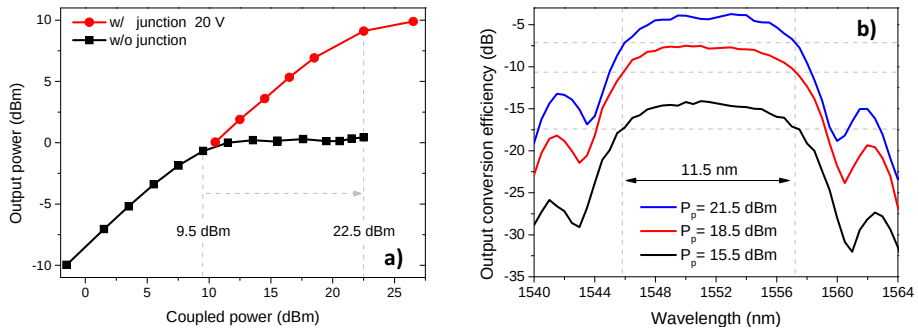

Figure 5.2: (a) Output power versus coupled power for two 4-cm long waveguide, one without junction (black) and one with a 20-V reversed-biased junction (red). (b) Output CE spectra for different coupled pump powers at the input of a 20-V reversed-biased 4-cm long waveguide.

After having verified a strong decrease of nonlinear losses for a single wave propagation, the FWM efficiency has been tested injecting two co-polarized waves into a 4-cm-long waveguide reversed-biased with 20 V. One strong wave at 1552 nm acts as a pump and interacts with a weak (-15 dBm) signal leading to the generation of an idler wave symmetrically located with respect to the pump (Section 2.2). The pump power has been varied between 15.5 dBm, 18.5 dBm, and 21.5 dBm effectively coupled into the waveguide. The output-to-output CE, defined as the ratio between

the idler and the amplified signal powers at the device output, has been measured for signal wavelengths spanning from 1540 nm to 1564 nm and the results are shown in Fig. 5.2 (b). The measured CEs have a FWHM bandwidth of 11.5 nm and a maximum value of −3.7 dB achievable with 21.5 dBm of pump power. Higher pump power coupled into the waveguide has been shown to lead to even higher CEs with values up to -0.7 dB being reported using 26 dBm of pump power [191].
No dispersion optimization was performed when designing these waveguides. Using the dimensions of the waveguide cross-section in a vectorial finite-difference mode solver and refining the calculations through numerical fitting of the CE spectrum, a dispersion value $D \approx -2450$ ps/nm·km at 1552 nm has been estimated. A smaller and positive value would instead be required for obtaining parametric amplification as discussed in Section 2.3. Proper dispersion engineering of the waveguide is expected to result in a wider CE bandwidth. The new design however, needs to take into account the trade-offs in terms of slab height and doped-regions separation as discussed above.

5.3 High efficiency wavelength conversion using a p-i-n junction

The high CE achievable by efficiently removing the FCs from the waveguide region makes the device suitable for wavelength conversion applications with low performance degradation in the conversion. In order to further evaluate the benefits of the reduction in FC effects, a simple wavelength conversion experiment has been performed.

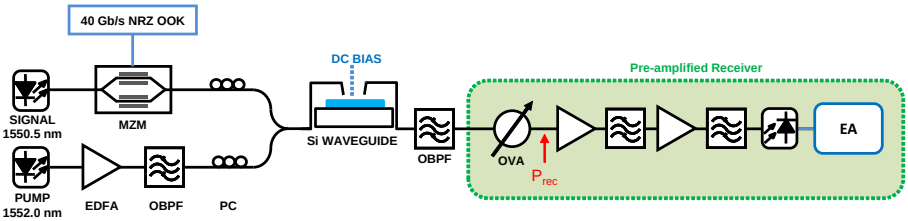

Figure 5.3: Setup for wavelength conversion BER measurements.

The setup is shown in Fig. 5.3. A CW signal at 1550.5 nm is modulated at 40 Gbps in the non-return-to-zero (NRZ) format using a Mach-Zehnder modulator (MZM) driven in push-pull operation by pseudo-random binary

sequences (PRBSs) of length $2^{15} - 1$. The modulated signal is coupled into the waveguide together with a CW pump at 1552 nm, pre-amplified by an erbium-doped fiber amplifier (EDFA) and filtered by an optical band-pass filter (OBPF) with a 0.8-nm FWHM bandwidth to suppress out-of-band amplified spontaneous emission (ASE) noise. The signal and pump powers have been set to 7 dBm and 27 dBm, respectively, before being coupled into a 4-cm long waveguide, resulting in 22.5 dBm of pump power into the waveguide. Due to the polarization sensitivity of the couplers, the signal and pump have been aligned to the TE mode of the waveguide by optimizing the output power. At the output of the device, the wavelength converted signal is selected with a second narrowband OBPF (1-nm FWHM bandwidth) and injected into a conventional pre-amplified receiver for BER measurements. The receiver consists of a variable optical attenuator (VOA) used to tune the received power, followed by two pairs of EDFA and OBPF. The first EDFA acts as noise-loading stage while the second boosts the power to a suitable and constant level for the photodiode (PD), which provides the opto-electronic conversion in front of the error analyzer (EA) stage performing the error-counting. The two OBPFs have a 2-nm and 0.9-nm FWHM bandwidth, respectively.

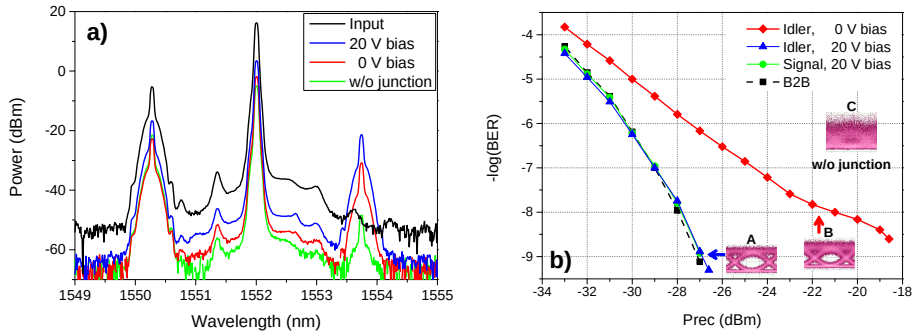

Figure 5.4: (a) Comparison of the input and output spectra for 20-V reverse-biased p-i-n junction, 0-V reverse-biased p-i-n junction and reference waveguide without junction. (b) Measured BER as a function of received power: back-to-back, output signal and idler for 20 V of bias, and idler for 0 V of bias. The insets show the eye diagrams for (A) the idler for 20 V of bias (P_{rec}=-27 dBm), (B) the idler for 0 V of bias (P_{rec}=-18.6 dBm), and (C) the idler for the reference waveguide without junction (P_{rec}=-18.6 dBm).

Fig. 5.4 (a) shows input and output spectra for the three different sce-

narios analyzed: a silicon waveguide with the p-i-n junction and 20 V of reverse bias; the same waveguide but without any bias applied; a reference waveguide of identical length without the p-i-n junction. The output-to-output CEs in the three cases are -4.6 dB, -8 dB, and -26.9 dB respectively. The increase in CE provided by the p-i-n junction with 0 V of bias applied, is due to the built-in field across the junction which still leads to a partial FCs lifetime decrease [184]. The performances of the wavelength converted signal (idler) are then evaluated in terms of its BER performances. The curves are reported in Fig. 5.4 (b). The FCA reduction, obtained when applying the bias, allowed receiving the idler without the need for amplification at the waveguide output before entering the receiver. A negligible power penalty of around 0.2 dB (BER=10^{-9}) is measured compared to the back-to-back case corresponding to the output of the MZM being directly coupled to the receiver. The idler shows clear and open eyes as can be seen in inset A of Fig. 5.4 (b), for a received power P_{rec}=-27 dBm. The same 0.2-dB penalty is also measured for the signal at the waveguide output and may be due to the high total insertion losses of the device.
When the bias is switched off, the idler power decreased by 9.5 dB, resulting in the need for an additional EDFA acting as pre-amplifier before entering the receiver. However, the amplification of such a weak signal lowers the optical signal-to-noise ratio (OSNR) causing a power penalty above 8 dB. Nevertheless, error-free operation and clear eye diagrams are obtained as shown in inset B of Fig. 5.4 (b) for a received power P_{rec}=-18.6 dBm. At last, the reference waveguide without the p-i-n junction is checked. As shown by the closed eye diagram in inset C of Fig. 5.4 (b), measured for a received power P_{rec}=-18.6 dBm, error counting is not possible even after additional amplification at the device output.

5.4 Static characterization of phase-sensitive properties

The overall goal of this chapter is to investigate the potential for phase-sensitive processing in silicon waveguides. As discussed in Section 2.3, the phase-sensitive processing is directly related to the CE, since it is the result of the constructive and destructive interference between signal and idler.

High CE levels are, therefore, promising for obtaining the PER values required for practical applications like phase regeneration (Section 2.6). In order to test the achievable PER performances, a first static characterization, i.e. under CW operation, is performed with focus on the benefits

provided by the p-i-n junction in enabling phase-sensitive processing. Both the impacts of waveguide length and pump power on the measured PER have been investigated.

The setup used for this static characterization is sketched in Fig. 5.5. A CW signal emitted at 1549.76 nm by a narrow linewidth (∼100 kHz) external cavity laser (ECL) is phase modulated with a 40-GHz radio frequency (RF) signal with a modulation index[1] of 4.0 in order to generate an optical frequency comb with 40-GHz line spacing.

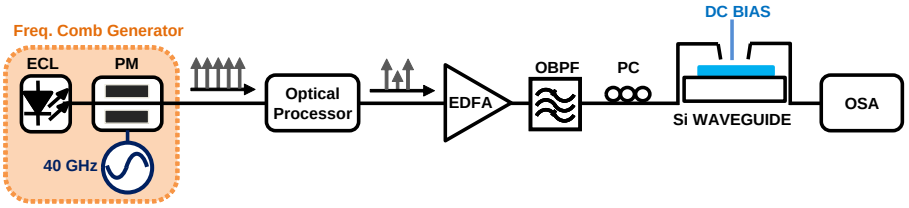

Figure 5.5: Experimental setup for static characterization of the phase-sensitive properties of the silicon waveguide with reverse-biased p-i-n junction.

An optical processor is then used to select three neighboring comb lines: the outer ones act as pumps and the central one serves as signal as shown in Fig. 5.6 (a). The choice of a pump-signal separation of 40 GHz has been dictated by the available frequency comb generator as well as by the ability to sufficiently attenuate the undesired frequency components. Nevertheless, similar performances for larger wavelength spacings are expected thanks to the relatively broadband CE bandwidth (11.5 nm) as in Fig. 5.2 (b).

The pumps power levels are then equalized and the pump-to-signal power ratio set to 30 dB in order to avoid the onset of saturation effects. Pumps and signal are amplified together in an EDFA for a total power of 24 dBm and filtered by an OBPF (0.8-nm FWHM bandwidth) to suppress the out-of-band ASE noise. The three waves are injected into the waveguide through a vertical grating coupler after aligning their states-of-polarization to the TE mode of the device. A reverse-bias voltage of 20 V is applied to the p-i-n junction ('junction voltage') and the signal power at the output of the waveguide is measured using an OSA while the relative phase of the signal with respect to the phases of the pumps is varied using the optical

[1]The modulation index is defined as $\pi/2$-times the ratio of the peak-to-peak voltage of the driving signal to the half-wave voltage of the phase modulator. More details about frequency comb generation can be found in Appendix B.

processor. The optical spectra at the input and output of a reverse-biased 4-cm-long waveguide are reported in Fig. 5.6 (b). The two output spectra have been obtained for a signal phase of 45° and 135° corresponding to maximum amplification (constructive) and de-amplification (destructive interference), respectively. The output signal power difference for the two phase values leads to a PER of 15.5 dB.

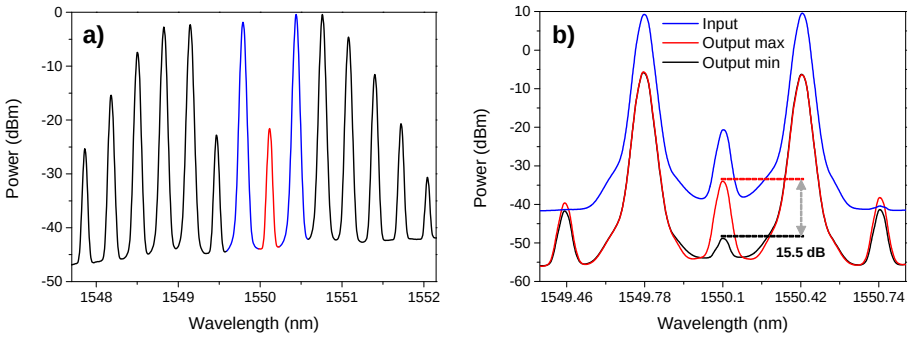

Figure 5.6: (a) Spectrum of the optical frequency comb at the output of the PM with pumps (red) and signal (blue) highlighted. (b) Spectra at the input and output of the 4 cm waveguide for maximum and minimum gain.

The full phase-sensitive gain curves as a function of the input signal phase are reported in Fig. 5.7 (a) for four different waveguides: a 4-cm-long reference waveguide without the junction and three waveguides with 20-V reverse-biased p-i-n junctions and lengths of 1 cm, 2 cm, and 4 cm, respectively. For the reference waveguide, the accumulation of FCs results in 8-dB higher insertion losses compared to the p-i-n junction waveguide of the same length. TPA and strong FCA reduce the efficiency of the parametric mixing, resulting in a nearly-constant phase-sensitive gain with variations below 1 dB, which are close to the measurement errors taking into account drifts of in- and out-coupling.

In contrast, when the waveguides with a p-i-n junction are used, the reverse bias allows decreasing the carrier lifetime, hence removing the main obstacle to efficient nonlinear interaction. The measured gain follows the expected sine square dependence with a 180° phase periodicity (Section 2.3). The measured PER grows from 7.3 dB to 9.7 dB, and 15.5 dB as the waveguide length increases from 1 cm to 2 cm and 4 cm.

The impact of the total power in input to the waveguide is investigated in Fig. 5.7 (b). The output signal power as a function of the input signal phase is reported for total power levels at the waveguide grating spanning

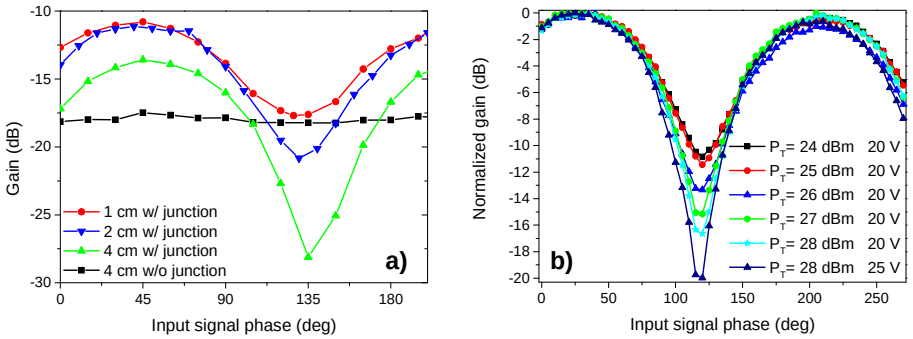

Figure 5.7: (a) Phase-sensitive gain as function of the signal phase for the 1-cm, 2-cm, 4-cm waveguides with the p-i-n junction (20 V of reverse junction voltage) and for the reference 4-cm waveguide without the junction. The total input power is fixed to 24 dBm. (b) Normalized phase-sensitive gain for a 4-cm-long waveguide as a function of the signal phase for various total power levels at the input coupler and an applied reverse-bias of 20 V or 25 V ('contact voltage').

from 24 dBm to 28 dBm and corresponding to effective powers coupled in the waveguide between 16.5 dBm and 20.5 dBm per pump. The stated voltages in this case refer to the voltages applied at the metal contacts of the waveguide through DC probes ('contact voltage'), the actual voltage at the junction ('junction voltage') being therefore lower.

For a constant contact voltage of 20 V, the PER increases with the pump power from 10.8 dB to 16.7 dB. Raising the voltage up to 25 V enables increasing the PER up to 20 dB (for 28 dBm of total power).

As a final remark, it is worth mentioning that the results of Fig. 5.7 (a) and Fig. 5.7 (b) have been measured on waveguides from different wafers, therefore slight variations in terms of coupling and p-i-n junction efficiency are expected. Nevertheless, comparing the two figures, to achieve the same PER of 15 dB, 3-dB higher power is required in the second set of measurements. The difference is mainly attributed to the lower bias voltage used for Fig. 5.7 (b) as the 20-V bias used refers to the voltage applied through the probes ('contact voltage') while the 20 V of Fig. 5.7 (a) have been estimated at the junction and the actual voltage applied is roughly 8 V higher.

The reported values of PER, therefore, confirm silicon as a promising platform for all-optical signal processing once the FC effects are reduced by the use of p-i-n junctions. Successful all-optical signal regeneration has

been demonstrated for PER values as low as 12 dB in HNLFs [195], therefore the values reported here are well above the required levels.

5.5 Phase regeneration of DPSK signals

The PER levels achieved during the static characterization show a strong potential for providing phase regeneration using phase-sensitive amplification in silicon waveguides to enable phase squeezing as discussed in Section 2.6. Fig. 5.8 shows the changes in the static characterization setup of Fig. 5.5 made in order to investigate the scheme under dynamic conditions, i.e. to provide phase regeneration for DPSK-modulated signals.

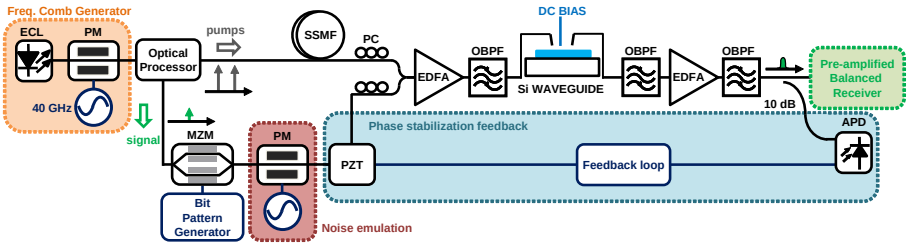

Figure 5.8: Experimental setup for dynamic phase regeneration of a 10-Gbps DPSK signal.

The optical processor after the frequency comb generator is used to separate the signal from the pumps by outputting it to a different port so that it could be modulated in the DPSK format at 10 Gbps using a standard MZM driven in push-pull operation by a PRBS of length $2^{15}-1$. The pumps are propagated through 13.5 m of standard single mode fiber (SSMF) and coupled back together with the signal via a 3-dB coupler. The length of SSMF is chosen in order to approximately match the pumps and signal path lengths (within less than 0.5 m), therefore easing the operation of the phase control loop aiming at compensating for slow thermal drifts and increasing its stability over time. A polarization controller (PC) in each arm is used to align the state of polarization (SOP) of pumps and signal to the TE mode of the waveguide.

After coupling the three waves back together (pump-signal power ratio around 20 dB), they are amplified to a total power of 24 dBm, band-pass filtered and injected into the Si-waveguide. A relatively low input power has been chosen for this proof-of-principle experiment to minimize coupling drifts due to thermal effects in the waveguide. Using a temperature

controlled stage would allow increasing the power and therefore better performances would be expected. As the power is lowered, the contact voltage is increased to 25 V in order to keep the overall insertion losses, including nonlinear losses, around 14 dB. At the waveguide output, a pair of OBPFs with 0.8-nm and 0.3-nm bandwidths, are used to select the signal and input it to the pre-amplified DPSK balanced receiver for BER testing. A second EDFA located between the OBPFs is used to compensate for extra insertion losses. Finally, phase-to-intensity demodulation in the receiver is performed by a 1-bit (100 ps) delay interferometer (DI) followed by a balanced photodiode (BPD) with cut-off frequency of 45 GHz and an electrical low-pass filter (ELPF) with a bandwidth of 7.5 GHz.

The splitting of pumps and signal and their propagation along different fibers inevitably results in a loss of phase coherence due to acoustic and thermal effects, even when balancing the paths lengths. In order to lock the waves in phase, 10% of the signal power is detected by a slow speed avalanche photodiode (APD) (50-MHz 3-dB bandwidth) after the OBPFs at the waveguide output and used as a reference for a feedback loop based on a piezoelectric actuator (PZT). The PZT has a bandwidth of 15 kHz and therefore is able to compensate for the slow thermal drift between the waves. The feedback loop relies on the use of a 1-kHz frequency-dithering tone which allows locking the relative phase for maximum amplification or de-amplification when tracked through a proportional integrator scheme.

In order to investigate the regeneration properties of the scheme, phase noise is emulated deterministically by adding sinusoidal phase modulation to the DPSK signal using a PM driven by a single RF tone generated from an independent unsynchronized RF source. The modulation index and the frequency of the noise tone have been varied to verify the effectiveness of the regenerator under different operation conditions.

Spectra at the input and output of the waveguide are reported in Fig. 5.9 (a) together with eye diagrams in Fig. 5.9 (b) before and after regeneration under two test conditions: when no driving signal is applied to the PM ("w/o noise") and when the phase noise is emulated by a 5-GHz RF signal with a modulation index of 0.89 ("w/ noise").

Clear and open eye diagrams can be seen after the regeneration with only little distortion compared to the back-to-back reference signal with no noise added (top left eye diagram). A significant improvement is instead measured over the back-to-back signal with additional phase noise (bottom left eye diagram).

In order to properly assess the performance of the regenerator, the BER

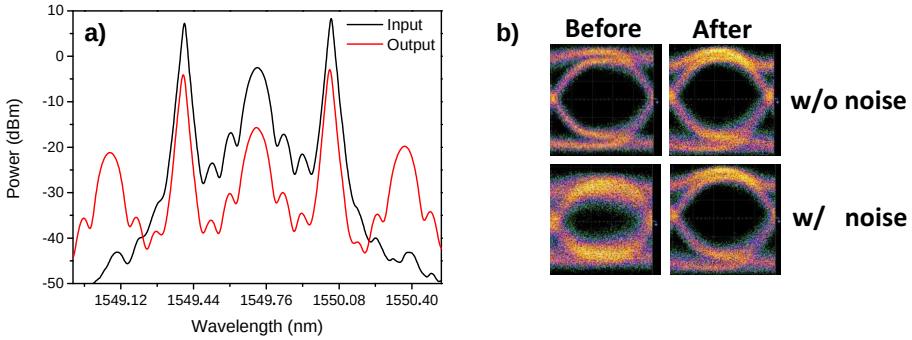

Figure 5.9: (a) Optical spectra at the input and output of the waveguide under dynamic operation with a 10-Gbps DPSK signal. (b) Eye diagrams at the receiver for −36 dBm of received power (left) before and (right) after regeneration, (top) without and (bottom) with phase noise generated by a 5-GHz tone with a modulation index of 0.89.

of the signal before and after regeneration is measured for no degradation as well as phase noise frequencies of 4 GHz, 5 GHz, and 6 GHz. All the measurements have been carried out keeping the modulation index of the phase noise fixed at 0.89. The resulting BER curves as a function of the received power are shown in Fig. 5.10 (a). The performances are evaluated in terms of the receiver sensitivity, defined as the received power required to reach a BER of 10^{-9}.

In the absence of added noise, the scheme results in a power penalty of around 1 dB with respect to the back-to-back reference taken at the PM output. However, when phase noise is added to the signal, the regenerated output shows an improved receiver sensitivity for all the three considered phase noise frequencies, enabling to decrease the power penalty from 10 dB down to less than 3.5 dB. Increased stability both in terms of phase coherence and coupling drifts is expected to allow decreasing the 1-dB implementation penalty further. In particular, a more thorough tuning of the path length difference between the two arms of the interferometer used to separate the signal from the pumps could enable more stable operation.

Furthermore, the penalty introduced by the regenerator even without phase noise may be the result of simple OSNR degradation due to the relatively high insertion losses of the waveguide. As previously discussed, more complex coupling scheme could significantly lower the coupling losses and in turn play an important role in improving the results.

Notice that the difference in performances measured for the various

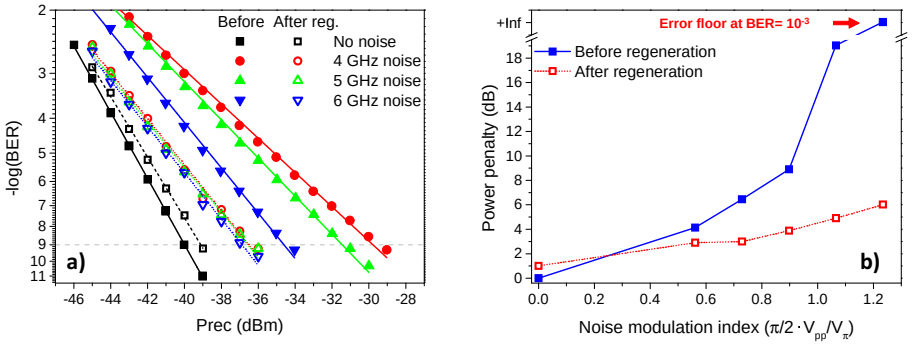

Figure 5.10: (a) BER as a function of the received power for different phase noise loading conditions before (solid symbols) and after (hollow symbols) regeneration. (b) Power penalty (compared to back-to-back for BER=10^{-9}) as a function of the modulation index of the 5-GHz radio frequency tone used to emulate the phase noise.

phase noise emulation frequencies without regeneration are caused by the electrical low-pass filter at the receiver. The roll-off of the filter transfer function partially compensates for the degradation caused by the added phase noise. This compensation is indeed stronger the closer the noise frequency is to the cut-off frequency of the filter, therefore resulting in better BER performances for 6-GHz noise emulation compared to 4 GHz. While this effect can be clearly detected on the BER of the signal before regeneration, no significant correlation can be seen between the performances of the regenerated output and the frequency chosen for the noise emulation. The phase noise suppression provided by the regeneration dominates over the compensation provided by the electrical filtering at the receiver.

The last aspect investigated is the impact of the modulation index on the regeneration performances for a fixed noise frequency (5 GHz). The power penalty at BER= 10^{-9} with respect to back-to-back without degradation is reported in Fig. 5.10 (b) as a function of the modulation index, before and after regeneration.

The results show that an increase of the phase noise modulation index slowly increases the power penalty for the regenerated signal. The degradation, however, grows far steeper on the signal without regeneration, leading to an improvement above 14 dB provided by the regeneration for a modulation index of 1.06. Increasing further the modulation index, up to 1.23, results in an error floor at a BER of 10^{-3} without regeneration. The corre-

sponding regenerated signal can, instead, achieve error-free performances with a penalty below 6 dB.

5.6 Summary

In this section, the use of silicon waveguides for phase-sensitive optical signal processing is investigated. The strong nonlinear loss caused by the accumulation of TPA-induced FCs is the main challenge preventing to effectively use silicon as nonlinear medium for optical signal processing. A reverse-biased p-i-n junction along the waveguide allows decreasing the free carriers lifetime, thus increasing the efficiency of FWM to output-to-output CE values above -5 dB. The results reported here show how the increased CE enables wavelength conversion applications for high-speed signals with low penalty (0.2 dB), as well as the achievement of PER values up to 20 dB satisfying the requirements for phase-sensitive optical signal processing. In this direction, the main result reported is the first demonstration of phase regeneration for DPSK-modulated signal on a silicon platform, showing a decrease in power penalty up to more than 14 dB thanks to the regeneration. Currently two main obstacles limit a further improvement of the performances, namely the relatively high insertion losses of the device as well as the lack of dispersion optimization. Decreasing the device insertion losses as well as proper dispersion engineering leave room for improving such results further and potentially decrease the inherent penalty introduced by the regenerator for a clean signal.

Chapter 6

Multi-pump QPSK-to-2×BPSK wavelength and modulation format conversion

6.1 Introduction

A significant part of the renewed interest in phase-sensitive amplification for all-optical signal processing has been focused on the effort of improving the spectral efficiency through the use of higher order modulation formats such as quadrature phase-shift keying (QPSK) and quadrature amplitude modulation (QAM). In this direction various schemes for phase regeneration have been demonstrated, not only for binary phase-shift keying (BPSK) signals, as mentioned in Chapter 5, but also for the more advanced QPSK [114], 8-QAM signals [55].

Additionally, modulation format conversion is another fundamental functionality for future flexible optical networks. Numerous methods are well-known to provide conversion between amplitude and phase-modulation, especially between on-off keying (OOK) and BPSK [196–198]. The complexity, however, increases significantly when converting between more advanced modulation formats. Furthermore, most of the proposed methods to provide QPSK-to-BPSK conversion end up demultiplexing only one quadrature discarding 50% of the information carried by the original signal [117, 199].

Among demonstrations of all-optical phase-sensitive signal processing targeting advanced modulation formats, R.P. Webb *et al.* have proposed the use of phase-sensitive four-wave mixing (FWM) for converting the two complex quadratures of an optical signal to different wavelengths through phase discrimination. Such a functionality is suitable for QPSK-to-2×BPSK modulation format and wavelength conversion [25]. In contrast with another recently demonstrated phase-sensitive technique relying on orienting the phase-sensitive gain axis to demultiplex the desired quadrature of a QPSK signal [117], this method enables the simultaneous recovery of both BPSK quadratures. Static operation (i.e. using continuous wave (CW) signals) of this scheme has been demonstrated using semiconductor optical amplifiers (SOAs) as nonlinear media [25]. Dynamic operation has then been reported for a 10.65-Gbaud QPSK signal [200], even though the lack of a phase-locking scheme limited the investigations of the performances.

In spite of the numerical prediction of operation of the scheme at symbol rates as high as 40 Gbaud and the demonstration of positive conversion efficiencies with pump spacings of 600 GHz [201], pattern effects due to a relatively slow carrier recovery time need to be addressed when processing high bit rate signals in SOAs [202, 203]. To fully exploit the benefits of all-optical signal processing, bit rate transparent operation is a required condition.

Along such a direction, using other Kerr nonlinear media such as highly nonlinear fibers (HNLFs) or silicon waveguides, as well as $\chi^{(2)}$ materials such as periodically poled lithium niobate (PPLN) waveguides might be more suitable for scaling up the scheme to higher bitrates.
This chapter, therefore, analyzes implementations of the scheme using these media. The concept of phase discrimination is first introduced in Section 6.2, followed by the numerical investigation of an application of the scheme for increasing the phase-noise tolerance of conventional QPSK balanced receivers in Section 6.3. Next, an overview of the block setups used for the experimental characterizations is provided in Section 6.4 and the numerical optimization is fine tuned experimentally with the static characterization reported using the different nonlinear media in Section 6.5. In Section 6.6, the scheme is analyzed dynamically, i.e. for 10-Gbaud QPSK signals. First, the setup used for the dynamic operation is described in details focusing on the challenges of phase stabilization. Then, system performances are investigated using Kerr nonlinearity in a HNLF as well as cascaded second-order nonlinearities in a PPLN waveguide. Finally, Section 6.7 summarizes the key results discussed in the chapter.

6.2 Phase discrimination concept

The phase discrimination scheme relies on the use of four phase-coherent CW pumps (denoted as P1-P4) that are injected together with a phase-coherent signal (denoted as S) into a nonlinear medium, as illustrated in Fig. 6.1(a). Phase-sensitive FWM or functionally equivalent effects enable the generation of two idlers (denoted as I and Q), whose conversion efficiencies with respect to the input signal are determined by the phase relation between signal and pumps.

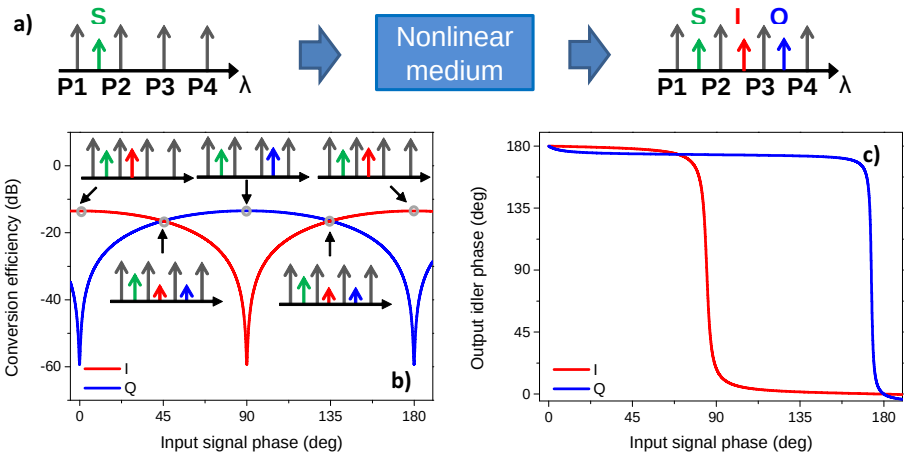

Figure 6.1: (a) Operation principle sketching the waves allocation at the input and output of the nonlinear medium. (b) CEs and (c) output phases for the two idlers (I and Q) as a function of the input signal phase. The curves have been obtained through numerical simulations assuming as nonlinear medium a standard HNLF.

The output-to-input CE is defined as the power ratio between output idler and input signal. By optimizing the pumps phases and power levels together with the signal power, the CEs versus signal phase responses of the two idlers can be arbitrarily phase-shifted. The case of a phase-shift of 90° is of particular interest as it enables the simultaneous conversion of the in-phase and quadrature components of S to I and Q, respectively. This can be seen in Fig. 6.1(b) where the CEs are shown as functions of the input signal phase. Alternatively, this property can be understood by looking at Fig. 6.1(c), where the output idlers phases are plotted as a function of the input signal phase. The 90°-shifted step-like curves indeed enable such a conversion.

CEs and phase transfer functions of Fig. 6.1(b) and (c) have been obtained as the result of a numerical optimization carried out using optimization routines provided by MATLAB® combined with the conventional split-step Fourier method (Appendix A) to solve the nonlinear Schrödinger equation (NLSE) describing the waves propagation in a Kerr medium (Section 2.2). In the specific case, the HNLF is characterized by the parameters listed in Section 6.4. However, as shown throughout the chapter, the scheme can be implemented in any nonlinear medium where processes functionally equivalent to high-efficiency FWM can be obtained.

For practical applications, other than the desired 90° phase-shift, it is critical to provide a high phase-sensitive extinction ratio (PER) as it is directly linked to the flatness of the phase transfer function. As discussed in Section 2.3, a high gain, or equivalently large PER, leads to an output phase $\Phi \approx \arctan(1)$, i.e. a two-states function.

The ability to provide phase discrimination as well as wavelength conversion and phase regeneration makes the scheme suitable for QPSK-to-2×BPSK demultiplexing. A switching node in a network, where the two BPSK converted tributaries are to be routed to different destinations, would indeed benefit from such a functionality. Additionally, the phase-sensitive optical parametric amplifier (OPA) can also be employed as an all-optical pre-processor at a balanced QPSK receiver front-end as discussed in Section 6.3.

6.3 Phase-noise tolerant QPSK balanced receiver

In this section, the phase discrimination scheme introduced in Section 6.2 is used as an all-optical pre-processor in a novel receiver configuration to enhance the phase-noise tolerance of conventional balanced QPSK receivers.

The setup of Fig. 6.2 shows the main blocks of the numerical model implemented to compare the bit-error ratio (BER) of the signal detected by the conventional QPSK balanced receiver shown in Fig. 6.2(a), with the performances obtained using the proposed phase noise reduction scheme of Fig. 6.2(b).

A 10-Gbaud QPSK signal is generated modulating a CW signal with an IQ modulator driven by pseudo-random binary sequences (PRBSs) of length $2^{11} - 1$, and it is noise loaded either with pure phase noise or

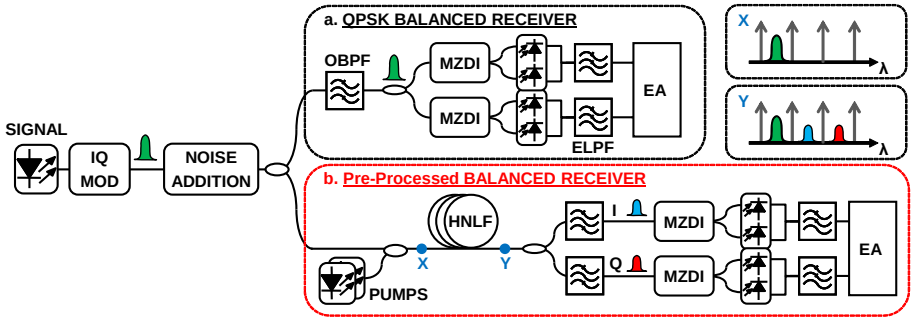

Figure 6.2: System under investigation. The two receivers compared are (a) a standard QPSK balanced receiver and (b) the proposed PSA-based noise reduction scheme followed by two parallel BPSK balanced receivers. Insets: sketched spectra at(X) input and (Y) output of the HNLF.

with complex Gaussian noise before being injected into the two receiver structures.

The QPSK balanced receiver in Fig. 6.2(a) has a standard structure [204]. The signal is filtered by a 2^{nd} order Gaussian optical band-pass filter (OBPF) with a full-width at half-maximum (FWHM) bandwidth of 2.4-times the symbol rate and split into two arms where each of the two quadratures is demodulated. The two arms are identical, consisting of a 1-symbol Mach-Zehnder delay interferometer (MZDI) and a balanced photodiode (BPD) followed by a 5^{th} order Bessel electrical low-pass filter (ELPF) with FWHM bandwidth of 0.7-times the symbol rate. The electrical signals for the two quadratures are then injected into the error analyzer (EA).

The proposed receiver structure, instead, is illustrated in Fig. 6.2(b) and implements the scheme providing the QPSK-to-2×BPSK conversion followed by two parallel interferometric differential phase-shift keying (DPSK) receivers. In the numerical model, the four 0.64-nm spaced pumps are injected into a HNLF together with the QPSK signal following the wavelength allocation depicted in Fig. 6.1(a). The parameters used for simulating the propagation in the HNLF match the physical properties of the fiber used experimentally and are listed in Section 6.4. The power levels of the pumps (short-to-long wavelengths) and signal have been set to 9.7 dBm, 10.6 dBm, 10.1 dBm, 10.5 dBm, and -7 dBm, while the pump phases are 0.0 rad, -

0.3 rad, 2.1 rad, and 0.2 rad. These values lead to the static characteristics of Fig. 6.1(b,c). At the output of the fiber the optical signal is equally split into two arms, for I and Q respectively. In each arm an OBPF selects either I or Q and the rest of the receiver structure is equivalent to the conventional QPSK balanced receiver described above.
As can be seen from Fig. 6.1(b), the maximum CE is relatively low. Higher pumps power levels would allow increasing this value. However, for consistency with the experiments, the power per pump is kept below the stimulated Brillouin scattering (SBS) threshold of the HNLF used (15 dBm as in Fig. 3.7). In the numerical model, a stable phase relation between the waves is implicitly assumed. For a practical implementation, various methods could be employed to guarantee the phase coherence between signal and pumps. Frequency comb generation followed by a phase recovery scheme has been successfully implemented in [114]. Alternatively, additional FWM stages could create the needed phase coherence [23].

Two different scenarios have been considered to benchmark the performances of the two schemes along with a simple DPSK receiver: pure phase noise and complex additive Gaussian noise.
In the first case, a phase modulator (PM) has been used to introduce Gaussian distributed phase noise with a 20-GHz bandwidth ('noise addition' in Fig. 6.2). Phase variance values in the range 0-20° have been considered and the quality of the signal has been evaluated for each variance level in terms of the BER versus the optical signal-to-noise ratio (OSNR) at the input of the OBPFs. The OSNR, defined over a 0.1 nm noise bandwidth, has been varied adding complex Gaussian noise. Monte Carlo simulations have been performed using the split-step Fourier method to solve the propagation through the HNLF. A minimum of 200 errors have been counted to obtain a confidence level above 99%.
The receiver sensitivity, defined as the OSNR required for a BER of 10^{-3}, is the metric used for the comparison. The results are reported in Fig. 6.3(a) as a function of the input phase variance. Both QPSK quadratures (I and Q) received through the pre-processed balanced receiver show an improvement in OSNR sensitivity above 4 dB over the standard QPSK receiver, for the whole phase variance range considered. Furthermore for phase variances above 13°, a BER of 10^{-3} can still be achieved using the pre-processor, unlike with the conventional receiver. The phase squeezing at the BPSK receivers front-end indeed allows reducing the impact of the phase noise in the MZDI-based demodulation. The sensitivity of I and Q is also compared with the performances of a DPSK signal at the same baudrate and received

through a balanced DPSK receiver. A gap increasing with the phase variance can be seen. The main limitation of the pre-processor comes from the phase-to-amplitude noise conversion as discussed in Section 2.3. Decreasing the PER could lower the introduction of amplitude noise, however, that would result in a less flat phase transfer function (see Section 2.3), therefore undermining the phase squeezing. A trade-off between the phase flatness and the phase-to-amplitude noise conversion is desirable.

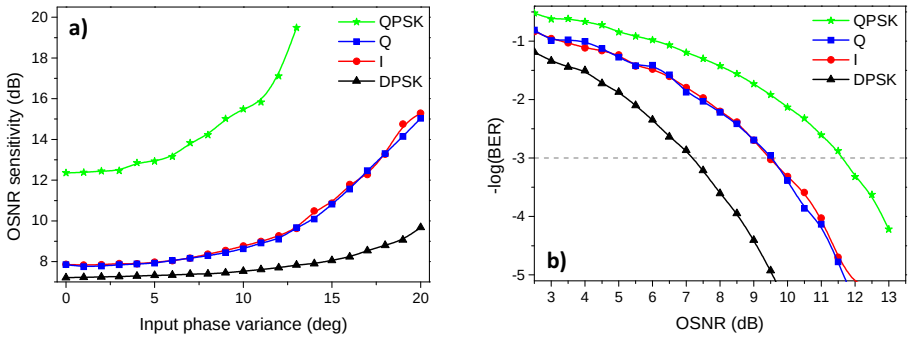

Figure 6.3: (a) Receiver sensitivity (BER of 10^{-3}) versus input phase variance and (b) BER versus OSNR at the IQ modulator output: (green) QPSK balanced receiver, (blue) I and (red) Q idlers using the phase noise reduction scheme, DPSK balanced receiver for a DPSK signal at the same baudrate (black).

Defining the OSNR after the pre-processor neglects the signal-noise interaction in the HNLF. A second set of simulations has thus been run bypassing the PM and defining the OSNR directly at the IQ modulator output by adding complex Gaussian noise. For this scenario the receiver sensitivity is improved in excess of 2 dB as reported in Fig. 6.3(b). The lower improvement can be explained remembering the amplitude-to-phase noise conversion due to self-phase modulation (SPM) in the HNLF.

Recently a multi-harmonic scheme for QPSK signal regeneration has been proposed and demonstrated numerically [205] and experimentally [116]. The novelty of the method relies on making use of additional harmonics to provide the desired step-like phase-transfer function while reducing the detrimental phase-dependent gain variations leading to phase-to-amplitude noise conversion. Potentially, a similar approach could be applied improving the effectiveness of the all-optical pre-processor. However this can be achieved at the expenses of increasing even further the

complexity with the requirement of additional pumps and a consequently more challenging optimization.

6.4 Operation principle and nonlinear media

The numerical simulations showed promising levels of improvement provided by the scheme. However, the critical challenge of avoiding phase drifts between pumps and signal has been neglected in the numerical model. In order to verify efficiency and performances of the scheme under more realistic conditions, an experimental characterization has been performed. The setup considered is sketched in Fig. 6.4.
The four pumps and the signal are generated from a single CW laser source by frequency comb generation such that a stable phase relation between the five waves involved in the phase-sensitive process is guaranteed.

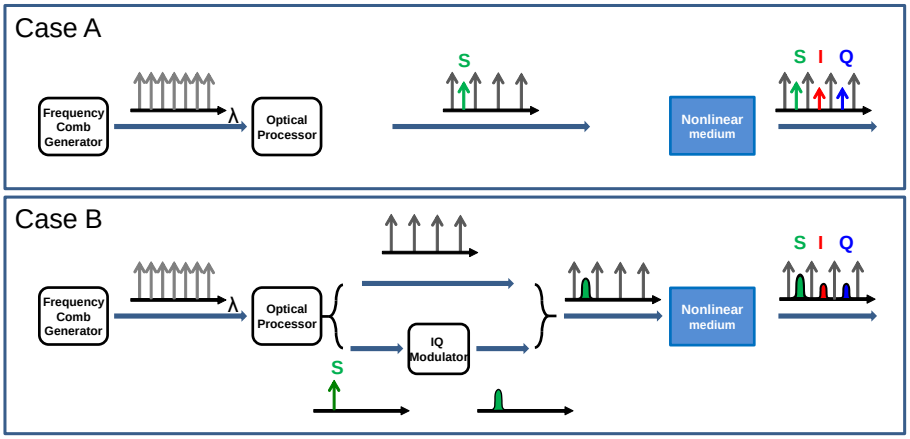

Figure 6.4: Block diagrams of the experimental setup: (case A) static characterization and (case B) system experiment.

An optical processor (Finisar Waveshaper) is then used to select four CW pumps separated by 80 GHz and a CW signal located in-between the shortest wavelength pumps.

For the static characterization (Case A), all the selected waves have been directed towards the same output port of the processor, therefore injecting into the nonlinear medium five CW signals. For the dynamic experiment (Case B), the signal is sent to a different output port, QPSK-modulated, recombined with the four pumps, and injected into the nonlinear medium.

In both cases, at the output of the nonlinear medium, the two idlers are generated in the empty slots between the pumps, I and Q being either two CW signals (Case A) or two BPSK signals (Case B).

In this investigation, three different nonlinear media have been considered, namely a standard HNLF, a PPLN waveguide, and a silicon waveguide with an embedded p-i-n junction for free carriers (FCs) removal (Section 5.2). Note that, due to the different dispersion properties of the the various nonlinear media investigated, the laser wavelength has been shifted accordingly.

The main physical properties of the three media are listed below, together with the wavelength at which the signal line of the frequency comb is tuned.

HNLF The HNLF length, attenuation, zero-dispersion wavelength, dispersion slope, and nonlinear coefficient are L =500 m, α =0.7 dB/km, λ_0 =1550.4 nm, S =0.0185 ps/(nm^2·km), and γ =10.7 W^{-1}·km^{-1}, respectively. The signal line is located at λ_s =1549.4 nm.

PPLN The PPLN waveguide (NEL, WH-0780-000-F-B-C) length, fiber-to-fiber insertion loss, conversion efficiency, and operation temperature of the waveguide are L =3 cm, 3.3 dB, 286 %/W, and 50°C, respectively. The signal line is located at 1561.4 nm and the temperature is tuned such that the quasi-phase matching (QPM) wavelength is set to λ_{QPM} =1562.4 nm, i.e. pump 3, leading to roughly equalized CEs for the two idlers.

Silicon The silicon waveguide propagation losses, two-photon absorption (TPA) coefficient, and nonlinear coefficient are equal to α =1 dB/cm, β_{TPA} =0.5 cm/GW, and γ =280 W^{-1}·m^{-1}, respectively. The signal line is set to λ_s =1549.1 nm.

6.5 Static characterization of phase-sensitive wavelength conversion

In order to meet the two fundamental requirements for the scheme, i.e. a 90° phase-shift between the idlers CEs versus signal phase responses, and a sufficient PER, the power levels and phases of the four pumps have been optimized together with the signal power by use of the optical processor. Starting from the results of the numerical optimization of Fig. 6.1(b) and (c), the nine optimization parameters have been fine tuned

experimentally for each medium.

In the case of the HNLF, the optimization has led to the phases and power levels of Table 6.1. Note that the phase of the signal is swept in order to produce the phase-dependent wavelength conversion curves.

Table 6.1: Experimental optimization results: power levels and phases of the five waves at the HNLF input.

	Pump 1	Pump 2	Pump 3	Pump 4	Signal
Power [dBm]	6.9	14.3	14.7	12.5	-2.5
Phase [rad]	1.1	0.3	1.4	0.1	-

It should be noted that, in order to neglect backscattering effects, the power per pump coupled into the HNLF has been kept below the SBS threshold (around 15 dBm for the HNLF used in this work as in Fig. 3.7(a)). In practice, SBS represents one of the main limitations to the increase in CE for the two idlers. However, several SBS mitigation methods such as fiber straining have the potential to increase the achievable CE [64]. In this experiment, a standard HNLF is used as the obtained CEs (around -10 dB) are sufficient to achieve error-free performances.

Using the settings of Table 6.1, the normalized CEs measured using an optical spectrum analyzer (OSA) at the HNLF output are reported in Fig. 6.5(a) together with the output spectra for three different values of the signal phase in Fig. 6.5(b). Using the HNLF as nonlinear medium, the CE curves show the desired phase shift and PERs in excess of 13 dB.

A similar optimization has been carried out for the PPLN waveguide described in Section 6.4. PPLN waveguides offer a more compact implementation compared to HNLFs, as well as a better SBS immunity, and have been proven effective for achieving phase-sensitive processing exploiting second-order nonlinearities [172, 173]. In fact, cascaded second-harmonic generation (SHG) and difference frequency generation (DFG) are functionally equivalent to FWM as discussed in Section 2.2.
Due to the damage threshold of the waveguide caused by the onset of the photorefractive effect, the total input power has been kept below 26 dBm, and the optimization under such constrain leads to the power levels and phases reported in Table 6.2.

In PPLN the photorefractive effect leads to crystal damage and distortion of the output beam and is thus the main limitation to the maximum

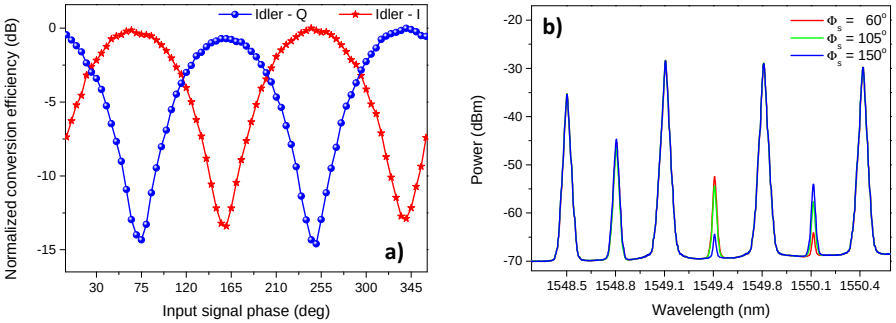

Figure 6.5: (a) Conversion efficiencies for I and Q as a function of the input signal phase obtained using the HNLF as nonlinear medium. (b) Spectra measured at the HNLF output for three values of the signal phase showing the maximum amplification for I ($\Phi_s = 60°$) and Q ($\Phi_s = 150°$), as well as the quadrature point ($\Phi_s = 105°$) where the idlers output powers are 3 dB below their maximum.

Table 6.2: Optimization results: power levels and phases of the five waves at the PPLN waveguide input.

	Pump 1	Pump 2	Pump 3	Pump 4	Signal
Power [dBm]	16.3	22.1	20.7	16.4	0.7
Phase [rad]	2.67	0.2	1.32	0	-

input power and in turn to the achievable CEs. Nevertheless, maximum CEs above -10 dB could also be reached. The full normalized CEs as a function of the signal phase are reported in Fig. 6.6(a) together with the output spectra for max amplification for I and Q as well as the quadrature phase-point in Fig. 6.6(b). Using the HNLF as nonlinear medium, the PERs exceed 20 dB for both idlers and the CE curves are ($90° \pm 5°$)-shifted in signal phase.

Finally, the scheme is tested using a silicon waveguide as nonlinear medium. As discussed in Section 5.2, silicon waveguides enable a more compact and SBS-tolerant implementation than HNLFs. Furthermore, silicon has the potential to enable a broader operation bandwidth than what is achievable in PPLN since it is not limited by a relatively narrow QPM bandwidth. In fact, even though the CE bandwidth in PPLN can be broadened using either temperature gradients along the waveguide [206], multiple

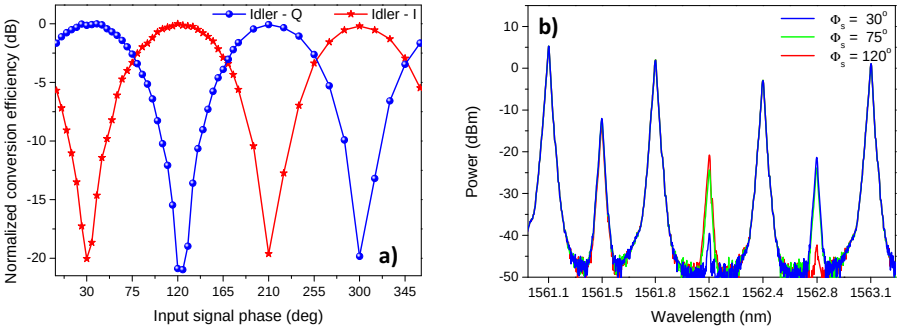

Figure 6.6: (a) Conversion efficiencies for I and Q as a function of the input signal phase obtained using the PPLN waveguide as nonlinear medium. (b) Spectra at the PPLN output for maximum amplification for Q ($\Phi_s = 30°$) and I ($\Phi_s = 120°$), as well as the quadrature point ($\Phi_s = 75°$).

QPM bandwidths [207], or dual-pump schemes [208], these approaches may lead to a reduced CE.

For silicon waveguides, the CE bandwidth can be tuned simply engineering the dispersion profile to the required specification by designing the cross-section of the waveguide, enabling CE levels comparable with PPLN [191] but potentially broader CE bandwidths.

The main challenge for nonlinear processing in silicon waveguides is, however, the high nonlinear loss due to TPA and FCs effects. As discussed in Section 5.2, the use of a reverse-biased p-i-n junction along the waveguide allows decreasing the accumulation of FCs. Using the waveguide described in Section 5.2 and characterized by the parameters listed in Section 6.4, the optimized power levels and phases are reported in Table 6.3.

Table 6.3: Optimization results: power levels and phases of the five waves at the silicon waveguide input.

	Pump 1	Pump 2	Pump 3	Pump 4	Signal
Power [dBm]	9.5	22.4	18.2	17.1	-9
Phase [rad]	2.83	0.45	0	0.24	-

The total power at the waveguide input is set to 24.8 dBm to keep the overall insertion losses to 14 dB with 25 V of bias voltage applied through DC probes ('contact voltage' as defined in Section 5.2).

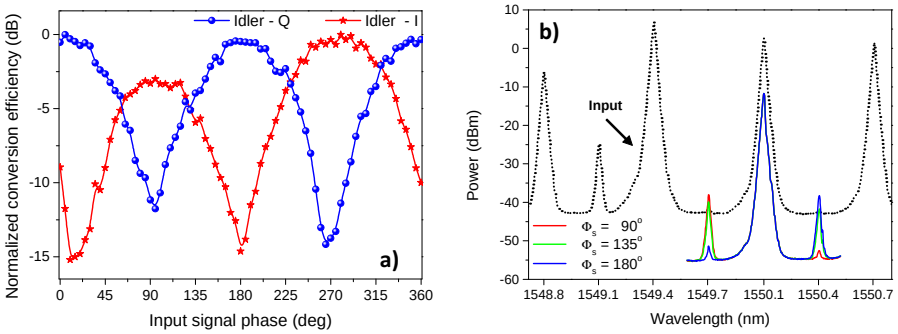

Figure 6.7: (a) Conversion efficiencies for I and Q as a function of the input signal phase obtained using the silicon waveguide as nonlinear medium. (b) Spectra at the silicon waveguide input (dotted) and output (restricted to the wavelength range around I, P3, and Q) for maximum amplification for I ($\Phi_s = 90°$) and Q ($\Phi_s = 180°$), as well as the quadrature point ($\Phi_s = 135°$).

Fig. 6.7(a) shows the normalized CE as a function of the input signal phase while input and output spectra (restricted to the wavelength range around I, P3, and Q) for max amplification for I and Q as well as the quadrature phase-point are reported in Fig. 6.7(b). The silicon waveguide provides PER values in excess of 14 dB similar to levels achieved with the HNLF. However, drifts in coupling over the measurement time have affected the results leading to a slight tilt in the CE curves.

6.6 Dynamic characterization of QPSK-to-2×BPSK conversion

After measuring promising PER levels for all the nonlinear media in static operation, the scheme is evaluate dynamically, i.e. for 10-Gbaud QPSK signals.

First the full system setup is introduced, focusing on the most challenging aspect, namely the phase-stabilization aimed at preserving the phase-coherence between the waves. Then, the performances are reported, showing successful discrimination of the two BPSK quadratures and presenting BER measurements realized using two of the nonlinear media introduced above, namely the HNLF and the PPLN waveguide.

Regardless of PER levels fulfilling the requirements for practical applications, high insertion losses may still limit the effectiveness of silicon waveguides for practical applications, leading to OSNR degradation, as discussed in Chapter 5. The dynamic characterization of the scheme has therefore not been carried out in this case.

6.6.1 Detailed system setup

The fully detailed experimental setup for the dynamic characterization (Case B) is shown in Fig. 6.8.

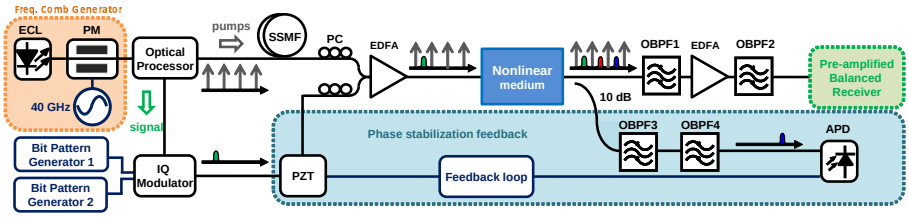

Figure 6.8: Experimental setup for dynamic phase-sensitive wavelength and format conversion of a 10-Gbaud QPSK signal.

A CW signal emitted by a narrow linewidth (∼100 kHz) external cavity laser (ECL) source is phase modulated with a 40-GHz radio frequency signal with a modulation index of 4.3 in order to generate an optical frequency comb with 40-GHz line spacing (see Appendix B). The optical processor is used to select four 80-GHz spaced pumps and a signal out of the frequency comb and to adjust their power levels and relative phases to achieve transfer functions similar to the targets of Fig. 6.1(b) and (c). Unlike for the static characterization, the optical processor is also used to separate the signal from the pumps by outputting it to a different port so that it could be modulated in the QPSK format at 10 Gbaud using a standard IQ modulator. The modulator is driven by two non-return-to-zero (NRZ) signals at 10 Gbps carrying two PRBSs coming from two independent bit pattern generators (BPGs) synchronized with a common reference signal at 10 GHz. The pumps spacing is limited by the electronics used for the comb generation as well as the ability of the optical processor to suppress the undesired comb lines. The pumps spacing in turn limits the signal bitrate, while no strong constraints (e.g. pattern effects, CE bandwidth) are set by the chosen nonlinear media. The pumps are propagated through around 10 m

of standard single mode fiber (SSMF) and coupled back together with the signal via a 3-dB coupler. The length of SSMF has been optimized in order to approximately match the pumps and signal path lengths down to 0.5 m in order to ease the operation of the phase control loop aiming at compensating for slow thermal drifts. A pair of polarization controllers (PCs) align the state of polarization (SOP) of the pumps and signal, maximizing the FWM efficiency. In the case of PPLN, the SOPs are aligned to the TE mode of the waveguide.

At the nonlinear medium output, a pair of OBPFs (i.e. OBPF 1 and OBPF 2 in the figure) with 0.5-nm and 0.3-nm FWHM bandwidths, respectively, are used to select one of the idlers at a time and inject it into a pre-amplified BPSK balanced receiver for BER testing. An erbium-doped fiber amplifier (EDFA) located between the OBPFs compensates for their insertion losses. Finally, phase-to-intensity demodulation is performed in the receiver by a 1-bit (100 ps) delay interferometer (DI) followed by a BPD with cut-off frequency of 45 GHz.

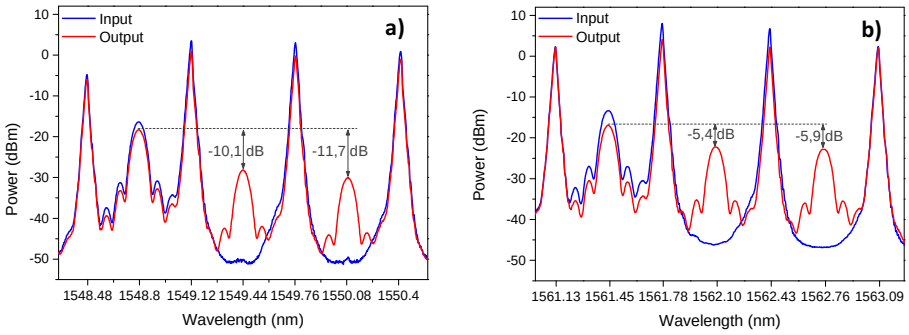

Figure 6.9: Optical spectra at the input and output of (a) HNLF and (b) PPLN waveguide for a 10-Gbaud QPSK-modulated input signal. The labels show the achieved CE values.

The spectra at the input and output of the HNLF and the PPLN waveguide are reported in Fig. 6.9(a) and (b), respectively. The existence of two modulated idlers is clearly confirmed by the output spectra, showing output CEs around -11 dB for the HNLF and -6 dB for the PPLN waveguide.

The splitting of pumps and signal and their propagation along different paths inevitably results in a partial loss of phase coherence due to thermal effects, even when balancing the paths lengths. In order to lock the waves in phase, 10% of the nonlinear medium output power is taped out for a phase stabilization feedback loop. The idler Q is selected through two

fixed OBPFs (i.e. OBPF 3 and OBPF 4) with 0.3-nm and 0.8-nm FWHM bandwidths, detected by a low-speed avalanche photodiode (APD) (50-MHz 3-dB bandwidth) and used as reference for a feedback loop based on a piezoelectric actuator (PZT) with a 15-kHz bandwidth. It should be noted that the same reference idler and feedback loop conditions have been used for both received idlers, showing the simultaneous conversion of the two orthogonal quadratures of the original QPSK signal.

The phase stabilization mechanism relies on tracking the average power variations of idler Q as the relative phase between signal and pumps drifts. The phase-sensitive FWM and cascaded SHG/DFG directly map the phase drifts into power variations of the idlers.

Each of the four $\pi/2$-spaced constellation points of the input QPSK signal are moved along the CE versus input signal phase curve such that each point follows the sine square trend of Fig. 6.1(b). As the phase drifts occur on a time scale orders of magnitude slower than the signal bitrate, the relative $\pi/2$ phase difference between neighbor constellation points is preserved. Therefore, once the gain for one point decreases due to a phase drift, the gain of its neighbor increases being on the opposite slope of the sine square curve ($\pi/2$-shifted in signal phase). The slow speed photodiode is unable to track the fast power variations, therefore the fluctuations are averaged out leading to a constant output power for the two idlers, regardless of phase drifts as sketched in Fig. 6.10(a).

That is indeed the case for an ideal QPSK signal. Practically, however, due to the high tolerance of interferometric detection to a sub-optimum voltage bias applied to the phase-shifter in the IQ modulator [209], as well as the practical tuning precision, even optimizing the bias for best performances of the QPSK signal, a small residual IQ quadrature error between in-phase and quadrature leads to weak power fluctuations. The effect is illustrated schematically in Fig. 6.10(b), where the actual error has been significantly exaggerated for the sake of clarity. These weak fluctuations can still provide a locking reference for the phase stabilization scheme once the output voltage of the APD has been appropriately amplified and filtered.

Such power fluctuations can be minimized if the original QPSK signal is rotated such that the constellation points "match" closely the quadrature points of the CE curves, i.e. 3 dB below the maximum. Fortunately this corresponds to the desired locking point as they correspond to the area of maximum flatness of the phase transfer function (Fig. 6.1(c)). A misalignment, in fact, would result in excess phase noise added to the BPSK idlers through the conversion. Furthermore, a QPSK signal aligned to match the

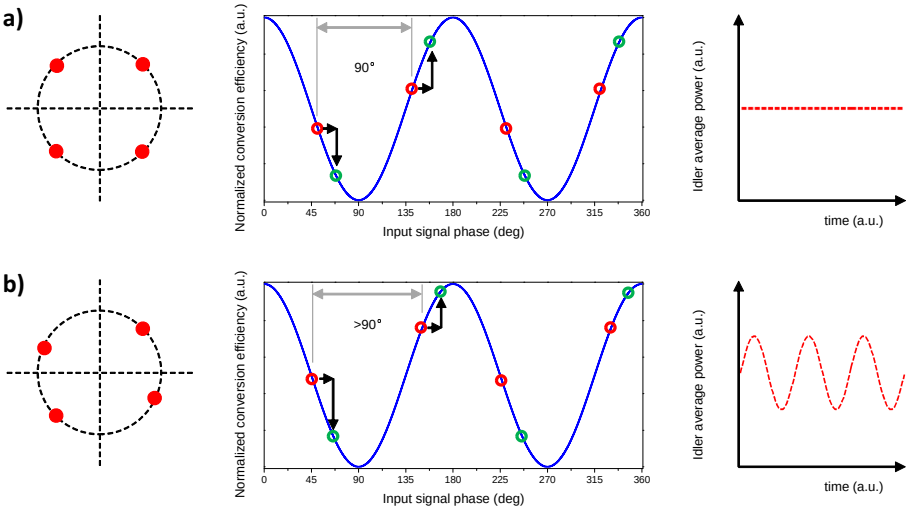

Figure 6.10: (left) Constellation diagrams, (center) position of the four original QPSK points (red circles) as the phase drifts (black arrows) and they move along the CE (green circles) and (right) average idler power variations over time. (a) Ideal QPSK signal and (b) QPSK signal with an IQ quadrature error. Remark that the quadrature error has been significantly exaggerated for clarity.

position of maxima and minima in the CE curve would be converted to two OOK-modulated idlers. The information carried by both I and Q would then be the result of an exclusive OR operation between the datastreams carried by the two quadratures of the original signal, with consequent loss of information.

Keeping the QPSK signal aligned at the quadrature points of the CE corresponds to locking to the most linear part of the transfer function. A simple loop filter based on a proportional integrator therefore suffices to achieve the desired locking conditions, with no need for frequency dithering.

6.6.2 System performances

In order to verify the successful conversion of the two quadratures of the QPSK signal to different wavelengths, two different sequences have been applied to the electrical inputs of the IQ modulator, i.e. a PRBS of length $2^7 - 1$ for $\mathrm{DATA_I}$ and a PRBS of length $2^9 - 1$ for $\mathrm{DATA_Q}$. A digital sampling oscilloscope is then used at the receiver to save 50 bits demodulated

from each idler, indeed proving that I is carrying $\mathrm{DATA_I}$ while $\mathrm{DATA_Q}$ can be retrieved from Q. The electrical waveforms after interferometric demodulation and balanced detection are shown in Fig. 6.11(a) and (b), together with the binary values of the corresponding PRBSs, showing that indeed the data carried by the phases of the generated idlers match the original PRBSs modulated on each quadrature of the QPSK signal. The nonlinear medium used is the HNLF and the thickness of the recorded oscilloscope traces are partly caused by a sub-optimum phase stabilization loop which does not fully and instantaneously compensate for the phase drifts, leading to weak power fluctuations over the acquisition time.

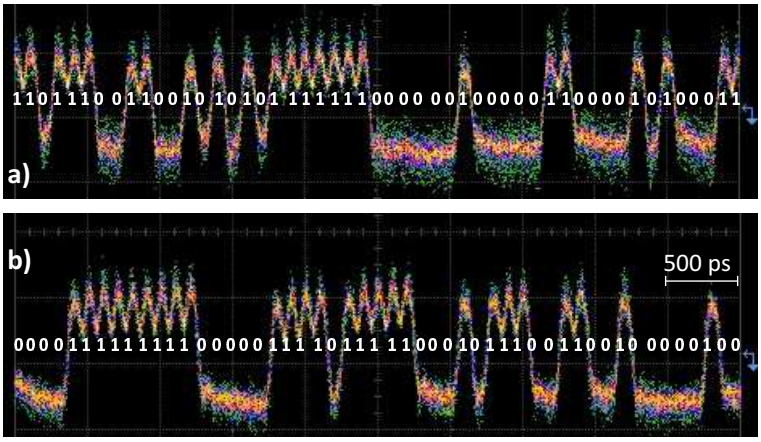

Figure 6.11: Temporal waveforms saved by a digital sampling oscilloscope at the receiver side after interferometric demodulation and balanced detection for (a) I (corresponding to a $2^7 - 1$ PRBS) and (b) Q (corresponding to a $2^9 - 1$ PRBS). The nonlinear medium used is the HNLF.

The performances of the two converted idlers at the HNLF output have then been evaluated through BER measurements. In these measurements, decorrelated PRBSs of length $2^{15}-1$ have been used as $\mathrm{DATA_I}$ and $\mathrm{DATA_Q}$. The measured idlers BERs as functions of the average received power are shown in Fig. 6.12(a) and compared with back-to-back performances for both a BPSK signal at 10 Gbps and a QPSK signal at 10 Gbaud. The reference BPSK signal is demodulated using the 100-ps DI. Regarding the reference QPSK, the two quadratures are demodulated one at a time using the same 100-ps DI and tuning the bias point of the DI to different values. It should be noted that, for the back-to-back QPSK quadratures, the demodulated signal is no longer a simple PRBS (as are the original

electrical $DATA_I$ and $DATA_Q$), since no differential encoding had been applied at the transmitter [204]. Instead, the error analyzer is programmed with the expected patterns. The available memory in the error analyzer limited the length of the PRBS that could be used for testing. However, comparison between PRBSs of lengths 2^7-1 and $2^{15}-1$ showed no difference in performances for the scheme under investigation, as expected by the ultra-fast nature of FWM, thus longer sequences are also believed to lead to equivalent performances.

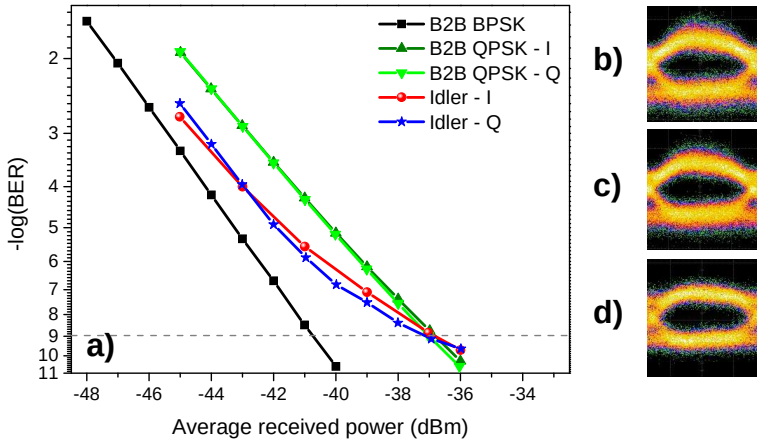

Figure 6.12: (a) BER performances for the converted idlers together with back-to-back QPSK and BPSK as references using the HNLF as nonlinear medium. Eye diagrams for (b) I, (c) Q and (d) one quadrature of the demodulated back-to-back QPSK signal for a received power of −35 dBm and 10 s of acquisition time.

A comparison between the detected BPSK idlers and the demodulated back-to-back QPSK signal shows a sensitivity improvement above 1.5 dB at a BER of 10^{-3} and equal performances at a BER of 10^{-9}. Similarly to the trace thickness in Fig. 6.11, the slight tilt of the BER curves for the idlers at high received power is partly caused by the sub-optimum stabilization which leads to more severe impairments as the gating time needed to obtain a reliable error counting gets longer. Nevertheless, clear and open eye diagrams can be seen (Fig. 6.12(b) to (d)). A power penalty of about 4 dB is measured at a BER of 10^{-9} for the converted idlers compared to the simple case of BPSK modulation and interferometric detection.

It should also be mentioned that the specific measurements reported in Fig. 6.12 have been obtained using as feedback the same idler under

measurement due to equipment availability. However, the performances have been verified afterwards keeping the feedback locked on one of the idlers (Q in the specific case) and measuring both BER curves under the same locking conditions. That proves the simultaneous conversion of both QPSK-quadratures to different wavelengths.

The BER performances have also been investigated using the PPLN waveguide as nonlinear medium. The results for a PRBS of length $2^7 - 1$ are shown in Fig. 6.13(a).

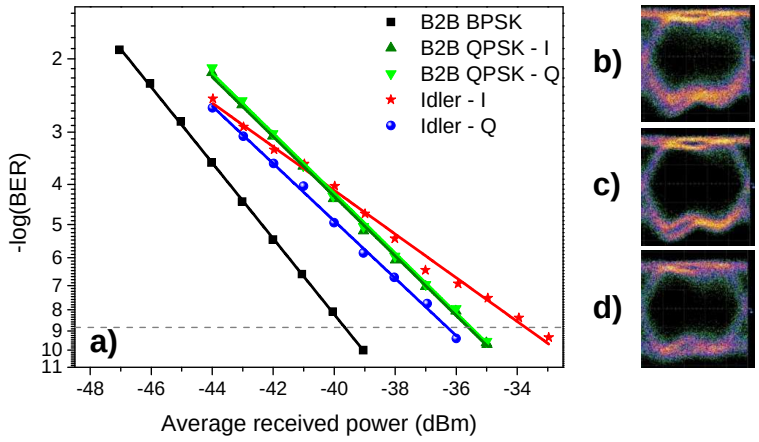

Figure 6.13: (a) BER performances for the idlers together with back-to-back QPSK and BPSK as references using the PPLN waveguide as nonlinear medium. Eye diagrams for (b) I, (c) Q, and (d) one quadrature of the demodulated back-to-back QPSK (-36 dBm received power).

Both idlers could be detected error-free, with sensitivities of -33.5 dBm and -36 dBm, for I and Q, respectively. A comparison between the detected BPSK idlers and the demodulated back-to-back QPSK signal shows a better sensitivity at low average received power for both idlers. At higher power levels, however, the sensitivity improvement of Q decreases while the performance of I degrades, reaching a power penalty of 2 dB at a BER of 10^{-9}. The degradation is mainly caused by a sub-optimum locking position for the phase stabilization, which could be related to a slight mismatch in the phase-orthogonality between the conversion efficiencies of the two idlers. It is believed that a more thorough tuning of the pumps phases and power levels would allow achieving similar performances for the two idlers, as shown in Fig. 6.12 for a HNLF. As mentioned above, also in this case, the worsen-

ing of the performance is more severe for lower BER values when a longer gating time, therefore longer-lasting stability, is required. Nevertheless, a PPLN waveguide is proven a suitable nonlinear medium for implementing the scheme with error-free performance obtained for both converted idlers and showing clear and open eye diagrams (Fig. 6.13(b)-(c)).

6.7 Summary

In this chapter, a novel multi-pump PSA scheme enabling simultaneous QPSK-to-2×BPSK modulation format and wavelength conversion proposed in [25] is investigated.
Firstly, the operation principle is introduced and a potential application of the scheme to improve the phase-noise tolerance of balanced QPSK receivers is numerically investigated. An OSNR improvement above 2 dB over conventional balanced receivers is shown. Following, static characterization, i.e. under CW operation, of the scheme is experimentally reported using three different nonlinear media: a standard HNLF, a PPLN waveguide, and a silicon waveguide with a reverse-biased p-i-n junction for FCs removal. The measured CEs for I and Q are 90° shifted in signal-phase for all the three scenarios with PER in excess of 13 dB for all the media. The conversion of both complex quadratures $\mathrm{DATA_I}$ and $\mathrm{DATA_Q}$ of a 10-Gbaud QPSK signal to two distinct BPSK idlers I and Q has then been experimentally proven transmitting different sequences for I and Q using a HNLF as nonlinear medium. Finally, the BER performances have been analyzed implementing the scheme with a HNLF and a PPLN waveguide. Error-free performances (BER of 10^{-9}) are reported with limited power penalty compared to the detection of the QPSK signal using a 1-symbol delay interferometer. The performances are mainly limited by the phase stabilization feedback loop.

Chapter 7

Conclusions and future work

The great potential of parametric amplification to provide critical functionalities for optical signal processing and amplification in future optical networks is being intensively investigated with numerous breakthroughs being reported in very recent years. Along this direction, four main applications of optical parametric amplifiers (OPAs) have been explored during this Ph.D. project, namely amplification (Chapter 3), optical phase conjugation (OPC) (Chapter 4), signal phase-regeneration (Chapter 5), and modulation format conversion (Chapter 6).

The key results presented in the aforementioned chapters are summarized in the following sections. Additionally, an outlook on future research directions and aspects worth investigating starting from this project's findings are also provided for each topic.

7.1 Amplification

OPAs may have the potential to compete with erbium-doped fiber amplifiers (EDFAs) for in-line amplification as they provide several advantages, first of all in terms of amplification bandwidth. Therefore, for future applications, it is critical to understand their limitations, especially with respect to amplification of advanced modulation formats.
Chapter 3 focuses precisely on this aspect, investigating the performances of a single-pump fiber optical parametric amplifier (FOPA) for amplification of 16-quadrature amplitude modulation (QAM) signals looking into both unsaturated and saturated gain regimes.
A numerical analysis shows that keeping the input signal power below

the 1-dB gain saturation threshold is required to ensure low performance degradation of the amplified signal. Furthermore, the impact of saturated amplification on the different modulation states of the 16-QAM constellation is studied. Gain differences between the symbols, as well as different nonlinear phase rotations experienced, are discovered to be the main causes of signal distortion. Then, the interplay between saturation and amplitude-to-phase noise conversion in the FOPA also plays a role in further impairing the signal. The bitrate independence of these effects has been highlighted and it has been shown that a simple figure of merit (FOM), introduced in [24] and based on the power ratio between output-signal and input-pump, is sufficient to characterize the signal degradation. The numerical findings are also confirmed experimentally by investigating the constellation distortion of a 14-Gbaud 16-QAM signal.

These results have actually already been complemented in a very recent paper from Sackey *et al.* [124], where the single-channel investigation presented in Chapter 3 has been extended to a wavelength-division multiplexing (WDM) scenario with very similar conclusions being drawn.
In order to understand the full potential of FOPAs for in-line amplification though, the impact of multiple amplification stages needs to be investigated. This has yet to be explored for QAM signals.

7.2 Optical phase conjugation

The transmission of advanced modulation formats is ultimately limited by Kerr nonlinearity. Optical phase conjugation (OPC) is a well-known technique to compensate for the nonlinear distortion and can be implemented in OPAs, as signal amplification automatically provides the generation of a high-quality phase-conjugated copy of the signal (idler).
The focus of Chapter 4 has, thus, been directed towards the design and optimization of a fiber-based OPC device exploiting parametric effects in a highly nonlinear fiber (HNLF).
Desirable requirements for a black-box OPC device to be employed in future optical networks include broadband operation, low insertion losses or potentially net gain, modulation format and polarization independence, and ideally no, or at least low, signal degradation. FOPAs automatically fulfill the first two conditions. A dual-pump FOPA can achieve high conversion efficiency (CE) over a broad bandwidth: in the scheme presented a flat gain profile could be obtained over 18 nm even for 13-dB on-off gain.

Furthermore, the ultra-high speed Kerr nonlinearity allows for modulation format independence, as long as the detrimental saturation effects discussed in Chapter 3 are avoided. In order to provide the polarization independence, a diversity loop configuration has been optimized achieving polarization-dependent gain (PDG) levels below 0.5 dB even in the high gain regime (13 dB). Keeping the signal degradation low is perhaps the most critical and challenging aspect and was achieved by optimizing the pumps phase-dithering in a counter-phasing fashion to prevent the pumps phase-modulation to be transferred to the idler as phase noise. By using such a design, an optical signal-to-noise ratio (OSNR) penalty below 1 dB could be achieved at 5-dB on-off gain for a five-channel WDM polarization-division multiplexing (PDM) 16-QAM signal (1.12 Tbps).
After the back-to-back characterization of the OPC device, two different system scenarios have been considered to benchmark the performances of a transmission system using the OPC device to provide mid-span spectral inversion (MSSI) against straight transmission. First, a fully dispersion-compensated link using lumped EDFA-based amplification has been assessed for total transmission lengths of 480 km, 640 km, and 800 km. Significant improvements have been measured for all the transmission distances reaching 1.3-dB and 0.9-dB increases in Q-factor after 800-km transmission for single- and five-channel signals, respectively. Additionally, a dispersion-uncompensated link using distributed Raman amplification with backward pumping has also been investigated transmitting over 400 km. In this scenario the improvement was found to be 1.1 dB and 0.8 dB for single- and five-channel signals, respectively.

An alternative well-known scheme to provide polarization-independent OPC relies on the use of polarization-orthogonal pumps. It could be interesting to compare the degradation introduced by the OPC operation for the two different schemes. Furthermore, verifying the modulation format independence comparing the Q-factor improvement provided by the MSSI for different modulation formats, as well as increasing the number of WDM channels would contribute making the scheme more appealing for future flexible networks. Finally, the use of multiple OPC operations has been shown in [158] for PDM quadrature phase-shift keying (QPSK) signals, as a single MSSI stage did not provide sufficient improvement. Increasing the number of OPC stages for longer transmissions may increase further the improvement provided by the nonlinear compensation.

7.3 Phase regeneration

Most of the very recent breakthroughs in terms of phase regeneration have been achieved using HNLFs as nonlinear media. However, silicon waveguides combine a small footprint with a stronger nonlinear coefficient and potentially higher stimulated Brillouin scattering (SBS) immunity. Additionally, silicon photonics can take advantage of the well-established fabrication know-how from CMOS technology. Nevertheless, optical signal processing in silicon is limited by nonlinear absorption, which strongly impairs the nonlinear interaction. The use of a novel waveguide design with a reverse-biased p-i-n junction fabricated along the waveguide enables to keep free carrier absorption (FCA) and free carrier dispersion (FCD) to a minimum by preventing the accumulation of free carriers (FCs) in the waveguide. This solution allows a drastic increase in the achievable CE with values as high as -0.7 dB having been reported [191]. A high-efficiency nonlinear interaction is critical for phase-sensitive processing. The static characterization, i.e. under continuous wave (CW) operation, of the phase-sensitive performances of a dual-pump degenerate OPA based on such silicon waveguide resulted in measured phase-sensitive extinction ratios (PERs) in excess of 20 dB, as presented in Chapter 5. These values represent a two-order of magnitude increase compared to the levels measured without the p-i-n junction as well as one-order of magnitude increase compared with the highest reported value to date (11 dB) obtained under pulsed operation at 38.6 MHz in slow-light photonic crystal waveguides [178]. Furthermore, removing the need to operate in a pulsed regime permits to use the scheme for processing of high-speed signals. The first demonstration of phase regeneration on a silicon platform is then shown for a differential phase-shift keying (DPSK)-modulated signal at 10 Gbps. Even though the high insertion losses of the waveguide and a sub-optimum phase stabilization feedback loop introduced some degradation for a clean signal, decreases in power penalty up to more than 14 dB have been measured for DPSK signals with added phase noise.

At the present stage, two main obstacles limit the performances from the device point of view: the high insertion losses as well as the lack of dispersion engineering. Lowering the overall insertion losses, for example decreasing the coupling losses through more complex coupling structures, may increase the achievable PER or equivalently reduce the input pump power required. Furthermore, the grating coupler losses ($\sim$ 4.5 dB/coupler)

are believed to be a significant source of OSNR degradation hindering the quality of the output signal.
Additionally, having an anomalous dispersion in the 1550-nm region would enable a major increase in CE further contributing in an increase in PER.
Such improvements may be combined with the strong potential for integration provided by silicon photonics to construct more complex schemes.
Even though QPSK regeneration has been demonstrated also without the need for demultiplexing the signal into two binary phase-shift keying (BPSK) tributaries [114], an integrated diversity scheme may be more compact and easier to implement on a silicon platform.

7.4 Modulation format conversion

Several methods have been proposed to provide QPSK-to-BPSK conversion. Most of them, however, end up demultiplexing only one quadrature discarding 50% of the information carried by the original signal [117, 199].

A novel scheme enabling simultaneous QPSK-to-2×BPSK modulation format and wavelength conversion without loss of information was proposed in [25].
The approach is based on the use of a four-pump phase-sensitive OPA and combines the ability to split the two BPSK tributaries to different wavelengths with phase-regeneration capabilities. The operation principle of this method is based on the phase-sensitive generation of two idlers with CEs which are 90° phase-shifted in the input signal phase, leading to the conversion of one BPSK tributary to each idler. Achieving the phase-orthogonality condition between the CEs is particularly challenging as it requires the optimization of power levels and phases of the four pumps as well as the signal power. Efficient phase noise suppression, then, further requires a high PER for both idlers, bringing extra constraints for the optimization. Nevertheless, performing first a coarse optimization numerically and, then, fine tuning the values experimentally enabled to measure the desired 90°-shift in signal phase between the two CEs with PERs in excess of 13 dB for both idlers. Such a static characterization has been performed for three different nonlinear media: a standard HNLF, a periodically poled lithium niobate (PPLN) waveguide, and a silicon waveguide with a reverse-biased p-i-n junction for FCs removal. All the media showed comparable performances, highlighting the flexibility of the scheme in terms of practical implementation. Furthermore, the

correct conversion of the two tributaries have been experimentally verified at 10-Gbaud by encoding different data sequences into the two QPSK quadratures. Error-free performances (bit-error ratio (BER) of 10^{-9}) have been measured with no or limited power penalty compared to balanced detection of the original QPSK signal both for a HNLF- and a PPLN-based implementations.

The performances have been mainly limited by the implemented phase stabilization feedback loop aimed at compensating for phase drifts between signal and pumps. The stabilization system was based on tracking the power fluctuations of only one idler. A more complex approach based on comparing both idler simultaneously may provide higher accuracy, potentially enabling to better match the numerically predicted regeneration levels.
Furthermore, the waves allocation for these experiments has been fixed to a 40-GHz grid. The numerical investigations of [201] have predicted that higher flexibility in the idlers wavelengths may be possible without impacting the performances but rather decreasing the number of pumps required down to three. Experimental verification has, however, yet to be reported. Finally, a major challenge for the scheme, which still needs to be tackled, is the generation of four (or three) pumps which are all phase-coherent with the signal. Different methods have been described in the case of two pumps, mainly relying on additional four-wave mixing (FWM) stages [23, 107]. These solutions, however, scale poorly when four pump waves are needed.

Appendix A

Split-step Fourier method

In this appendix, a brief introduction to the split-step Fourier method to solve the nonlinear Schrödinger equation (NLSE) is outlined.

The NLSE has been presented in Section 2.2 and the physical effects are discussed there in details. Here the focus is directed towards the mathematical formulation and the numerical approach to solve the equation.

The NLSE in the formulation of Equation (2.3), i.e. neglecting Raman and self-steepening effects, is repeated below:

$$\frac{\partial}{\partial z}A = -\frac{\alpha}{2}A + \left(\sum_{n=1}^{N}(-i)^{n+1}\frac{\beta_n}{n!}\frac{\partial^n}{\partial t^n}\right)A + i\gamma|A|^2A - \frac{\beta_{TPA}}{2A_{\text{eff}}}|A|^2A + i\beta_F A\,, \tag{A.1}$$

where α represents the linear propagation loss term, β_n the n-th order dispersion term, γ and β_{TPA} Kerr and two-photon absorption (TPA) coefficients, A_{eff} the effective area, and β_F the free carriers (FCs) effects, as discussed in Section 2.2.

In this thesis, the presented numerical investigations have been mainly focused on solving the equation to describe the propagation in optical fibers, therefore neglecting TPA and FCs effects ($\beta_{TPA} = 0; \beta_F = 0$). Hence, the focus is initially directed towards the interplay between dispersion and Kerr nonlinearity taking place in highly nonlinear fibers (HNLFs) as discussed in Section A.1. The extension of the model for silicon waveguides, i.e. including TPA and FCs effects is then shortly described in Section A.2.

A.1 Split-step Fourier method for optical fibers

The NLSE can be solved analytically if either the group-velocity dispersion (GVD) or the Kerr nonlinearity are taken into account separately. When both effects are considered, an analytical solution can still be derived but only under a special condition: soliton propagation [26]. For more general scenarios, numerical approaches need to be employed, the most common for optical fiber is known as *split-step Fourier method*.
Neglecting TPA and FCs effects, (A.1) can be rewritten as:

$$\frac{\partial}{\partial z}A(z,t) = \left(\hat{D} + \hat{N}\right) A(z,t)\,, \tag{A.2}$$

where the linear $\hat{D}$ and nonlinear $\hat{N}$ operators are defined as:

$$\hat{D}(\omega) = -\frac{\alpha}{2} + \left(\sum_{n=1}^{N}(-i)^{n+1}\frac{\beta_n}{n!}\frac{\partial^n}{\partial t^n}\right) \tag{A.3}$$

$$\hat{N}(z,t) = -i\gamma|A(z,t)|^2 \tag{A.4}$$

The split-step Fourier method, then, makes use of the fact that analytical solutions can be easily derived if only $\hat{D}$ or $\hat{N}$ are considered. The two operators are, therefore, applied separately: the linear part is solved in the frequency domain, whereas the nonlinear part is solved in the time domain. Looking at one operator at the time, if $\hat{N} = 0$, then the field after a step Δz can be expressed as:

$$\frac{\partial}{\partial z}\tilde{A}(z,\omega) = \hat{D}(\omega)\tilde{A}(z,\omega) \quad \rightarrow \quad \tilde{A}(z+\Delta z,\omega) = \tilde{A}(z,\omega)e^{\hat{D}(\omega)\Delta z}\,, \tag{A.5}$$

where $\tilde{A}(z,\omega)$ is the Fourier transform of $A(z,t)$.
If $\hat{D} = 0$, instead, the analytical solution can be written as [20]:

$$\frac{\partial}{\partial z}A(z,t) = \hat{N}(z,t)A(z,t) \quad \rightarrow \quad A(z+\Delta z,t) = A(z,t)e^{\hat{N}(z,t)\Delta z}\,. \tag{A.6}$$

Combining the two steps yields:

$$A(z+\Delta z,t) \approx \mathcal{F}^{-1}\left\{e^{\hat{D}(\omega)\Delta z}\mathcal{F}\left\{e^{\hat{N}(z,t)\Delta z}A(z,t)\right\}\right\}\,. \tag{A.7}$$

Dividing the fiber into sections of length Δz (*step size*) and applying Equation (A.7) for a number of times equal to $N = L/(\Delta z)$, the field at the fiber output can be calculated with a precision strongly dependent on the chosen step size.

Generally, the approach outlined here, known as asymmetrical split-step, leads to a quadratic error in the step size due to the fact that $\hat{D}$ and $\hat{N}$ do not commute. The error is, therefore, proportional to the commutator between the two operators.

A common way to improve the accuracy to a cubic precision relies on a symmetrical version where, first, a half linear step is applied ($\Delta z/2$), followed by a full nonlinear step, and again a half linear step.
A graphical explanation of the symmetrical Split-step Fourier method is shown in Fig. A.1: this approach has been implemented and used throughout the thesis.

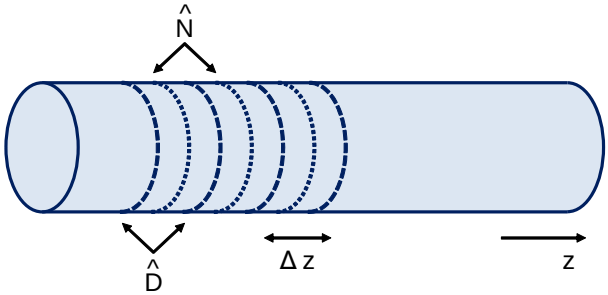

Figure A.1: Graphical explanation of the split-step Fourier method inspired from [26]. The linear step is calculated between the dashed midplane lines while the nonlinear step between the dotted ones.

Fig. A.2 then compares the parametric gain spectra of a single-pump fiber optical parametric amplifier (FOPA) calculated with the theoretical expression of Equation (2.26), with the numerical results obtained solving the coupled equations of Section 2.3 (Fig. 2.5), and by solving the NLSE with the split-step Fourier method outlined here. Excellent agreement can be seen between the three methods validating the numerical code.

A.2 Split-step Fourier method for silicon waveguides

The approach described in the previous section for optical fiber can be applied to silicon waveguides as well. However, as discussed in Section 2.2, neglecting TPA and FCs effects is not a valid approximation anymore, therefore, the two additional term in the NLSE need to be taken into account.

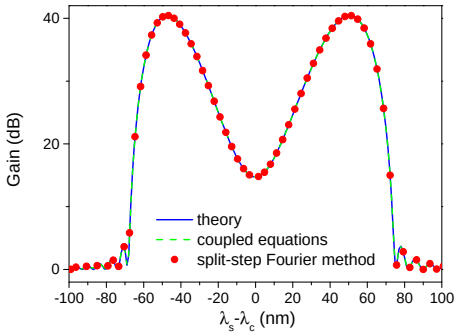

Figure A.2: Single-pump parametric gain spectrum as in Fig. 2.5: comparison between theory, coupled equations method and full NLSE solution using the split-step Fourier method.

The impact of TPA can be easily included in the nonlinear operator and an analytical solution can be derived splitting the field differential equation into a coupled differential equations for power and phase as in:

$$\begin{cases} \frac{\partial}{\partial z}|A| = -\frac{\alpha}{2}|A| + \gamma_I|A|^3\,, \\ \frac{\partial}{\partial z}\Phi = -\gamma_R|A|^2\,. \end{cases} \tag{A.8}$$

The above system can be solved analytically leading to [210]:

$$\begin{cases} |A| = \sqrt{\frac{|A(0,t)|^2 e^{\alpha z}}{1-2\gamma_I|A(0,t)|^2 L'_{\text{eff}}}} \\ \Phi = \frac{\gamma_R}{2\gamma_I}\log\left(1-2\gamma_I L'_{\text{eff}}|A(0,t)|^2\right) + \angle A(0,t)\,, \end{cases} \tag{A.9}$$

where $L'_{\text{eff}} = (1-e^{-\alpha dz})/\alpha$.

Taking into account only TPA but not FCs effects may be useful to model silicon waveguides where FCs are swept out of the waveguide by, for example, a reverse-biased p-i-n junction (see Section 5.2). However, even though a p-i-n junction can effectively reduce the carrier lifetime by several orders of magnitude, neglecting completely FCs effects provides only approximated results.
In order to accurately model nonlinearities in silicon, it is required to solve the full NLSE of Equation (A.1), and to do so, the first step is understanding the time-evolution of the FCs density N_c. Electron-holes pairs are generated through TPA and decay with an effective carrier lifetime τ_0. The carrier

density can be described by the differential equation (2.14), repeated below:

$$\frac{\partial}{\partial t}N_c(z,t) = \frac{\beta_{TPA}}{2h\nu_0}\frac{|A(z,t)|^4}{A_{\text{eff}}^2} - \frac{N_c}{\tau_0}\,. \tag{A.10}$$

In the case of continuous wave (CW) signals propagating through the waveguide, the equation can be solved analytically leading to a steady-state solution:

$$N_c(z) = \frac{\tau_0\beta_{TPA}}{2h\nu_0 A_{\text{eff}}^2}|A(z,\tau)|^4\,. \tag{A.11}$$

Generally, however, the equation needs to be solved numerically taking into account that the carrier density evolution is characterized by a transient period lasting around $5\times\tau_0$ and leading to a steady-state distribution [210]. In order to solve the NLSE, then, the carrier distribution needs to be calculated at every step z' of the propagation. Once $N_c(t,z')$ is known, TPA, free carrier absorption (FCA), and free carrier dispersion (FCD) can be added as additional terms to Kerr nonlinearity in the nonlinear operator. Notice that an analytical solution has yet to be reported for this general scenario and the nonlinear operator needs to be solved numerically, for example using the Runge-Kutta method [211].

A validation of the implemented numerical model with the simulation results of [212] is reported in Fig. A.3.
A Gaussian pulse has been propagated through a 2-cm silicon waveguides characterized by the parameters of [212] for intensities of 1.2 GW/cm^2, 6.0 GW/cm^2, and 12.5 GW/cm^2, with the self-phase modulation (SPM)-broadened output spectra shown in Fig. A.3(a), (b), and (c), respectively. The phase shift across the pulse, instead, is shown in Fig. A.3(d). The numerical results match perfectly the results of [212, Fig. 2] for all the cases considered.

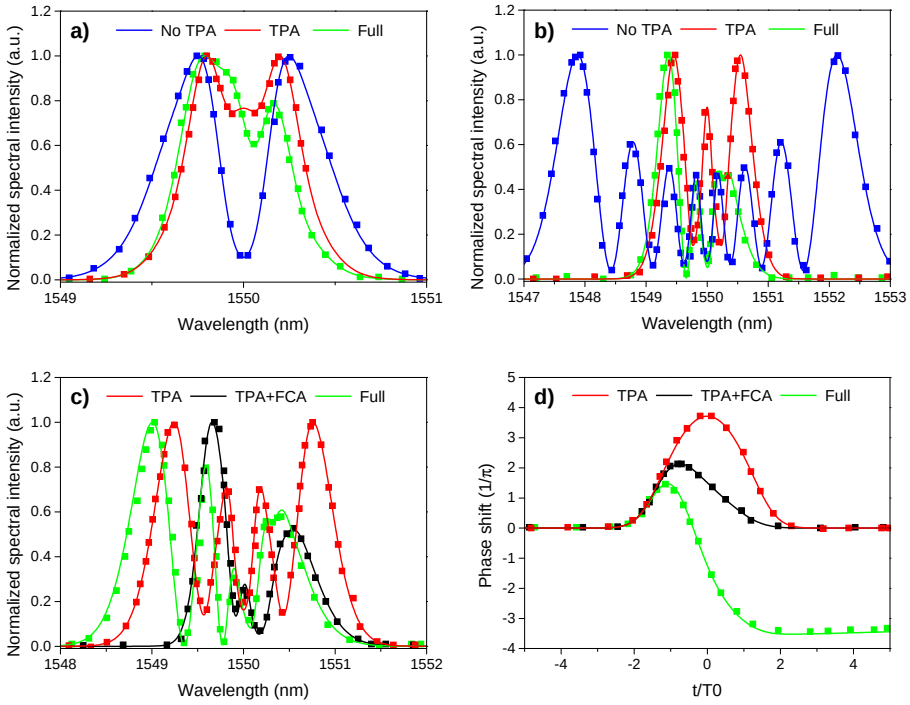

Figure A.3: SPM broadened spectra for an input Gaussian pulse with intensity of (a) 1.2 GW/cm^2, (b) 6.0 GW/cm^2, and (c) 12.5 GW/cm^2 and (d) temporal phase shift for 12.5 GW/cm^2. The numerical simulations (continuous lines) are compared with data from [212, Fig. 2] (squares).

Appendix B

Frequency comb

Frequency combs have been raising a significant interest in recent years, as the generation of frequency- and phase-locked waves provides several useful applications, spanning from metrology and clock distribution to short-pulse generation and coherent communications (Section 2.6).
Generating phase-locked waves is critical for phase-sensitive processing and frequency comb generation represents a straightforward solution to obtain them. The pumps and signal used to achieve the results discussed in Chapters 5 and 6 have been indeed selected from a frequency comb.
Out of several techniques well-known to provide the generation of frequency combs, phase modulation with a high modulation index has been chosen due to its simple and robust implementation [119]. Unlike approaches relying on resonant structures, mode-locked lasers or supercontinuum generation in highly nonlinear fibers (HNLFs), the use of high-modulation-index phase modulation leads to a lower number of lines. They are, however, sufficient for the applications discussed in this thesis.
The electrical field of a phase-modulated continuous wave (CW) signal can be expressed as [213]:

$$E(t) = E_0 e^{i(\Phi_0+\omega_0 t)} e^{i\pi \frac{V(t)}{V_\pi}} , \tag{B.1}$$

where E_0, Φ_0 and ω_0 are the amplitude, phase and frequency of the CW signal at the input to the phase modulator, and $V(t)$ and V_π are the driving voltage applied to the phase-modulator and its half-wave voltage, defined as the voltage required to cause a π phase-shift on the optical signal, respectively.
In the case of purely sinusoidal modulation, the driving voltage can be written as $V(t) = V_{pp}/2 \cdot \cos(\Omega t)$, being Ω the modulation frequency.

Expanding the cosine in a Fourier series, the Fourier coefficient are Bessel functions leading to a phase modulated field in the form of:

$$E(t) = E_0 e^{i(\Phi_0+\omega_0 t)} \sum_{k=-\infty}^{\infty} i^k J_k(m)\, e^{ik\Omega t}\,, \tag{B.2}$$

where J_k is a first order Bessel function of order k and m is the *modulation index* defined as:

$$m = \frac{\pi}{2}\frac{V_{pp}}{V_\pi}\,. \tag{B.3}$$

Other definitions of modulation index discard the pre-factor $\pi/2$, or consider a factor π. Throughout the thesis, however, the definition of Equation (B.3) is used.
An example of frequency comb measured for a modulation index $m \approx 4$ is shown in Fig. B.1.

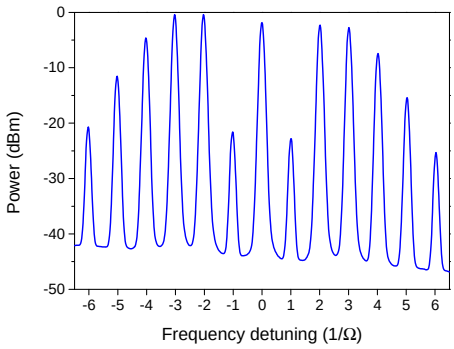

Figure B.1: Measured optical spectrum of a frequency comb generated by phase-modulating a CW laser with a sinusoidal RF signal at $\Omega = 40$ GHz and a modulation index $m \approx 4$.

Frequency combs with a similar modulation index are used in both Chapters 5 and 6.

Acronyms

A/D	analog-to-digital
APD	avalanche photodiode
ASE	amplified spontaneous emission
AWG	arbitrary waveform generator
BER	bit-error ratio
BPD	balanced photodiode
BPG	bit pattern generator
BPSK	binary phase-shift keying
CE	conversion efficiency
CW	continuous wave
DBP	digital back-propagation
DC	direct current
DCF	dispersion compensating fiber
DFG	difference frequency generation
DI	delay interferometer
DPSK	differential phase-shift keying
DSP	digital signal processing
EA	error analyzer

ECL	external cavity laser
EDFA	erbium-doped fiber amplifier
ELPF	electrical low-pass filter
EVM	error vector magnitude
FC	free carrier
FCA	free carrier absorption
FCD	free carrier dispersion
FEC	forward error correction
FOM	figure of merit
FOPA	fiber optical parametric amplifier
FWHM	full-width at half-maximum
FWM	four-wave mixing
GVD	group-velocity dispersion
HD-FEC	hard-decision FEC
HNLF	highly nonlinear fiber
IDF	inverse dispersion fiber
IR	infra red
LO	local oscillator
MNTI	mid-nonlinearity temporal inversion
MSSI	mid-span spectral inversion
MZDI	Mach-Zehnder delay interferometer
MZM	Mach-Zehnder modulator
NLSE	nonlinear Schrödinger equation
NRZ	non-return-to-zero

OBPF	optical band-pass filter
OFDM	orthogonal frequency-division multiplexing
OOK	on-off keying
OPA	optical parametric amplifier
OPC	optical phase conjugation
OSA	optical spectrum analyzer
OSNR	optical signal-to-noise ratio
OTDM	optical time-division multiplexed
PAM	pulse amplitude modulation
PBS	polarization beam splitter
PC	polarization controller
PD	photodiode
PDG	polarization-dependent gain
PDM	polarization-division multiplexing
PER	phase-sensitive extinction ratio
PM	phase modulator
PMD	polarization mode dispersion
PPLN	periodically poled lithium niobate
PRBS	pseudo-random binary sequence
PSA	phase-sensitive amplification
PZT	piezoelectric actuator
QAM	quadrature amplitude modulation
QPM	quasi-phase matching
QPSK	quadrature phase-shift keying

RF	radio frequency
RIN	relative intensity noise
RTO	real-time sampling oscilloscope
SBS	stimulated Brillouin scattering
SEM	scanning electron microscope
SFG	sum-frequency generation
SHG	second-harmonic generation
SLA	super-large-effective-area
SNR	signal-to-noise ratio
SOA	semiconductor optical amplifier
SOP	state of polarization
SPM	self-phase modulation
SRS	stimulated Raman scattering
SSMF	standard single mode fiber
TPA	two-photon absorption
VOA	variable optical attenuator
WDM	wavelength-division multiplexing
XPM	cross-phase modulation
ZDW	zero-dispersion wavelength
WSS	wavelength selective switch

Bibliography

[1] H. Takara, A. Sano, T. Kobayashi, H. Kubota, H. Kawakami, A. Matsuura, Y. Miyamoto, Y. Abe, H. Ono, K. Shikama, Y. Goto, K. Tsujikawa, Y. Sasaki, I. Ishida, K. Takenaga, S. Matsuo, K. Saitoh, M. Koshiba, and T. Morioka, "1.01-Pb/s (12 SDM/222 WDM/456 Gb/s) crosstalk-managed transmission with 91.4-b/s/Hz aggregate spectral efficiency", in *European Conference on Optical Communication, ECOC* (2012), paper Th.3.C.1.

[2] D. Qian, E. Ip, M.-F. Huang, M.-J. Li, A. Dogariu, S. Zhang, Y. Shao, Y.-K. Huang, Y. Zhang, X. Cheng, Y. Tian, P. Ji, A. Collier, Y. Geng, J. Linares, C. Montero, V. Moreno, X. Prieto, and T. Wang, "1.05 Pb/s transmission with 109 b/s/Hz spectral efficiency using hybrid single- and few-mode cores," in *Frontiers in Optics, FiO* (2012), paper FW6C.3.

[3] R.J. Mears, L. Reekie, I.M. Jauncey, and D.N. Payne, "Low-noise erbium-doped fiber amplifier operating at 1.54 μm," *Electronics Letters*, **23**, 1026–1028 (1987).

[4] P.J. Winzer, "High-spectral-efficiency optical modulation formats," *Journal of Lightwave Technology*, **30**, 3824–3835 (2012).

[5] P.J. Winzer, "Beyond 100G ethernet," *IEEE Communication Magazine*, **48**, 26–30 (2010).

[6] Cisco, "Cisco Visual Networking Index: Forecast and Methodology, 2013-2018," *Cisco Technical Report*, June 2014.

[7] R.S. Tucker and K. Hilton, "Energy consumption and energy density in optical and electronic signal processing," *IEEE Photonics Journal*, **3**, 820–833 (2011).

[8] G.W.A.T.T. (Global 'What if' Analyzer of NeTwork Energy ConsumpTion), http://gwatt.net .

[9] ITU, "Background report," *ITU Symposium on ICTs and Climate Change*, www.itu.int/ITU-T/worksem/climatechange/200907/ (2009).

[10] S. Koehl, A. Liu, and M. Paniccia, "Integrated silicon photonics: harnessing the data explosion," *Optics & Photonics News*, **22**, 24–29 (2011).

[11] B.J. Eggleton, B. Luther-Davies, and K. Richardson, "Chalcogenide photonics," *Nature Photonics*, **5**, 141–148 (2011).

[12] J. Wathen, P. Apiratikul, C. Richardson, G. Porkolab, G. Carter, and T. Murphy, "Efficient continuous-wave four-wave mixing in bandgap-engineered AlGaAs waveguides," *Optics Letters*, **39**, 3161–3164 (2014).

[13] R.H. Kingston, "Parametric amplification and oscillation at optical frequencies," in *Proceedings of the Institute of Radio Engineers*, **50**, 472 (1962).

[14] S.E. Harris, "Tunable optical parametric oscillators," *Proceedings of the IEEE*, **57**, 2096–2113 (1969).

[15] T. Torounidis, P.A. Andrekson, and B.-E. Olsson, "Fiber optical parametric amplifier with 70-dB gain," *IEEE Photonics Technology Letters*, **18**, 1194–1196 (2006).

[16] M. Jamshidifar, A. Vedadi, and M.E. Marhic, "Continuous-wave two-pump fiber optical parametric amplifier with 60 dB gain," in *Conference on Lasers and Electro-Optics, CLEO* (2014), paper JW2A.21.

[17] T. Torounidis and P.A. Andrekson, "Broadband single-pumped fiber-optic parametric amplifiers," *IEEE Photonics Technology Letters*, **19**, 650–652 (2007).

[18] J.M. Chavez Boggio, S. Moro, E. Myslivets, J.R. Windmiller, N. Alic, and S. Radic, "155-nm continuous-wave two-pump parametric amplification," *IEEE Photonics Technology Letters*, **21**, 612–614 (2009).

[19] Z. Tong, C. Lundström, P.A. Andrekson, C.J. McKinstrie, M. Karlsson, D.J. Blessing, E. Tipsuwannakul, B.J. Puttnam, H. Toda, and L. Grüner-Nielsen, "Towards ultrasensitive optical links enabled by low-noise phase-sensitive amplifiers," *Nature Photonics*, **5**, 430–436 (2011).

[20] M.E. Marhic, *Fiber Optical Parametric Amplifiers, Oscillators and Related Devices*, Cambridge University Press, 2008.

[21] J. Li, J. Hansryd, P.-O. Hedekvist, P.A. Andrekson, and S.N. Knudsen, "300 Gbit/s eye-diagram measurement by optical sampling using fiber based parametric amplification," *IEEE Photonics Technology Letters*, **13**, 987–989 (2001).

[22] Z. Lali-Dastjerdi, M. Galili, H.C. Hansen Mulvad, H. Hu, L.K. Oxenløwe, K. Rottwitt, and C. Peucheret, "Parametric amplification and phase preserving amplitude regeneration of a 640 Gbit/s RZ-DPSK signal," *Optics Express*, **21**, 25944–25953 (2013).

[23] R. Slavík, F. Parmigiani, J. Kakande, C. Lundström, M. Sjödin, P.A. Andrekson, R. Weerasuriya, S. Sygletos, A.D. Ellis, L. Grüner-Nielsen, D. Jakobsen, S. Herstrøm, R. Phelan, J. O'Gorman, A. Bogris, D. Syvridis, S. Dasgupta, P. Petropoulos, and D.J. Richardson, "All-optical phase and amplitude regenerator for next-generation telecommunications systems," *Nature Photonics*, **4**, 690–695 (2010).

[24] R. Elschner, T. Richter, and C. Schubert, "Characterization of FWM-induced crosstalk for WDM operation of a fiber-optical parametric amplifier," in *European Conference on Optical Communication, ECOC* (2011), paper Mo.1.A.2.

[25] R.P. Webb, J.M. Dailey, R.J. Manning, and A.D. Ellis, "Phase discrimination and simultaneous frequency conversion of the orthogonal components of an optical signal by four-wave mixing in an SOA," *Optics Express*, **19**, 20015–20022 (2011).

[26] G.P. Agrawal, *Nonlinear fiber optics*, Academic Press, 2007.

[27] M.E. Marhic, K.K.-Y. Wong, G. Kalogerakis, L.G. Kazovsky, "Recent advances in the design and experimental implementation of fiber optical parametric amplifiers," in *Conference on Passive Components and Fiber-based Devices, APOC* (2004), **5623**, 691–704.

[28] B.P.-P. Kuo, J.M. Fini, L. Grüner-Nielsen, and S. Radic, "Dispersion-stabilized highly-nonlinear fiber for wideband parametric mixer synthesis," *Optics Express*, **20**, 18611–18619 (2012).

[29] R. Nissim, A. Pejkic, E. Myslivets, B.P.-P. Kuo, N. Alic, and S. Radic, "Ultrafast optical control by few photons in engineered fiber," *Science*, **345**, 417–419 (2014).

[30] S. Afshar V. and T.M. Monro, "A full vectorial model for pulse propagation in emerging waveguides with subwavelength structures part I: Kerr nonlinearity," *Optics Express*, **17**, 2298–2318 (2009).

[31] J. Hansryd, P.A. Andrekson, M. Westlund, J. Li, and P.-O. Hedekvist, "Fiber-based optical parametric amplifiers and their applications", *IEEE Journal of Selected Topics in Quantum Electronics*, **8**, 506–520 (2002).

[32] G. Banfi, I. Cristiani, and V. Degiorgio, " Wavelength shifting by cascaded second-order processes," *Journal of Optics A: Pure and Applied Optics*, **2**, 260–267 (2000).

[33] G.P. Agrawal, *Fiber Optic Communication Systems*, Academic Press, 2010.

[34] M.J. Weber, *Handbook of Optical Materials*, CRC Press, 2004.

[35] Q. Lin, J. Zhang, G. Piredda, R.W. Boyd, P.M. Fauchet, and G.P. Agrawal, "Dispersion of silicon nonlinearities in the near infrared region," *Applied Physics Letters*, **91**, 021111 (2007).

[36] Q. Lin, O.J. Painter, and G.P. Agrawal, "Nonlinear optical phenomena in silicon waveguides: Modeling and applications," *Optics Express*, **15**, 16660–16644 (2007).

[37] A.C. Turner-Foster, M.A. Foster, J.S. Levy, C.B. Poitras, R. Salem, A.L. Gaeta, and M. Lipson, "Ultrashort free-carrier lifetime in low-loss silicon nanowaveguides," *Optics Express*, **18**, 3582–3591 (2010).

[38] A. Kobyakov, M. Sauer, and D. Chowdhury, "Stimulated Brillouin scattering in optical fibers," *Advances in Optics and Photonics*, **2**, 1–59 (2010).

[39] B.J. Eggleton, C.G. Poulton, and R. Pant, "Inducing and harnessing stimulated Brillouin scattering in photonic integrated circuits," *Advances in Optics and Photonics*, **5**, 536–587 (2013).

[40] I.P Kaminow, T. Li, A.E Wilner, *Optical Fiber Telecommunications VIA, Components and Subsystems*, Academic Press, 2013.

[41] A. David and M. Horowitz, "Low-frequency transmitted intensity noise induced by stimulated Brillouin scattering in optical fibers," *Optics Express*, **19**, 11792–11803 (2011).

[42] S. Roy, S.K. Bhadra, and G.P. Agrawal, "Raman amplification of optical pulses in silicon waveguides: effects of finite gain bandwidth, pulse width, and chirp," *Journal of the Optical Society of America B*, **26**, 17–25 (2009).

[43] S.-K. Choi, R.-D. Li, C. Kim, and P. Kumar, "Traveling-wave optical parametric amplifier: Investigation of its phase-sensitive and phase-insensitive gain response," *Journal of the Optical Society of America B*, **14**, 1564–1575 (1997).

[44] C.J. McKinstrie and S. Radic, "Phase-sensitive amplification in a fiber," *Optics Express*, **12**, 4973–4979 (2004).

[45] M. Vasilyev, "Distributed phase-sensitive amplification," *Optics Express*, **13**, 7563–7571 (2005).

[46] C. Lundström, Z. Tong, M. Karlsson, and P.A. Andrekson, "Phase-to-phase and phase-to-amplitude transfer characteristics of a nondegenerate-idler phase-sensitive amplifier," *Optics Letters*, **36**, 4356–4358 (2011).

[47] Z. Tong, C. Lundström, M. Karlsson, M. Vasilyev, and P.A. Andrekson, "Noise performance of a frequency nondegenerate phase-sensitive amplifier with unequalized inputs," *Optics Letters*, **36**, 722–724 (2011).

[48] T. Nakanishi, M. Tanaka, T. Hasegawa, M. Hirano, T. Okuno, and M. Onishi, "Al2O3-SiO2 core highly nonlinear dispersion-shifted fiber with Brillouin gain suppression improved by 6.1 dB," in *European Conference on Optical Communication, ECOC* (2005), paper Th4.2.2.

[49] M.-J. Li, X. Chen, J. Wang, S. Gray, A. Liu, J.A. Demeritt, A.B. Ruffin, A.M. Crowley, D.T. Walton, and L.A. Zenteno, "AlGe co-doped large mode area fiber with high SBS threshold," *Optics Letters*, **15**, 8290–8299 (2007).

[50] M.D. Mermelstein, "SBS threshold measurements and acoustic beam propagation modeling in guiding and anti-guiding single mode optical fibers," *Optics Letters*, **17**, 16225–16237 (2009).

[51] L. Grüner-Nielsen, S. Dasgupta, M.D. Mermelstein, D. Jakobsen, S. Herstrøm, M.E. Pedersen, E. Lim, S. Alam, F. Parmigiani, D.J. Richardson, and B. Pálsdóttir, "A silica based highly nonlinear fibre with improved threshold for stimulated Brillouin scattering," in *European Conference on Optical Communication, ECOC* (2010), paper Tu.4.D.3.

[52] http://fiber-optic-catalog.ofsoptics.com/item/optical--fibers/highly-nonlinear-fiber-optical-fibers1/hnlf-al-doped.

[53] R. Slavík, J. Kakande, F. Parmigiani, P. Petropoulos, and D.J. Richardson, "All-optical regeneration based on phase sensitive amplification," in *Conference on Lasers and Electro-Optics, CLEO* (2011), paper CWD2.

[54] S.L.I. Olsson, B. Corcoran, C. Lundström, E. Tipsuwannakul, S. Sygletos, A.D. Ellis, Z. Tong, M. Karlsson, and P.A. Andrekson, "Injection locking-based pump recovery for phase-sensitive amplified links," *Optics Express*, **21**, 14512–14529 (2013).

[55] T. Richter, R. Elschner, and C. Schubert, "QAM phase-regeneration in a phase-sensitive fiber-amplifier," in *European Conference on Optical Communication, ECOC* (2013), paper We.3.A.2.

[56] J. Hansryd, F. Dross, M. Westlund, P.A. Andrekson, and S.N. Knudsen, "Increase of the SBS threshold in a short highly nonlinear fiber by applying a temperature distribution," *Journal of Lightwave Technology*, **19**, 1691–1697 (2001).

[57] J.D. Marconi, J.M. Chavez Boggio, F.A. Callegari, A. Guimarães, R. Arradi, and H.L. Fragnito, "Double-pumped parametric amplifier with strained fibre to suppress SBS," *Electronics Letters*, **40**, 1–2 (2004).

[58] J.M. Chavez Boggio, J.D. Marconi, and H.L. Fragnito, "Experimental and numerical investigation of the SBS-threshold increase in an optical fiber by applying strain distributions," *Journal of Lightwave Technology*, **23**, 3808–3814 (2005).

[59] C. Lundström, E. Myslivets, A.O.J. Wiberg, N. Alic, S. Radic, M. Karlsson, and P.A. Andrekson, "Tension-optimized highly nonlinear fiber for parametric applications," in *European Conference on Optical Communication, ECOC* (2012), paper We.1.F.2.

[60] C. Lundström, R. Malik, L. Grüner-Nielsen, B. Corcoran, S.L.I. Olsson, M. Karlsson, and P.A. Andrekson, "Fiber optic parametric amplifier with 10-dB net gain without pump dithering," *IEEE Photonics Technology Letters*, **25**, 234–237 (2013).

[61] E. Myslivets, C. Lundström, J. Aparicio, S. Moro, A.O.J. Wiberg, C.-S. Brès, N. Alic, P.A. Andrekson, and S. Radic, "Spatial equalization of zero-dispersion wavelength profiles in nonlinear fibers," *IEEE Photonics Technology Letters*, **21**, 1807–1809 (2009).

[62] M. Takahashi, M. Tadakuma, and T. Yagi, "Dispersion and Brillouin managed HNLFs by strain control techniques," *Journal of Lightwave Technology*, **28**, 59–64 (2010).

[63] B.P.-P. Kuo and S. Radic, "Highly nonlinear fiber with dispersive characteristic invariant to fabrication fluctuations," *Optics Express*, **20**, 7716–7725 (2012).

[64] B.P.-P. Kuo, J.M. Fini, L. Grüner-Nielsen, and S. Radic, "Dispersion-stabilized highly-nonlinear fiber for wideband parametric mixer synthesis," *Optics Express*, **20**, 18611–18619 (2012).

[65] Y. Takushima and T. Okoshi, "Suppression of stimulated Brillouin scattering using isolators," in *Optical Fiber Communication Conference, OFC* (1992), paper WM6.

[66] K.K.-Y. Wong, K. Shimizu, K. Uesaka, G. Kalogerakis, M.E. Marhic, and L.G. Kazovsky, "Continuous-wave fiber optical parametric amplifier with 60-dB gain using a novel two-segment design," *IEEE Photonics Technology Letters*, **15**, 1707–1709 (2003).

[67] S.K. Korotky, P.B. Hanse, L. Eskildsen, and J.J. Veselka, "Efficient phase modulation scheme for suppressing stimulated Brillouin scattering," in *Integrated Optics and Optical Fiber Communications, IOOC* (1995), paper WD2.

[68] A. Mussot, M. Le Parquier, and P. Szriftgiser, "Thermal noise for SBS suppression in fiber optical parametric amplifiers," *Optics Communications*, **283**, 2607–2610 (2010).

[69] J.B. Coles, B.P.-P. Kuo, N. Alic, S. Moro, C.-S. Brès, J.M. Chavez Boggio, P.A. Andrekson, M. Karlsson, and S. Radic, "Bandwidth-efficient phase modulation techniques for stimulated Brillouin scattering suppression in fiber optic parametric amplifiers," *Optics Express*, **18**, 18138–18150 (2010).

[70] A. Durécu-Legrand, A. Mussot, C. Simonneau, D. Bayart, T. Sylvestre, E. Lantz, and H. Maillotte, "Impact of pump phase modulation on system performance of fibre-optical parametric amplifiers," *Electronics Letters*, **17**, 1–2 (2005).

[71] R. Elschner, *Parametric Amplification and Wavelength Conversion of Phase-Modulated Signals*, Ph.D. thesis, Technische Universität Berlin, Berlin, Germany, 2011.

[72] J.M. Chavez Boggio, F.A. Callegari, A. Guimaraes, J.D. Marconi, and H.L. Fragnito, "Q Penalties due to pump phase modulation in FOPAs," in *Optical Fiber Communication Conference, OFC* (2005), paper OWN4.

[73] M.-C. Ho, M.E. Marhic, K.Y.K. Wong, and L.G. Kazovsky, "Narrow-linewidth idler generation in fiber four-wave mixing and parametric amplification by dithering two pumps in opposition of phase," *Journal of Lightwave Technology*, **20**, 469–476 (2002).

[74] R. Elschner, C.-A. Bunge, B. Hüttl, A. Gual i Coca, C. Schmidt-Langhorst, R. Ludwig, C. Schubert, and K. Petermann, "Impact of pump-phase modulation on FWM-based wavelength conversion of D(Q)PSK signals," *IEEE Journal of Selected Topics in Quantum Electronics*, **14**, 666–673 (2008).

[75] T. Richter, R. Elschner, A. Gandhe, K. Petermann, and C. Schuber, "Parametric amplification and wavelength conversion of single- and dual-polarization DQPSK signals," *IEEE Journal of Selected Topics in Quantum Electronics*, **18**, 988–995 (2012).

[76] J. Kakande, R. Slavík, F. Parmigiani, P. Petropoulos, and D.J. Richardson, "Synthesis of phase-locked counter-phase modulated pumps for SBS-suppressed fiber parametric amplifiers," in *Conference on Lasers and Electro-Optics, CLEO* (2010), paper CFN4.

[77] R. Elschner, C.A. Bunge, and K. Petermann, "Co- and counterphasing tolerances for dual-pump parametric λ-conversion of D(Q)PSK signals," *IEEE Photonics Technology Letters*, **21**, 706–708 (2009).

[78] S. Radic, C.J. McKinstrie, R.M. Jopson, J.C. Centanni, A.R. Chraplyvy, C.G. Jorgensen, K. Brar, and C. Headley, "Selective suppression of idler spectral broadening in two-pump parametric architectures," *IEEE Photonics Technology Letters*, **15**, 673–675 (2003).

[79] A.P. Anthur, R.T. Watts, K. Shi, J.O. Carroll, D. Venkitesh and L.P. Barry, "Dual correlated pumping scheme for phase noise preservation in all-optical wavelength conversion," *Optics Express*, **12**, 15568–15579 (2013).

[80] N.E. Dahdah, D.S. Govan, M. Jamshidifar, N.J. Doran, and M.E. Marhic, "Fiber optical parametric amplifier performance in a 1-Tb/s DWDM communication system," *IEEE Journal of Selected Topics in Quantum Electronics*, **18**, 950–957 (2012).

[81] X. Liu, R.M. Osgood Jr., Y.A. Vlasov, and W.M.J. Green, "Mid-infrared optical parametric amplifier using silicon nanophotonic waveguides," *Nature Photonics*, **4**, 557–560 (2010).

[82] F. Gholami, B.P.-P. Kuo, S. Zlatanovic, N. Alic, and S. Radic, "Phase-preserving parametric wavelength conversion to SWIR band in highly nonlinear dispersion stabilized fiber," *Optics Express*, **21**, 11415–11424 (2013).

[83] A. Yariv, D. Fekete, and D.M. Pepper, "Compensation for channel dispersion by nonlinear optical phase conjugation," *Optics Letters*, **4**, 52–54 (1979).

[84] H. Rong, S. Ayotte, W. Mathlouthi, and M. Paniccia, "Mid-span dispersion compensation via optical phase conjugation in silicon waveguides," in *Optical Fiber Communication Conference, OFC* (2008), paper OWP2.

[85] S. Watanabe and T. Chikam, "Cancellation of four-wave mixing in multichannel fibre transmission by midway optical phase conjugation," *Electronics Letters*, **30**, 1156–1557 (1994).

[86] S.L. Jansen, D. van den Borne, C. Climent Monsalve, S. Spälter, P.M. Krummrich, G.D. Khoe, and H. de Waardt, "Reduction of Gordon-Mollenauer phase noise by midlink spectral inversion," *IEEE Photonics Technology Letters*, **17**, 923–925 (2005).

[87] B.P.-P. Kuo, E. Myslivets, N. Alic, and S. Radic, "Wavelength multicasting via frequency comb generation in a bandwidth-enhanced fiber optical parametric mixer," *Journal of Lightwave Technology*, **29**, 3515–3522 (2011).

[88] K. Inoue, "Optical level equalisation based on gain saturation in fibre optical parametric amplifier," *Electronics Letters*, **36**, 1016–1017 (2000).

[89] A. Bogoni, X. Wu, S.R. Nuccio, and A.E. Willner, "640 Gb/s all-optical regenerator based on a periodically poled lithium niobate waveguide," *Journal of Lightwave Technology*, **30**, 1829–1834 (2012).

[90] C. Peucheret, M. Lorenzen, J. Seoane, D. Noordegraaf, C.V. Nielsen, L. Grüner-Nielsen, and K. Rottwitt,"Amplitude regeneration of RZ-DPSK signals in single-pump fiber-optic parametric amplifiers," *IEEE Photonics Technology Letters*, **21**, 872–874 (2009).

[91] T. Richter, R. Ludwig, J.K. Fischer, S. Watanabe, R. Okabe, T. Kato, and C. Schubert, "All-optical level equalization of data packets using a fiber-optic parametric amplifier," in *European Conference on Optical Communication, ECOC* (2010), paper We.8.A.7.

[92] H.C. Hansen Mulvad, M. Galili, L. Grüner-Nielsen, L.K. Oxenløwe, A.T. Clausen, and P. Jeppesen, "640 Gbit/s time-division add-drop multiplexing using a non-linear polarisation-rotating fibre loop," in *European Conference on Optical Communication, ECOC* (2008), paper Tu.3.D.6.

[93] T. Morioka and M. Saruwatari, "Ultrafast all-optical switching utilizing the optical Kerr effect in polarization-maintaining single-mode fibers," *IEEE Journal of Selected Areas in Communications*, **6**, 1186–1198 (1988).

[94] A.O.J. Wiberg, B.P.-P. Kuo, C.-S. Brès, N. Alic, and S. Radic, "640-Gb/s transmitter and self-tracked demultiplexing receiver using single parametric gate," *IEEE Photonics Technology Letters*, **23**, 507–509 (2011).

[95] M. Westlund, P.A. Andrekson, H. Sunnerud, J. Hansryd, and J. Li, "High-performance optical-fiber-nonlinearity-based optical waveform monitoring," *Journal of Lightwave Technology*, **23**, 2012–2022 (2005).

[96] H. Ohta, S. Nogiwa, Y. Kawaguchi, and Y. Endo, "Measurement of 200 Gbit/s optical eye diagram by optical sampling with gain switched optical pulse," *Electronics Letters*, **36**, 737–739 (2000).

[97] C. Lundström, *Phase-Sensitive Fiber Optic Parametric Amplifiers and Their Applications in Optical Communication*, Ph.D. thesis, Chalmers Univerisity of Technology, Göteborg, Sweden, 2012.

[98] J.A. Levenson, I. Abram, T. Rivera, and P. Grangier, "Reduction of quantum noise in optical parametric amplification," *Journal of the Optical Society of America B*, **10**, 2233–2238 (1993).

[99] Z. Tong, C.J. McKinstrie, C. Lundström, M. Karlsson, and P.A. Andrekson, "Noise performance of optical fiber transmission links that use non-degenerate cascaded phase-sensitive amplifiers," *Optics Express*, **18**, 15426–15439 (2010).

[100] T. Umeki, M. Asobe, H. Takara, Y. Miyamoto, and H. Takenouchi, "Multi-span transmission using phase and amplitude regeneration in PPLN-based PSA," *Optics Express*, **21**, 18170–18177 (2013).

[101] R. Tang, J. Lasri, P.S. Devgan, V.S. Grigoryan, P. Kumar, and M. Vasilyev, "Gain characteristics of a frequency nondegenerate phase-sensitive fiber-optic parametric amplifier with phase self-stabilized input," *Optics Express*, **13**, 10483–10493 (2005).

[102] R. Tang, P.S. Devgan, V.S. Grigoryan, P. Kumar, and M. Vasilyev, "In-line phase-sensitive amplification of multi-channel CW signals based on frequency nondegenerate four-wave-mixing in fiber," *Optics Express*, **16**, 9046–9053 (2008).

[103] B. Corcoran, S.L.I. Olsson, C. Lundström, M. Karlsson, and P.A. Andrekson, "Phase-sensitive optical pre-amplifier implemented in an 80km DQPSK link," in *Optical Fiber Communication Conference, OFC* (2012), paper PDP5A.4.

[104] S.L.I. Olsson, T.A. Eriksson, C. Lundström, M. Karlsson, and P.A. Andrekson, "Linear and nonlinear transmission of 16-QAM over 105 km phase-sensitive amplified link," in *Optical Fiber Communication Conference, OFC* (2014), paper Th1H.3.

[105] S.L.I. Olsson, C. Lundström, M. Karlsson, and P.A. Andrekson, "Long-Haul (3465 km) Transmission of a 10 GBd QPSK Signal with Low Noise Phase-Sensitive In-Line Amplification," in *European Conference on Optical Communication, ECOC* (2014), paper PD.2.2.

[106] K.A. Croussore, C. Kim, and G. Li, "All-optical regeneration of differential phase-shift keying signals based on phase-sensitive amplification," *Optics Letters*, **29**, 2357–2359 (2004).

[107] C. Lundström, B.J. Puttnam, Z. Tong, M. Karlsson, and P.A. Andrekson, "Experimental characterization of the phase squeezing properties of a phase-sensitive parametric amplifier in non-degenerate idler configuration," in *European Conference on Optical Communication, ECOC* (2010), paper Th.10.C.1.

[108] A. Albuquerque, B.J. Puttnam, M. Drummond, Á. Szabó, D. Mazroa, S. Shinada, N. Wada, and R. Nogueira, "Phase-sensitive amplification in a single bi-directional PPLN waveguide," *Optics Express*, **21**, 22063–22069 (2013).

[109] R. Slavík, J. Kakande, F. Parmigiani, L. Grüner-Nielsen, D. Jakobsen, S. Herstrøm, P. Petropoulos, and D.J. Richardson, "All-optical phase-regenerative multicasting of 40 Gbit/s DPSK signal in a degenerate phase sensitive amplifier," in *European Conference on Optical Communication, ECOC* (2010), paper Mo.1.A.2.

[110] P. Frascella, S. Sygletos, F. Gunning, R. Weerasuriya, L. Grüner-Nielsen, R. Phelan, J. O'Gorman, and A.D. Ellis, "DPSK signal regeneration with a dual-pump nondegenerate phase-sensitive amplifier," *IEEE Photonics Technology Letters*, **23**, 516–518 (2011).

[111] S. Sygletos, M.J. Power, F.C. Garcia Gunning, R.P. Webb, R.J. Manning, and A.D. Ellis, "Simultaneous dual channel phase regeneration in SOAs", in *European Conference on Optical Communication, ECOC* (2012), paper Tu.1.A.2.

[112] S. Sygletos, M.E. McCarthy, S.J. Fabbri, M. Sorokina, M.F.C. Stephens, I.D. Phillips, E. Giacoumidis, N. Mac Suibhne, P. Harper, N.J. Doran, S.K. Turitsyn, and A.D. Ellis, "Multichannel regeneration of dual quadrature signals", in *European Conference on Optical Communication, ECOC* (2014), paper P.3.13.

[113] J. Kakande, R. Slavík, F. Parmigiani, A. Bogris, D. Syvridis, L. Grüner-Nielsen, R. Phelan, P. Petropoulos, and D.J. Richardson, "Multilevel quantization of optical phase in a novel coherent parametric mixer architecture," *Nature Photonics*, **5**, 748–752 (2011).

[114] J. Kakande, A. Bogris, R. Slavík, F. Parmigiani, D. Syvridis, P. Petropoulos, and D.J. Richardson, "First demonstration of all-optical QPSK signal regeneration in a novel multi-format phase sensitive amplifier," in *European Conference on Optical Communication, ECOC* (2010), paper PD3.3.

[115] J. Kakande, A. Bogris, R. Slavík, F. Parmigiani, D. Syvridis, P. Petropoulos, D.J. Richardson, M. Westlund, and M. Sköld, "QPSK phase and amplitude regeneration at 56 Gbaud in a novel idler-free non-degenerate phase sensitive amplifier," in *Optical Fiber Communication Conference, OFC* (2011), paper OMT4.

[116] K.R.H. Bottrill, G. Hesketh, F. Parmigiani, P. Horak, D.J. Richardson, and P. Petropoulos, "An optical phase quantiser exhibiting suppressed phase dependent gain variation," in *Optical Fiber Communication Conference, OFC* (2014), paper W3F.7.

[117] M. Gao, T. Kurosu, T. Inoue, and S. Namiki, "Low-penalty phase de-multiplexing of QPSK signal by dual pump phase sensitive amplifiers," in *European Conference on Optical Communication, ECOC* (2013), paper We.3.A.5.

[118] J. Pfeifle, V. Brasch, M. Lauermann, Y. Yu, D. Wegner, T. Herr, K. Hartinger, P. Schindler, J. Li, D. Hillerkuss, R. Schmogrow, C. Weimann, R. Holzwarth, W. Freude, J. Leuthold, T.J. Kippenberg, and C. Koos, "Coherent terabit communications with microresonator Kerr frequency combs," *Nature Photonics*, **8**, 375–380 (2014).

[119] V. Torres-Company and A.M. Weiner, "Optical frequency comb technology for ultra-broadband radio-frequency photonics," *Laser Photonics Review*, **8**, 368–393 (2014).

[120] R. Slavík, J. Kakande, P. Petropoulos, and D.J. Richardson, "Processing of optical combs with fiber optic parametric amplifiers," *Optics Express*, **20**, 10059–10070 (2012).

[121] P.J. Winzer, A.H. Gnauck, C.R. Doerr, M. Magarini, and L.L. Buhl, "Spectrally efficient long-haul optical networking using 112-Gb/s polarization-multiplexed 16-QAM," *Journal of Lightwave Technology*, **28**, 547–556 (2010).

[122] S. Savory, "Digital coherent optical receivers: algorithms and subsystems," *IEEE Journal of Selected Topics in Quantum Electronics*, **16**, 1164-1179 (2010).

[123] M. Jazayerifar, S. Warm, R. Elschner, D. Kroushkov, I. Sackey, C. Meuer, C. Schubert, and K. Petermann, "Performance evaluation of DWDM communication systems with fiber optical parametric amplifiers," *Journal of Lightwave Technology*, **31**, 1454–1461 (2013).

[124] I. Sackey, R. Elschner, M. Nölle, T. Richter, L. Molle, C. Meuer, M. Jazayerifar, S. Warm, K. Petermann, and C. Schubert, "Characterization of a fiber-optical parametric amplifier in a 5×28-GBd 16-QAM DWDM system," in *Optical Fiber Communication Conference, OFC* (2014), paper W3E.3.

[125] Z. Tong, A. Bogris, M. Karlsson, and P.A. Andrekson, "Full characterization of the signal and idler noise figure spectra in single-pumped fiber optical parametric amplifiers," *Electronics Letters*, **18**, 2884–2893 (2010).

[126] V. Cristofori, Z. Lali-Dastjerdi, T. Lund-Hansen, C. Peucheret, and K. Rottwitt, "Experimental investigation of saturation effect on pump-to-signal intensity modulation transfer in single-pump phase-insensitive fiber optic parametric amplifiers," *Journal of the Optical Society of America B*, **30**, 884–888 (2013).

[127] K. Inoue and T. Mukai, "Experimental study on noise characteristics of a gain-saturated fiber optical parametric amplifier," *Journal of Lightwave Technology*, **20**, 969–974 (2002).

[128] R. Elschner and K. Petermann, "BER performance of 16-QAM signals amplified by dual-pump fiber optical parametric amplifiers," in *Optical Fiber Communication Conference, OFC* (2010), paper OThA4.

[129] R. Elschner, T. Richter, M. Nölle, J. Hilt, and C. Schubert, "Parametric amplification of 28-GBd NRZ-16QAM signals," in *Optical Fiber Communication Conference, OFC* (2011), paper OThC2.

[130] I. Fatadin, D. Iver, and S. Savory, "Laser linewidth tolerance for 16-QAM coherent optical systems using QPSK partitioning," *IEEE Photonics Technology Letters*, **22**, 631–633 (2010).

[131] Z. Lali-Dastjerdi, K. Rottwitt, M. Galili, and C. Peucheret "Asymmetric gain-saturated spectrum in fiber optical parametric amplifiers," *Optics Express*, **20**, 15530–15539 (2012).

[132] R. Schmogrow, B. Nebendahl, M. Winter, A. Josten, D. Hillerkuss, S. Koenig, J. Meyer, M. Dreschmann, M. Huebner, C. Koos, J. Becker, W. Freude, and J. Leuthol, "Error vector magnitude as a performance measure for advanced modulation formats," *IEEE Photonics Technology Letters*, **24**, 61–63 (2012).

[133] G.-W. Lu, T. Sakamoto, and T. Kawanishi, "Wavelength conversion of optical 64QAM through FWM in HNLF and its performance optimization by constellation monitoring," *Optics Express*, **22**, 15–22 (2014).

[134] A.R. Chraplyvy, "Limitations on lightwave communications imposed by optical-fiber nonlinearities," *Journal of Lightwave Technology*, **8**, 1548–1557 (1990).

[135] A.D. Ellis, J. Zhao, and D. Cotter, "Approaching the non-linear Shannon limit," *Journal of Lightwave Technology*, **28**, 423–433 (2010).

[136] X. Li, F. Zhang, Z. Chen, and A. Xu, "Suppression of XPM and XPM-induced nonlinear phase noise for RZ-DPSK signals in 40 Gbit/s WDM transmission systems with optimum dispersion mapping," *Optics Express*, **15**, 18247–18252 (2007).

[137] L.B. Du and A.J. Lowery, "Fiber nonlinearity compensation for CO-OFDM systems with periodic dispersion maps," in *Optical Fiber Communication Conference, OFC* (2009), paper OTuO1.

[138] E. Mateo, L. Zhu, G. Li, "Impact of XPM and FWM on the digital implementation of impairment compensation for WDM transmission using backward propagation," *Optics Express*, **16**, 16124–16137 (2008).

[139] D. Rafique, J. Zhao, and A.D. Ellis, "Digital back-propagation for spectrally efficient WDM 112 Gbit/s PM m-ary QAM transmission," *Optics Express*, **19**, 5219–5224 (2011).

[140] C. Xia, X. Liu, S. Chandrasekhar, N.K. Fontaine, L. Zhu, and G. Li, "Multi-channel nonlinearity compensation of PDM-QPSK signals in dispersion-managed transmission using dispersion-folded digital backward propagation," *Optics Express*, **22**, 5859–5866 (2014).

[141] S. Savory, G. Gavioli, E. Torrengo, and P. Poggiolini, "Impact of interchannel nonlinearities on a split-step intrachannel nonlinear equalizer," *IEEE Photonics Technology Letters*, **22**, 673–675 (2004).

[142] D. Rafique, M. Mussolin, J. Mårtensson, M. Forzati, J.K. Fischer, L. Molle, M. Nölle, C. Schubert, and A.D. Ellis, "Polarization multiplexed 16QAM transmission employing modified digital backpropagation," *Optics Express*, **19**, 805–810 (2011).

[143] E. Ip, P. Ji, E. Mateo, Y.-K. Huang, L. Xu, D. Qian, N. Bai, and T. Wang, "100G and beyond transmission technologies for evolving optical networks and relevant physical-layer issues," *Proceedings of the IEEE*, **100**, 1065—1078 (2012).

[144] R. Asif, C.-Y. Lin, M. Holtmannspötter, and B. Schmauss, "Evaluation of correlative coding and DP-16QAM n-channel 112Gbit/s coherent transmission: digital non-linear compensation perspective," *Optics Express*, **21**, 781–788 (2013).

[145] R. Maher, L. Galdino, M. Sato, T. Xu, K. Shi, S. Kilmurray, S.J. Savory, B.C. Thomsen, R.I. Killey, and P. Bayvel, "Linear and nonlinear impairment mitigation in a Nyquist spaced DP-16QAM WDM transmission system with full-field DBP ," in *European Conference on Optical Communication, ECOC* (2014), P.5.10.

[146] I. Brener, B. Mikkelsen, K. Rottwitt, W. Burkett, G. Raybon, J.B. Stark, K. Parameswaran, M.H. Chou, M.M. Fejer, E.E. Chaban, R. Harel, D.L. Philen, and S. Kosinski, "Cancellation of all Kerr nonlinearities in long fiber spans using a LiNbo3 phase conjugator and Raman amplification," in *Optical Fiber Communication Conference, OFC* (2000), paper PD33-1.

[147] P. Kaewplung and K. Kikuchi, "Simultaneous cancellation of fiber loss, dispersion, and Kerr effect in ultralong-haul optical fiber transmission by midway optical phase conjugation incorporated with distributed Raman amplification," *Journal of Lightwave Technology*, **25**, 3035–3050 (2007).

[148] D.M. Pepper and A. Yariv, "Compensation for phase distortions in nonlinear media by phase conjugation," *Optics Letters*, **5**, 59–60 (1980).

[149] S. Watanabe, T. Chikama, G. Ishikawa, T. Terahara, and H. Kuwahara, "Compensation of pulse shape distortion due to chromatic dispersion and Kerr effect by optical phase conjugation," *IEEE Photonics Technology Letters*, **5**, 1241–1243 (1993).

[150] W. Pieper, C. Kurtzke, R. Schnabel, D. Breuer, R. Ludwig, K. Petermann, and H.G. Weber, "Nonlinearity-insensitive standard-fibre transmission based on optical-phase conjugation in a semiconductor-laser amplifier," *Electronics Letters*, **30**, 724-726 (1994).

[151] S. Watanabe and M. Shirasaki, "Exact compensation for both chromatic dispersion and Kerr effect in a transmission fiber using optical phase conjugation," *Journal of Lightwave Technology*, **14**, 243–248 (1996).

[152] H. Wei and D.V. Plant, "Simultaneous nonlinearity suppression and wide-band dispersion compensation using optical phase conjugation," *Optics Express*, **12**, 1938–1958 (2004).

[153] M.F. Stephens, M. Tan, I. Phillips, S. Sygletos, P. Harper, and N.J. Doran, "1THz-bandwidth polarization-diverse optical phase conjugation of 10x114Gb/s DP-QPSK WDM signals," in *Optical Fiber Communication Conference, OFC* (2014), paper W3F.6.

[154] K. Solis-Trapala, T. Inoue, and S.Namiki, "Nearly-ideal optical phase conjugation based nonlinear compensation system," in *Optical Fiber Communication Conference, OFC* (2014), paper W3F.8.

[155] A. Chowdhury, G. Raybon, R.-J. Essiambre, J.H. Sinsky, A. Adamiecki, J. Leuthold, C.R. Doerr, and S. Chandrasekhar, "Compensation of intrachannel nonlinearities in 40-Gb/s pseudolinear systems using optical-phase conjugation," *Journal of Lightwave Technology*, **23**, 172–177 (2005).

[156] P. Minzioni, "Nonlinearity compensation in a fiber-optic link by optical phase conjugation," *Fiber and Integrated Optics*, **28**, 179–209 (2009).

[157] P. Minzioni, F. Alberti, and A. Schiffini, "Techniques for nonlinearity cancellation into embedded links by optical phase conjugation," *Journal of Lightwave Technology*, **23**, 2364–2370 (2005).

[158] H. Hu, R.M. Jopson, A. Gnauck, M. Dinu, S. Chandrasekhar, X. Liu, C. Xie, M. Montoliu, S. Randel, and C.J. McKinstrie, "Fiber nonlinearity compensation of an 8-channel WDM PDM-QPSK signal using multiple phase conjugations," in *Optical Fiber Communication Conference, OFC* (2014), paper M3C.2.

[159] L.B. Du, M. Monir Morshed, and A.J. Lowery, "Fiber nonlinearity compensation for OFDM super-channels using optical phase conjugation," *Optics Express*, **20**, 19921–19927 (2012).

[160] X. Liu, A.R. Chraplyvy, P.J. Winzer, R.W. Tkach, and S. Chandrasekhar, "Phase-conjugated twin waves for communication beyond the Kerr nonlinearity limit," *Nature Photonics*, **7**, 560–568 (2013).

[161] H. Eliasson, S.L.I. Olsson, M. Karlsson, and P.A. Andrekson, "Comparison between coherent superposition in DSP and PSA for mitigation of nonlinearities in a single-span link," in *European Conference on Optical Communication, ECOC* (2014),paper Mo.3.5.2.

[162] N. Alic, E. Myslivets, E. Temprana, B.P.-P. Kuo, and S. Radic, "Nonlinearity cancellation in fiber optic links based on frequency referenced carriers," *Journal of Lightwave Technology*, **32**, 2690–2698 (2014).

[163] K.K.-Y. Wong, M.E. Marhic, K. Uesaka, and L.G. Kazovsky, "Polarization-independent two-pump fiber optical parametric amplifier," *IEEE Photonics Technology Letters*, **14**, 911–913 (2002).

[164] M. Jazayerifar, I. Sackey, R. Elschner, S. Warm, C. Meuer, C. Schubert, and K. Petermann, "Impact of SBS on polarization-insensitive single-pump optical parametric amplifiers based on a diversity loop scheme," in *European Conference on Optical Communication, ECOC* (2014), Tu.4.6.4.

[165] S.K. Ibrahim, J. Zhao, F.C.G. Gunning, P. Frascella, F.H. Peters, and A.D. Ellis, "Towards a practical implementation of coherent WDM: analytical, numerical, and experimental studies," *IEEE Photonics Journal*, **2**, 833–847 (2010).

[166] L.B. Du and A.J. Lowery, "Experimental investigation of the effect of using 'Odd and Even' channels in all-optical OFDM and Nyquist WDM system comparisons," in *European Conference on Optical Communication, ECOC* (2012), paper Tu.4.C.5.

[167] M. Tan, P. Rosa, I.D. Phillips, M.F.C. Stephens, S. Sygletos, A.D. Ellis, and P. Harper, "Transmission comparison of ultra-long Raman fibre laser based amplification with first and dual order Raman amplification using 10×118 Gbit/s DP-QPSK," in *International Conference on Transparent Optical Networks, ICTON* (2014), paper Tu.C1.7.

[168] A. Gumaste and T. Antony, *DWDM Network Designs and Engineering Solutions* Cisco Press, 2002.

[169] M.N. Islam, *Raman Amplifiers for Telecommunications 2: Sub-Systems and Systems,* Springer, 2004.

[170] J.M. Chavez Boggio, S. Zlatanovic, F. Gholami, J.M. Aparicio, S. Moro, K. Balch, N. Alic, and S. Radic, "Short wavelength infrared frequency conversion in ultra-compact fiber device," *Optics Express*, **18**, 439–445 (2010).

[171] K.J. Lee, F. Parmigiani, S. Liu, J. Kakande, P. Petropoulos, K. Gallo, and D.J. Richardson, "Phase sensitive amplification based on quadratic cascading in a periodically poled lithium niobate waveguide," *Optics Express*, **17**, 20393–20400 (2009).

[172] B.J. Puttnam, D. Mazroa, S. Shinada, and N. Wada, "Large phase sensitive gain in periodically poled lithium niobate with high pump power," *IEEE Photonics Technology Letters*, **23**, 426–428 (2011).

[173] T. Umeki, M. Asobe, and H. Takenouchi, "In-line phase sensitive amplifier based on PPLN waveguides," *Optics Express*, **21**, 12077–12084 (2013).

[174] R. Neo, J. Schröder, Y. Paquot, D-Y. Choi, S. Madden, B. Luther-Davies, and B.J. Eggleton, "Phase-sensitive amplification of light in a $\chi^{(3)}$ photonic chip using a dispersion engineered chalcogenide ridge waveguide," *Optics Express*, **21**, 7926–7933 (2013).

[175] N. Kang, A. Fadil, M. Pu, H. Ji, H. Hu, E. Palushani, D. Vukovic, J. Seoane, H. Ou, K. Rottwitt, and C. Peucheret, "Experimental demonstration of phase sensitive parametric processes in a nano-engineered silicon waveguide," in *Conference on Lasers and Electro-Optics, CLEO* (2013), paper CM4D.7.

[176] S. Zlatanovic, J.S. Park, F. Gholami, J.M. Chavez Boggio, S. Moro, N. Alic, S. Mookherjea, and S. Radic, "Mid-Infrared wavelength conversion in silicon waveguides pumped by silica-fiber-based source," *IEEE Journal of Selected Topics in Quantum Electronics*, **18**, 612–620 (2012).

[177] Y. Zhang, C. Husko, J. Schröder, S. Lefrancois, I. Rey, T.F. Krauss, and B.J. Eggleton, "Record 11 dB phase sensitive amplification in sub-millimeter silicon waveguides," in *Conference on Lasers and Electro*Optics Pacific Rim, CLEO-PR* (2013), paper PD1b-3.

[178] Y. Zhang, C. Husko, J. Schröder, S. Lefrancois, I.H. Rey, T.F. Krauss, and B.J. Eggleton, "Phase-sensitive amplification in silicon photonic crystal waveguides," *Optics Letters*, **39**, 363–366 (2014).

[179] C. Grillet, L. Carletti, C. Monat, P. Grosse, B. Ben Bakir, S. Menezo, J.M. Fedeli, and D.J. Moss, "Amorphous silicon nanowires combining high nonlinearity, FOM and optical stability," *Optics Express*, **20**, 22609–22615 (2012).

[180] J. Matres, G.C. Ballesteros, P. Gautier, J.-M. Fedeli, J. Marti, and C.J. Oton, "High nonlinear figure-of-merit amorphous silicon waveguides," *Optics Express*, **21**, 3932–3940 (2013).

[181] K. Preston, P. Dong, B. Schmidt, and M. Lipson, "High-speed all-optical modulation using polycrystalline silicon microring resonators," *Applied Physics Letters*, **92**, 151104 (2008).

[182] P. Apiratikul, A.M. Rossi, and T.E. Murphy, "Nonlinearities in porous silicon optical waveguides at 1550 nm," *Optics Express*, **17**, 3396–3406 (2009).

[183] H. Rong, Y.-H. Kuo, A. Liu, M. Paniccia, and O. Cohen, "High efficiency wavelength conversion of 10 Gb/s data in silicon waveguides," *Optics Express*, **14**, 1182–1188 (2006).

[184] J.R. Ong, R. Kumar, R. Aguinaldo, and S. Mookherjea, "Efficient CW four-wave mixing in silicon-on-insulator micro-rings with active carrier removal," *IEEE Photonics Technology Letters*, **25**, 1699–1702 (2013).

[185] A. Gajda, L. Zimmermann, J. Bruns, B. Tillack, and K. Petermann, "Design rules for p-i-n diode carriers sweeping in nano-rib waveguides on SOI," *Optics Express*, **19**, 9914–9922 (2011).

[186] L.-D. Haret, X. Checoury, F. Bayle, N. Cazier, P. Boucaud, S. Combrié, and A. De Rossi, "Schottky MSM junctions for carrier depletion in silicon photonic crystal microcavities," *Optics Express*, **21**, 10324–10334 (2013).

[187] J. Safioui, F. Leo, B. Kuyken, S.-P. Gorza, S.K. Selvaraja, R. Baets, P. Emplit, G. Roelkens, and S. Massar, "Supercontinuum generation in hydrogenated amorphous silicon waveguides at telecommunication wavelength," *Optics Express*, **22**, 3089–3097 (2014).

[188] B. Kuyken, H. Ji, S. Clemmen, S.K. Selvaraja, H. Hu, M. Pu, M. Galili, P. Jeppesen, G. Morthier, S. Massar, L.K. Oxenløwe, G. Roelkens, and R. Baets, "Nonlinear properties of and nonlinear processing in hydrogenated amorphous silicon waveguides," *Optics Express*, **19**, B146–B153 (2011).

[189] K.-Y. Wang and A.C. Foster, "Continuous-wave frequency conversion in hydrogenated amorphous silicon waveguides," in *Conference on Lasers and Electro-Optics, CLEO* (2012), paper QF3G.6.

[190] R.J. Suess, M.M. Jadidi, K. Kim, and T.E. Murphy, "Characterization of optical nonlinearities in nanoporous silicon waveguides via pump-probe heterodyning technique," *Optics Express*, **22**, 17466–17477 (2014).

[191] A. Gajda, L. Zimmermann, M. Jazayerifar, G. Winzer, H. Tian, R. Elschner, T. Richter, C. Schubert, B. Tillack, and K. Petermann, "Highly efficient CW parametric conversion at 1550 nm in SOI waveguides by reverse biased p-i-n junction," *Optics Express*, **20**, 13100–13107 (2012).

[192] P.J. Foster, J.K. Doylend, P. Mascher, A.P. Knights, and P.G. Coleman, "Optical attenuation in defect-engineered silicon rib waveguides," *Journal of Applied Physics*, **99**, 073101 (2006).

[193] R.A. Soref and B.R. Bennet, "Electrooptical effects in silicon," *IEEE Journal of Quantum Electronics*, **23**, 123–129 (1987).

[194] Y. Ding, C. Peucheret, H. Ou, and K. Yvind, "Fully etched apodized grating coupler on the SOI platform with -0.58 dB coupling efficiency," *Optics Letters*, **39**, 5348–5350 (2014).

[195] K.A. Croussore and G. Lil, "Phase regeneration of DPSK signals based on symmetric-pump phase-sensitive amplification in bismuth oxide highly nonlinear fiber," in *Conference on Lasers and Electro-Optics, CLEO* (2007), paper CMZ4.

[196] C. Schmidt-Langhorst, R. Ludwig, M. Galili, B. Huettl, F. Futami, S. Watanabe, and C. Schubert, "160 Gbit/s all-optical OOK to DPSK in-line format conversion," in *European Conference on Optical Communication, ECOC* (2006), paper Th4.3.5.

[197] J. Wang, J. Sun, X. Zhang, D. Huang, and M.M. Fejer, "All-optical format conversion using periodically poled lithium niobate waveguides," *IEEE Journal of Quantum Electronics*, **45**, 195–205 (2009).

[198] J. Wang, Q. Sun, and J. Sun, "Simultaneous demonstration on FWM-based all-Optical 40 Gbit/s multicasting CSRZ-DPSK logic XOR gate and CSRZ-DPSK to RZ-DPSK format conversion," in *Asia Communications and Photonics Conference, ACP* (2009), paper TuX1.

[199] D. Wang, M. Zhang, J. Qin, G.-W. Lu, H. Wang, and S. Huang, "Multifunctional switching unit for add/drop, wavelength conversion, format conversion, and WDM multicast based on bidirectional LCoS and SOA-loop architecture," *Optics Express*, **22**, 21847–21858 (2014).

[200] M.J. Power, R.P. Webb, and R.J. Manning, "All-optical phase discrimination using SOA," *Optics Express*, **21**, 25664–25669 (2013).

[201] R.P. Webb, M. Power, and R.J. Manning, "Phase-sensitive frequency conversion of quadrature modulated signals," *Optics Express*, **21**, 12713–12727 (2013).

[202] J. Xu, X. Zhang, and J. Mørk, "Investigation of patterning effects in ultrafast SOA-based optical switches," *IEEE Journal of Quantum Electronics*, **46**, 87–94 (2010).

[203] J. Xu, Y. Ding, C. Peucheret, W. Xue, J. Seoane, B. Zsigri, P. Jeppesen, and J. Mørk, "Simple and efficient methods for the accurate evaluation of patterning effects in ultrafast photonic switches," *Optics Express*, **19**, 155–161 (2010).

[204] M. Seimetz, *High-Order Modulation for Optical Fiber Transmission*, Springer, 2009.

[205] G. Hesketh and P. Horak, "All-optical phase regeneration of multilevel amplitude and phase shift keyed signals," in *Conference on Lasers and Electro-Optics, CLEO/Europe* (2013), paper CI-3.3.

[206] Y.L. Lee, Y.-C. Noh, C. Jung, T.J. Yu, D.-K. Ko, and J. Lee, "Broadening of the second-harmonic phase-matching bandwidth in a temperature gradient-controlled periodically poled Ti:LiNbO3 channel waveguide," *Optics Express*, **11**, 2813–2819 (2003).

[207] H. Song, O. Tadanaga, T. Umeki, I. Tomita, M. Asobe, S. Yamamoto, K. Mori, and K. Yonenaga, "Phase-transparent flexible waveband conversion of 43 Gb/s RZ-DQPSK signals using multiple-QPM-LN waveguides," *Optics Express*, **18**, 15332–15337 (2010).

[208] T. Richter, R. Nouroozi, H. Suche, W. Sohler, and C. Schubert, "PPLN-waveguide based tunable wavelength conversion of QAM data within the C-band," *IEEE Photonics Technology Letters*, **25**, 2085–2087 (2013).

[209] H. Kawakami, E. Yoshida, and Y. Miyamoto, "Auto bias control technique based on asymmetric bias dithering for optical QPSK modulation," *Journal of Lightwave Technology*, **30**, 962–968 (2012).

[210] L. Yin, *Study of Nonlinear Optical Effects in Silicon Waveguides*, Ph.D. thesis, University of Rochester, Rochester, USA, 2009.

[211] E. Süli, and D.F. Mayers, *An Introduction to Numerical Analysis*, Cambridge University Press, 2003.

[212] L. Yin and G.P. Agrawal, "Impact of two-photon absorption on self-phase modulation in silicon waveguides," *Optics Letters*, **32**, 2031–2033 (2007).

[213] A.B. Carlson, *Communication Systems*, McGraw-Hill International Editions, 1986.